QUANTUM INFORMATION PROCESSING WITH FREQUENCY-BIN QUDITS

A Dissertation

Submitted to the Faculty

of

Purdue University

by

Hsuan-Hao Lu

In Partial Fulfillment of the

Requirements for the Degree

of

Doctor of Philosophy

December 2020

Purdue University

West Lafayette, Indiana

THE PURDUE UNIVERSITY GRADUATE SCHOOL
STATEMENT OF DISSERTATION APPROVAL

Dr. Andrew M. Weiner, Chair

School of Electrical and Computer Engineering

Dr. Tongcang Li

School of Physics and Astronomy

Dr. Mahdi Hosseini

School of Electrical and Computer Engineering

Dr. Joseph M. Lukens

Quantum Information Science Group, Oak Ridge National Laboratory

Approved by:

Dr. Dimitrios Peroulis

Head of the School of Electrical and Computer Engineering

This dissertation is dedicated to my family for their unwavering support.

ACKNOWLEDGMENTS

First and foremost, I would like to express my utmost gratitude to my advisor Prof. Andrew M. Weiner for his constant inspiration. I truly appreciate to have the opportunity to work under his guidance in the past years and learn how to tackle research problem as a scientist and an engineer—Four years ago Prof. Weiner's lab in Purdue University was the only place I applied to and I truly enjoy every second working in such supportive and innovative environment. I am also thankful to Prof. Tongcang Li and Prof. Mahdi Hosseini for serving on my doctoral committee and for their constructive feedbacks. Finally, I owe a special debt of gratitude to Dr. Joe Lukens for his mentorship since I joined Purdue. His wealth of knowledge in the field of quantum optics and the incessant passion in exploring and creating knowledge are the pillars behind the success of our Purdue/ORNL collaboration.

I could not accomplish this work without constant backing from all my colleagues in the Ultrafast Optics Lab. I miss the COVID-free era when we can hang out in the office, working together and bugging each other with little things in life. I would like to especially acknowledge Dr. Daniel Leaird, Dr. Ogaga Odele, Dr. Poolad Imany, Dr. Oscar Sandoval, Dr. Mohammed S. Alshaykh, Keith McKinzie and Navin Lingaraju for their valuable instructions and discussions throughout the years. I thank my senior colleagues in ORNL, Dr. Pavel Lougovski, Dr. Bing Qi, Dr. Brian Williams, Dr. Nick Peters, and Dr. Joe Lukens for always spending time answering my naive questions, driving me around for dining and grocery shopping, and just making me feel so at home in the so-called *Secret City*.

I am truly grateful to my friends outside the lab as well. I will miss Yi-Ting, Tzu-Chun, Pin-Hsuan and Yen-Sung for their company and the small trips to Indianapolis, Chicago, and other cities just for getting some good meals and bubble teas. I thank Maggie for valuable help in many aspects. All the hours spent working and studying

in the library and coffee shops add more colours to my PhD life. I appreciate the support from my friends in different time zones, Abby and Victoria in Taiwan, and Dominika in Poland. Finally, I thank Hao-Wen and all my family members for their genuine love and continuous encouragement throughout all of graduate school. Their love and care is the reason I can pick myself up when I fell down.

TABLE OF CONTENTS

Page

Page

LIST OF FIGURES

Figure Page

Figure Page

Figure Page

Figure Page

Figure Page

Figure Page

Figure Page

SYMBOLS

d	dimension of the single photon
η	pathway efficiency
F	discrete Fourier transform
$\mathcal{F}_\rho$	quantum state fidelity
$\mathcal{F}_W$	quantum gate fidelity
H	Hadamard operation
$\mathcal{H}(Y\|X)$	conditional entropy of Y given X
$\mathbb{1}$	identity operation
$\hat{\rho}$	density matrix
μ	photon-pair generation probability
$\Delta\omega$	frequency-bin spacing
$\mathcal{P}_W$	quantum gate success
Q	total number of components
$\mathcal{R}$	beamsplitter reflectivities
$\mathcal{T}$	beamsplitter transmissivities
V	mode transformation matrix
W	state transformation matrix
X, Y, Z	Pauli X,Y and Z

ABBREVIATIONS

AWG	arbitrary waveform generator
BFC	biphoton frequency comb
BME	Bayesian mean estimation
CAR	coincidence-to-accidental ratio
CFBG	chirped fiber Bragg grating
CNOT	controlled-not
CW	continuous-wave
DoF	degree of freedom
DFT	discrete Fourier transform
EO	electro-optic
EOM	electro-optic phase modulator
EPR	Einstein-Podolsky-Rosen
FSR	free spectral range
FWHM	full-width at half-maximum
HOM	Hong-Ou-Mandel
IM	intensity modulator
LOQC	linear-optical quantum computation
MCMC	Markov chain Monte Carlo
MLE	maximum likelihood estimation
NISQ	Noisy Intermediate-Scale Quantum
OSA	optical spectrum analyzer
POVM	positive-operator valued measure
PPLN	periodically poled lithium niobate
PS	Fourier-transform pulse shaper

SPDC	spontaneous parametric down conversion
QFC	quantum frequency conversion
QFP	quantum frequency processor
QIP	quantum information processing
QPT	quantum process tomography
QST	quantum state tomography
RF	radio-frequency
SNSPD	superconducting nanowire single-photon detector
SPDC	spontaneous parametric down-conversion
VQE	variational quantum eigensolver
WDM	Wavelength-division multiplexing
WSS	Wavelength-selective switch

ABSTRACT

Lu, Hsuan-Hao Ph.D., Purdue University, December 2020. Quantum Information Processing with Frequency-bin Qudits. Major Professor: Andrew M. Weiner.

Encoding quantum information in narrow, equispaced frequency bins has emerged as a novel scheme for photonic quantum information processing (QIP) due to its inherent high-dimensionality and compatibility with dense spectral multiplexing networks. Generation and distribution of such state, commonly known as biphoton frequency combs (BFCs), have been widely demonstrated over fiber- and chip-compatible platforms, while the *processing* side is relatively underdeveloped. In this dissertation, we focus on the realization of the quantum frequency processor, a photonic device comprised of an alternating sequence of electro-optic phase modulators and Fourier-transform pulse shapers, capable of processing BFCs in a parallel and low-noise fashion. Utilizing standard telecommunication components, we experimentally complete the universal gate set required for scalable quantum computing, including a high-fidelity Hadamard gate and a coincidence-basis controlled-NOT gate. High-dimensional quantum operations are also explored on our device, where we implement the first frequency-bin tritter, a three-mode extension of the Hadamard gate. Moreover, we exploit the natural parallelizability of the system and implement tunable and independent qubit operations on co-propagating qubits. We realize frequency-bin Hong-Ou-Mandel interference with record-high visibility, as well as the first high-fidelity spectral correlation flip on two-qubit entangled states. Finally, we demonstrate essential functionalities for quantum networking, including arbitrary single-qubit rotations, and for the first time, a frequency-domain Bell-state analyzer.

Each of these demonstrations represents a primitive but essential function in frequency domain QIP, with the potential of scaling up such fundamental systems into

larger processors thanks to ongoing efforts in integrated photonics design. Such large-scale integrated processors would then be well positioned for the application such as interconnecting matter qubits with mismatched frequencies and various quantum communication protocols based on frequency-bin encoding.

1. INTRODUCTION

Classical optical frequency combs have revolutionized a myriad of fields, from optical spectroscopy [1] to optical clocks [2], and have enabled arbitrary microwave synthesis [3], lightwave communication [4] and generation of attosecond pulses using high-harmonic generation [5–7]. Various forms of classical frequency combs have been extensively explored and tailored to specific applications [8,9]. On the other hand, applications for their non-classical counterparts, namely "quantum frequency combs," have only recently began to burgeon. Quantum frequency combs, also known as biphoton frequency combs (BFCs) [10,11], are usually described as two-photon states formed by many, discrete pairs of energy-matched comb lines (or "bins" for short), where strong time-energy correlation and stable phase coherence across the optical spectrum are shared between the photon pair. A great amount of information can be stored in many spectro-temporal quantum modes, which provides a unique framework for quantum information processing (QIP) in a single fiber-optic spatial mode [12], thereby enabling natural phase stability and compatibility with current fiber networks. Moreover, recent progress toward realization of BFCs with on-chip microring resonators [13–15] further enables generation of complex states in a scalable fashion. The inherent robustness and high dimensionality of this optical platform[1] could display significant promise to realize manifold QIP tasks, including fiber-compatible quantum networks and distributed quantum sensing.

To realize the aforementioned potential and possible applications with QFCs, a major piece of functionality is still missing—"an universal set of quantum gates", as

[1]In this dissertation, we will concentrate on discrete-variable (DV), gate-based QIP, while omitting the discussion of continuous-variable (CV) encoding with quantum frequency comb [16]. Large-scale, complex cluster states can be generated in various CV-based systems [17, 18], but the constituent comb lines are relatively difficult to manipulate with our proposed device due to the narrow free spectral range.

suggested by the Divincenzo's criteria [19], comprised of single-qubit rotations plus a two-qubit entangling gate, capable of synthesizing any arbitrary quantum operation. The very stability which makes frequency such a useful degree of freedom (DoF) for *encoding* information presents an array of unique challenges for quantum state *processing*, such as mixing and manipulating frequency modes at the single-photon level or even conditioned on the presence of a photon in a specific mode. In this dissertation, we attempt to address this specific challenge. Through the use of the newly developed quantum frequency processor (QFP) [20], a device incorporating both electro-optic modulation and pulse shaping techniques, frequency bins, that otherwise do not interact, can be coupled in a controlled fashion with remarkable precision. In the first demonstration, we focus on the realization of single-photon quantum gates, including a frequency-bin beamsplitter and a three-dimensional tritter [21], both with near-unity fidelity. These gates represents the basic building blocks toward scalable QIP based on frequency-bin encoding platform, and can soon find a range of applications such as quantum simulations and high-dimensional quantum communication.

Moving beyond single-photon frequency manipulation to full-fledged QIP with frequency-encoded qubits, we realize frequency-bin Hong-Ou-Mandel (HOM) interference, a foundational multiphoton effect [22] underlying two-qubit gates in the linear-optical quantum computing (LOQC) paradigm [23], with record highest visibility for photons of different colors [24]. We further showcase the potential for performing massively parallelized and independent operations on frequency bins, applying distinct single-qubit gates on two spectrally separated qubits to manipulate their spectral correlation [24]. Additionally, two-qubit entangling gate, a basic quantum computing functionality has heretofore proven elusive on the frequency-bin encoding platform due to the absence of strong photon-photon interaction and additional challenge from the mismatched wavelength, is firstly demonstrated with our device [25]. We also developed a tailored Bayesian machine learning approach to characterize the gate transformation, and validate its high-fidelity performance.

By this point the QFP has been experimentally leveraged to realize a broad set of QIP primitives. In the last part of our thesis, we shift our focus to designing useful functionalities for general-purpose protocols in frequency-bin quantum information. We experimentally demonstrate arbitrary gates utilizing the QFP, attaining ultrahigh mode transformation fidelities and confirming theoretically expected success probabilities [26]. These results provide a valuable foundation for applications in networking and communications, such as superdense coding [27] and quantum teleportation [28].

Furthermore, we design a Bell-state analyzer—a core unit to realize entanglement swapping and quantum teleportation in a quantum network—and experimentally realize such a device for spectrally distinguishable, frequency-encoded photonic qubits for the very first time. We unambiguously distinguish two of four Bell states with accuracy over 98%, which represents an important step toward the long-term vision of a quantum internet that is compatible with both heterogeneous nodes and dense spectral multiplexing. Finally, we present a novel quantum state tomographic technique drawing on both theoretical (Bayesian analysis) and experimental (EOMs and pulse shapers) methods developed in this dissertation. Applying a sequence of random quantum operations to signal-idler photon pairs followed by coincidence measurements, we are able to reconstruct two-qudit (up to $d = 5$) states with extremely high quantum state fidelity (> 0.93) and an upper bound of distillable entanglement close to ideal ($\sim\log_2 d$ ebits), which is the record-highest demonstrated in the discrete frequency-bin encoding platform. Such a technique can prove valuable to the frequency QIP community as building high-dimensional quantum gates is still considered challenging.

This dissertation is organized as follows. In Chapter 1 we describe in detail the building blocks of frequency-bin QIP, followed by the experimental implementation of high-fidelity Hadamard and discrete Fourier-transform gates for frequency qubits and qutrits in Chapter 2. Extending to operations on multiple qubits, we discuss the demonstration of frequency-bin HOM and correlation swapping experiments in Chapter 3. We cover our last missing piece for universal QIP, a post-selected controlled-

NOT (CNOT) gate, in Chapter 4. Chapter 5 tackles the important question of arbitrary single-qubit rotations and state reconstruction in frequency-encoding platform. Finally, in Chapter 6 we highlight several QIP tasks developed on the QFP paradigm. We have a short outlook section at the end of each chapter, stating the key areas for improvements in the future work. The Appendix section encompasses a great amount of information, including detailed simulation results and notes, transformation matrix reconstruction, Bayesian mean estimation method, etc.

1.1 Frequency-bin Quantum Information Processing (QIP)

1.1.1 Frequency-Bin Encoded Qudits

At a high level, any system for discrete-variable-based QIP requires first and foremost well-defined d-dimensional qudits (qubits for $d = 2$), which in the case of photonic QIP consists of selecting a particular DoF (set of modes or, in the parlance of quantum mechanics, the Hilbert space). Quantum information can be encoded in a scalable and interferometrically stable fashion using broadband frequency combs whereby every spectral comb line becomes an information carrier. The available mode space thus comprises countably infinite set of equispaced bins centered at frequencies $\omega_n = \omega_0 + n\Delta\omega$ $(n \in \mathbb{Z})$. A single-qubit state can be represented as a photon in a superposition of two modes indexed n_0 and n_1:

$$\psi = \alpha \left|1_{\omega_{n_0}}\right\rangle + \beta \left|1_{\omega_{n_1}}\right\rangle, \tag{1.1}$$

where $|\alpha|^2 + |\beta|^2 = 1$, and $|1_{\omega_n}\rangle$ corresponds to the Fock state with a single photon residing in bin with frequency ω_n. More generally, a single-qudit state can be defined as a d-mode superposition $\sum_{k=0}^{d-1} c_k \left|1_{\omega_{n_k}}\right\rangle$ where $\sum_{k=0}^{d-1} |c_k|^2 = 1$.

The preparation of this frequency-multiplexed state, i.e., a single photon in a quantum superposition of many frequency modes, usually requires entangled photon pairs (or, biphotons) generation in the form of BFCs followed by heralding operations [13]—that is, the detection of one photon suggests the presence of the other photon. One of

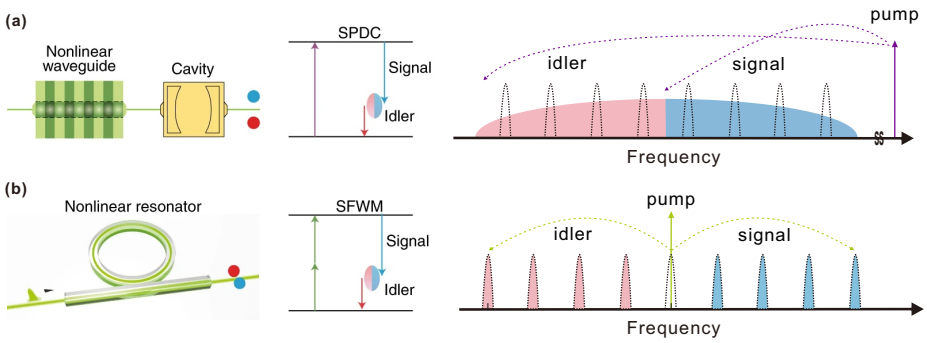

Fig. 1.1. **Generation of biphoton frequency combs.** (a) Broadband biphoton spectrum generated in $\chi^{(2)}$ nonlinear waveguides via SPDC, followed by cavity filtering. (b) Comb-like biphoton spectrum generated in $\chi^{(3)}$ nonlinear resonators via SFWM. (The figure is adapted and modified from Kues *et al.* [11])

the most conventional methods for BFC generation utilizes spontaneous parametric down conversion (SPDC) process [29], in which a high-energy pump photon is coupled into a $\chi^{(2)}$ material, such as periodically poled lithium niobate (PPLN) waveguide, and decays into a pair of entangled photons [Fig. 1.1 (a)]. Whereas individually these photons can possess any frequency value from a continuous, broadband spectrum, collectively their frequency distributions are highly correlated due to energy conservation. To create comb-like features in the frequency domain, we usually introduce etalon or Fourier-transform pulse shapers [3, 30] as a programmable filter to carve out the BFC. Recently, BFC generation is also realized on miniaturized platforms via spontaneous four-wave mixing (SFWM), where two pump photons decay into entangled photon pairs within an integrated ring resonator in the presence of $\chi^{(3)}$ nonlinearity [13, 15, 31, 32]. The resonant structure naturally forces photons to stay in a set of equispaced frequency modes spaced by the free spectral range (FSR), with the phase matching bandwidth covering several of these resonances [Fig. 1.1 (b)].

Then, to manipulate qubits optically one must be able to implement arbitrary frequency-bin operations with high fidelity, such that superpositions of various frequency bins can be converted to other superpositions defined by a unitary input/output matrix. One could envision performing unitaries on frequency bins through nonlinear

optical interactions, and indeed, quantum frequency mixers based on $\chi^{(2)}$ [33,34] and $\chi^{(3)}$ [35,36] nonlinearities have been demonstrated on two-dimensional Hilbert spaces. However, scaling up this approach to many bins is unclear, as it would require additional pump fields, carefully engineered phase-matching conditions, and aggressive pump filtering.

Alternatively, we adopt a novel approach proposed and theoretically developed by Lukens *et al.* [12], termed "spectral LOQC", motivated by the revolutionary LOQC scheme proposed by Knill, Laflamme, and Milburn (KLM) in 2001 [23]—a universal photonic QIP architecture based on linear optical components, including beamsplitters, phase shifters, photon counters, and measurement-induced nonlinearities. Spectral LOQC follows this perception and introduces electro-optic phase modulators (EOMs) and Fourier-transform pulse shapers (PSs) for frequency-bin manipulations, substituting the role of beamsplitters and phase shifters as neither of them is suited for single-spatial-mode operation. This substitution, as illustrated in Fig. 1.2, is not in a one-to-one fashion, since both EOMs and PSs can operate on a formally infinite-dimensional space of frequency bins rather than pair-wisely. Instead, a sequence of alternating temporal (in EOMs) and spectral modulations (in PSs) is found sufficient to realize any arbitrary unitary transformation on d spectral modes, with the total number of components required scaling like $\mathcal{O}(d)$. In contrast, the scaling in spatial- or polarization-encoded LOQC is $\mathcal{O}(d^2)$ [38]. In the following sections, we are going to discuss the functionality of EOMs and PSs in detail, and how a cascade of them (the QFP) can implement any arbitrary frequency-bin operations.

1.1.2 Fourier-Transform Pulse Shaper (PS)

Pulse shapers are frequently used in our experiments as spectral phase and amplitude filters to address each frequency mode. This device separates input frequency modes with a spectral disperser (e.g., diffraction gratings or prisms) and focuses different spectral components to small diffraction-limited spots onto liquid crystal modu-

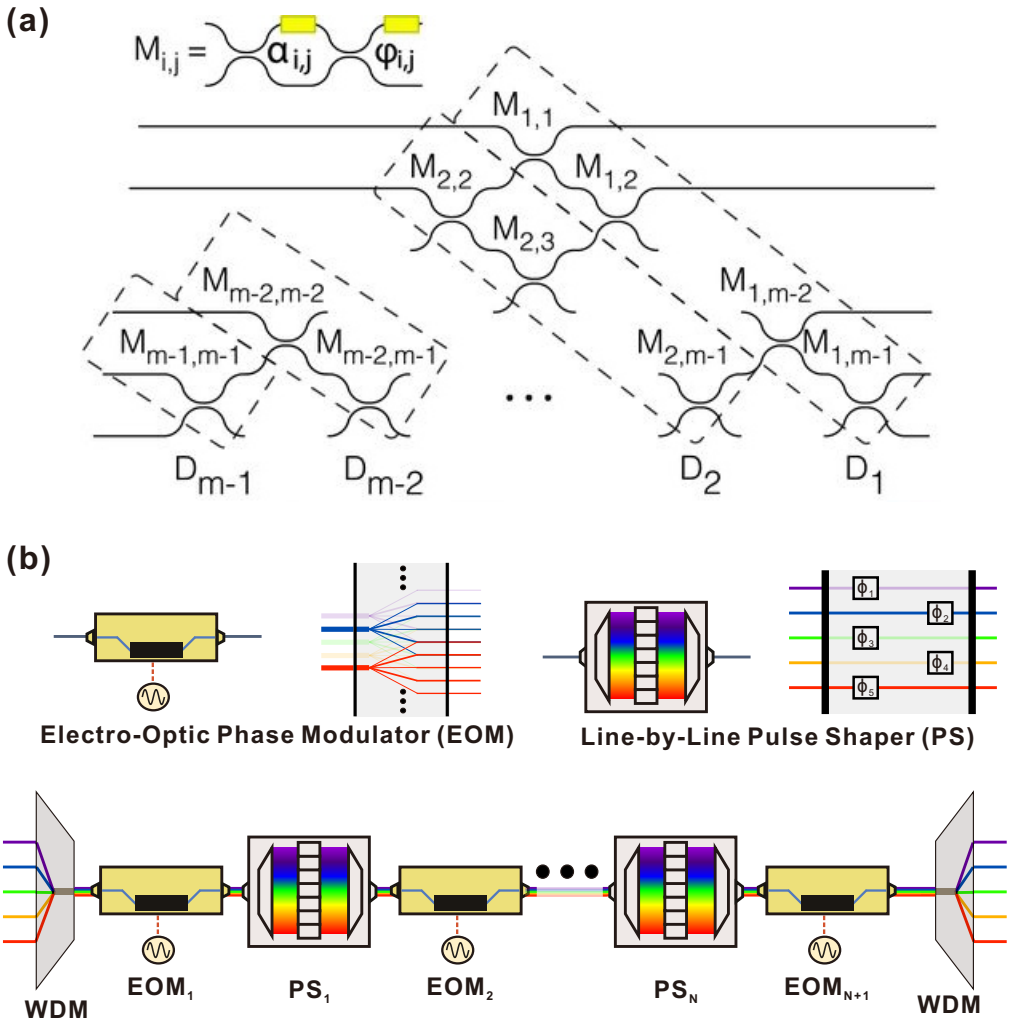

Fig. 1.2. **Transformations in spatial- and spectral LOQC.** (a) Path-based unitaries can be constructed from two-mode Mach-Zehnder interferometers $M_{i,j}$, each of which is composed of two spatial beamsplitters and two phase shifters [yellow box]. The total number of components scales *quadratically* with the number of spatial modes. (Carolan *et al.* [37]) (b) Frequency-bin unitaries build instead on two fundamental components, EOMs and PSs, producing a complete network via an alternating sequence (the QFP). The various horizontal paths shown correspond to distinct frequencies, all residing in a single spatial mode. The total number of components scales *linearly* with the number of frequency bins.

lator (LCM) arrays at the focal plane. One can program an user-defined pattern onto the LCM arrays via voltage controls, applying phase- and amplitude-modulation independently to the spatially dispersed optical components. Finally, a second lens and spectral disperser recombine all constituent frequencies in the shaped field into a single collimated beam. Owing to the Fourier relation between frequency and time, earliest demonstrations were mostly concentrated on shaping the temporal waveform of the classical light field on femtosecond timescales [30, 39], such as single-cycle ultrashort pulse generations [40] and optical arbitrary waveform generations [3]. This concept can readily apply to non-classical light field as well. Pe'er *et al.* firstly demonstrated shaping the time correlation function of entangled photon pairs [41] with phase-only spectral modulation, and Zäh *et al.* further extended to full amplitude and phase modulation of time-energy entangled two-photon states [42]. Following these pioneering demonstrations, a wide range of experiments have showcased the utility of pulse shaping at the single-photon level, including dispersion cancellation [43], quantum state reconstruction [44], and spectral coding [45].

In our works, pulse shaper can be visualized as a bank of user-defined attenuators and phase shifters over all frequency bins [Fig. 1.2(b)][2]. To ensure that we can operate in the line-by-line shaping [46, 47] regime, i.e., each frequency bin can be addressed independently, the bin spacing needs to be carefully chosen to exceed the pulse shaper resolution (determined by the optical beam size, grating period, focal length, etc). In most of our works, the frequency-bin spacing is chosen at 25 GHz, well above the commercial pulse shaper resolution (∼10 GHz; Finisar Corporation), meanwhile matching the standard ITU grid for dense wavelength-division multiplexing (DWDM) applications. The total optical bandwidth of the pulse shaper (5 THz, in our case) combined with the tightest available bin spacing will ultimately determine how many frequency modes can be addressed in parallel.

[2]For quantum gate construction, phase-only modulation is considered for the sake of unitarity.

1.1.3 Electro-Optic Phase Modulator (EOM)

As noted above, universal QIP also requires *mixing* different modes to, e.g., create superposition and generate single- and multi-photon interference [23]. For most DoFs in the photon, mixing different modes is straightforward—for example, spatial modes can be mixed via conventional beamsplitters or evanescently coupled waveguides, and polarization modes can be easily manipulated with a sequence of waveplates. Mixing frequency modes, on the other hand, requires generation of new frequency components, and thus nonlinear optical methods are instantly summoned [33–36]. Electro-optic modulation represents an attractive alternative: It requires no optical pumps, relies on purely electrical controls, and is compatible with state-of-the-art telecommunication technology. The applied radio-frequency (RF) voltage across the EOM can modify the refractive index of the material and introduce a temporal phase modulation to the co-propagating optical field. Assume this RF drive is periodic at frequency $\Delta\omega$, the optical energy can be redistributed into frequency sidebands spaced at $\Delta\omega$, an effect widely exploited for EO frequency comb generators [48, 49].

Importantly, EOMs are optically linear and independent of the input optical power, thus representing a strong candidate for manipulating single photons. Indeed, a large number of experiments have displayed the potential of EO modulations on quantum light after the first demonstration by Kolchin *et al.* [50], including non-local modulation cancellation [51], frequency-bin entanglement [52–54], large-alphabet quantum key distribution [55], bandwidth compression of single photon [56], etc. In this work, EOMs are driven by a periodic RF signal with frequency equal to the mode spacing, causing states across distinct input frequency bins to overlap and interfere in a complex fashion set by the specific RF waveform [Fig. 1.2(b)]. For maximum generality in the original proposal [12], it was assumed each EOM could be driven by arbitrary modulation patterns repeating at $\Delta\omega$. However, reproducing the required phase modulation bandwidth can pose a significant practical challenge to both electronic waveform generators and EOMs. A major finding in our works

is that much simpler single-tone drive signals are sufficient to construct many basic quantum gates with an extremely small reduction in performance; introducing extra harmonics to the microwave drives further improves performance and can facilitate implementation of higher-dimensional ($d > 2$) quantum operations.

In the following sections, we will describe the mathematical model to handle the transformation of PSs and EOMs, and discuss how to numerically find the spectral and temporal phase patterns required to synthesize a target quantum operation.

1.2 Modeling the Quantum Frequency Processor (QFP)

To describe how PSs and EOMs operate on discrete frequency modes, we start with introducing the positive-frequency electric-field operator [12, 57, 58] to describe the input state as

$$\hat{E}_{in}^{(+)}(t) = \sum_{n=-\infty}^{\infty} \hat{a}_n e^{-i\omega_n t}, \tag{1.2}$$

and the output state after the quantum operation as

$$\hat{E}_{out}^{(+)}(t) = \sum_{n=-\infty}^{\infty} \hat{b}_n e^{-i\omega_n t}, \tag{1.3}$$

where the symbol $\hat{a}_n$ and $\hat{b}_n$ denote the annihilation operator in the frequency bin centered at ω_n, before and after the operation. Mode transformation in a linear-optical device is represented by a matrix V, which connects the input $\hat{a}_n$ and output $\hat{b}_m$ (at frequencies ω_m) via

$$\hat{b}_m = \sum_{n=-\infty}^{\infty} V_{mn} \hat{a}_n. \tag{1.4}$$

The ideal line-by-line shaper can apply an arbitrary phase shift to each spectral mode, i.e.,

$$\hat{E}_{out}^{(+)}(t) = \sum_{n=-\infty}^{\infty} e^{i\phi_n} \hat{a}_n e^{-i\omega_n t}, \tag{1.5}$$

and thus the operation can be described as $[V]_{mn} = e^{i\phi_m}\delta_{mn}$, a diagonal unitary matrix in the frequency mode space.

On the other hand, consider an EOM driven with phase $\varphi(t)$, assumed periodic at the inverse mode spacing ($T = 2\pi/\Delta\omega$). The temporal phase modulation operation can be expressed using the Fourier series expansion $e^{i\varphi(t)} = \sum_k c_k e^{ik\Delta\omega t}$, where

$$c_k = \frac{1}{2\pi}\int_T dt\, e^{i\varphi(t)} e^{ik\Delta\omega t} \tag{1.6}$$

are the Fourier series coefficients of the periodic EOM operation. For example, in the case of single-sinewave modulation, i.e., $\varphi(t) = \Theta \sin \Delta\omega t$ with Θ denoting the modulation depth, c_k are revealed to be Bessel functions of the first kind, $J_k(\Theta)$. The output electric field then transforms as

$$\hat{E}^{(+)}_{out}(t) = e^{i\varphi(t)}\hat{E}^{(+)}_{in}(t) = \sum_{k=-\infty}^{\infty}\sum_{n=-\infty}^{\infty} c_k \hat{a}_n e^{-i(\omega_n + k\Delta\omega)t}. \tag{1.7}$$

We can derive the mode transformation as

$$\hat{b}_m = \sum_{n=-\infty}^{\infty} c_{m-n}\hat{a}_n, \tag{1.8}$$

which describes how an EOM couples an input mode to infinitely many output modes, with coupling coefficients depending only on the frequency difference between input and output modes. The matrix form of this transformation, $[V]_{mn} = c_{m-n}$, is a Toeplitz (diagonal-constant) matrix; namely, the ideal EOM is invariant to optical frequency translation. Any modulation which succeeds in coupling, say, mode n to $n+1$, will also couple modes $n+1$ to $n+2$ with equal weight. This feature, however, suggests that a single EOM cannot serve as a *deterministic* mode mixer, no matter how intricate the periodic modulations are designed. An operation intends to mix the frequency bins in the computational space, i.e., the predefined subset of frequency bins used to encode quantum information, will also scatter photon outside of the space. This fundamental limitation precludes the single-modulator-based scheme for general-purpose QIP, but may be acceptable[3] for experiments like frequency-bin entanglement verification [53, 54, 59] and probabilistic frequency-bin HOM interference [60].

[3]The probabilistic nature of frequency mixing process may still be problematic if one would like to extend the system to higher dimension, in which a large portion of photons are lost to sidebands not intended for the targeted mixing process.

QFP delivers as the alternative solution for frequency-bin QIP, introducing PSs between every two EOMs; the spectral phase imparted by the middle stage ensures that the generated sidebands are returned to the computational space at the last stage through successive frequency-bin interferences, thereby making it possible to realize a fully deterministic frequency-bin quantum operation.

1.3 Numerical Optimization Approach

Now we have qualitatively explained why an alternating sequence of EOMs and PSs can realize a target frequency-bin transformation, we move on to discuss the numerical optimization procedures we adopt to find the phase patterns for experimental implementation. More detailed discussions can also be found in [12, 21, 26, 61].

Fig. 1.3 shows the schematic of QFP construction. For simulation purposes, we discretize a single temporal period of EO modulation into M samples and truncate the number of frequency modes to M as well. This truncation provides an accurate approximation to the $d \times d$ operation of interest as long as $M \gg d$, which guarantees that the simulation can fully encompass all frequency modes occupied by photons throughout the operation. In the M-bin discretization, each pulse shaper acts as an $M \times M$ diagonal unitary D consisting of complex-exponential elements (phase shifts) over frequency bins. On the other hand, an EOM is represented as an $M \times M$ diagonal unitary D operating on *time* samples, or as $FDF^\dagger$ in the frequency domain, where F is the $M \times M$ discrete Fourier transform matrix (DFT) with elements defined as $F_{nk} = M^{-1/2} e^{2\pi i n k/M}$. We can then approximate the mode transformation matrix V for a QFP with a total number of Q alternating elements by

$$V = FD_Q F^\dagger \cdots D_2 F D_1 F^\dagger. \tag{1.9}$$

We explicitly consider QFPs consisting of $Q \in \{1, 3, 5, ...\}$ components, in which EOMs comprise the first and last devices in the sequence, since we have found that the additional phase shifts available by adding a shaper on the front or back end of the QFP does not enable a better performance than the configuration without it.

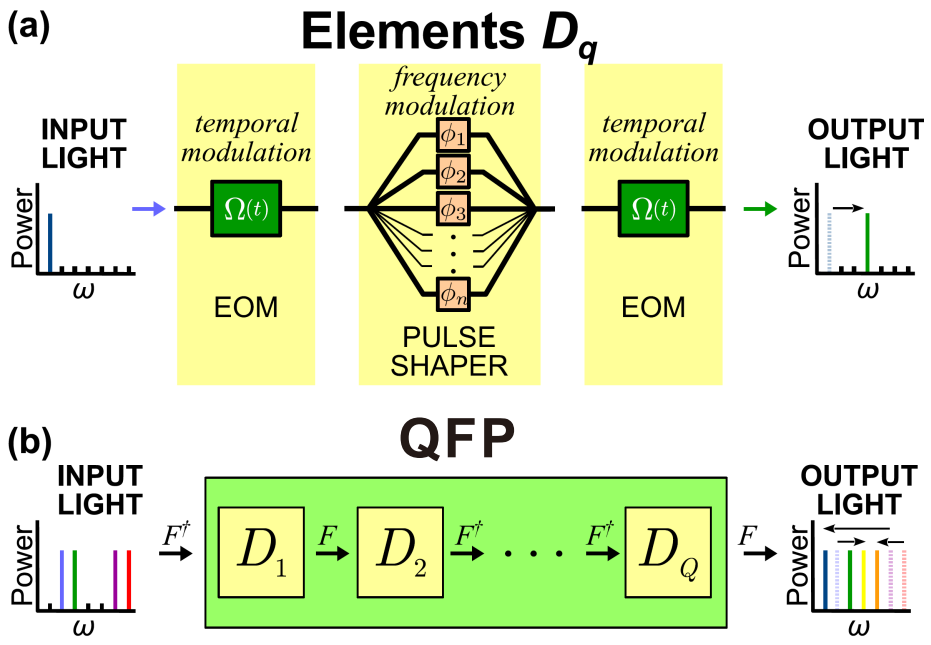

Fig. 1.3. **Schematic of QFP construction.** QFP example with a total number of three elements ($Q = 3$). Each element applies phase modulation in either time (EOMs) or frequency (shapers), realizing some desired frequency transformation. (b) An arbitrary cascade of Q elements. Both EOMs and PSs can be modeled as diagonal unitary matrices operating on the time and frequency domain, respectively. To model the transformation in an alternating sequence of them, discrete Fourier transforms (DFT; F) are used for the basis change.

To assess the performance of our QFP with respect to a desired unitary operation U, we introduce two metrics for optimization: success probability $\mathcal{P}_W$ and fidelity $\mathcal{F}_W$ [12, 62].

Success probability $\mathcal{P}_W$ describes the probability of a photon staying within the computational space, irrespective of the correctness of the operation. An operation with $\mathcal{P}_W < 1$ suggests photons scattering outside of the d-dimensional computational space into adjacent bins due to the EO modulation approach, rather than an overall insertion loss of the components (assumed lossless in the simulations). Mathematically speaking, $\mathcal{P}_W$ can be defined as

$$\mathcal{P}_W = \frac{\mathrm{Tr}(W^\dagger W)}{\mathrm{Tr}(U^\dagger U)}, \tag{1.10}$$

where W denotes the equivalent *state* transformation matrix, which in the case of single-qudit operation, equals to the $M \times M$ unitary *mode* transformation matrix V truncated to the dimension of U. Derivation of W is relatively complicated in the case of two-qubit gates, as one needs to consider all the possible pathways connecting a given pair of input modes to the output modes. We will have a short discussion in Chapter 4 regarding the construction of a two-qubit CNOT gate; for detailed information, the reader is directed to the supplemental information of [12].

Fidelity $\mathcal{F}_W$, on the other hand, describes the closeness of a *successful* transformation with respect to the ideal unitary U, and can be defined as

$$\mathcal{F}_W = \frac{\mathrm{Tr}(W^\dagger U)\,\mathrm{Tr}(U^\dagger W)}{\mathrm{Tr}(W^\dagger W)\,\mathrm{Tr}(U^\dagger U)}, \tag{1.11}$$

expressed in the form of Hilbert-Schmidt inner product. The ideal condition $\mathcal{F}_W = \mathcal{P}_W = 1$ signifies the situation $W = e^{i\phi}U$, with ϕ an unimportant global phase. Practically, we would like to constrain $\mathcal{F}_W$ to be as close to one as possible (for example, within a 10^{-4} reduction), since an imperfect fidelity will requires a lot of resources for error correction [63]. On the other hand, we are less susceptible to nonunity $\mathcal{P}_W$, as we just need to wait a longer time until the gate succeed (a long sequence of gates with reduced $\mathcal{P}_W$ will still be detrimental, though).

In our simulations, we utilize the Optimization Toolbox in MATLAB to search for an optimal set of phases for D, which preserve fidelity $\mathcal{F}_W \geq 0.9999$ and maximize success probability $\mathcal{P}_W$. One could alternatively constrain $\mathcal{P}_W$, or maximize to the product $\mathcal{F}_W\,\mathcal{P}_W$; In the theoretical proposal by Lukens *et al.* [12], each matrix is characterized by M independent real numbers in $(-\pi, \pi]$ for the sake of maximum generality: for the pulse shaper (D_2), these signify the phase shifts applied to each frequency mode; for the EOMs, these are samples of the temporal phase modulation over one period. However, for experimental practicability, we constrain the temporal phase patterns to sums of sinewaves (i.e., truncated Fourier series), rather than fully arbitrary functions. Thus, taking a total of p harmonics in the optimization—each specified by an amplitude and phase—the number of free parameters for each EOM

matrix reduces to $2p$. The specific algorithm used for gate optimization is listed below in chronological order.

1.3.1 Nonlinear Constrained Optimization

Making use the built-in nonlinear constrained multivariate optimizer (*fmincon*) in MATLAB, specifically the interior point algorithm [64], we run multiple optimizations with either random values or previous solutions as starting points, and report the final solution with maximum $\mathcal{P}_W$ satisfying $\mathcal{F}_W \geq 0.9999$. If a solution cannot be found to satisfy the condition, we can either increase the total number of components Q or the total number of harmonics p for the EOMs to boost the circuit complexity.

We adopt this optimization procedure for most of our works; however, we notice that *fmincon* is susceptible to local extrema trapping near the starting points, and we have to rerun the optimizer multiple times with different initial points to ensure the optimal solution can be found. Moreover, as the target transformation extends to higher dimensions, the algorithm fails even more frequently. For example, in one set of our attempts to find the solution for the 7-dimensional DFT operation, *fmincon* only managed to find the optimum once out of 500 trials!

1.3.2 Particle Swarm Optimization with Multi-Stage Cost Function

We introduce a hybrid algorithm using particle swarm optimization (PSO)—a nature-inspired metaheuristic algorithm—together with *fmincon* for better convergence. PSO starts with a number of particles moving around in the multi-dimensional problem space[4] in search of the extremum iteratively, where each particle represents a possible solution. In each iteration, the particle moves toward a new position depending on both the history of its local best known position and that of the entire swarm. The optimizer halts when all the particles converge to a single point in the

[4]The dimension of the particle is defined by the number of variables. In the case of 2EOM/1PS driven by a total of p RF tones, the length of the particle's vector is $M + 4p$.

problem space. A potential issue for traditional PSO is that we can no longer maximize one metric while constraining another, which in our case is the gate success probability ($\mathcal{P}_W$) and fidelity ($\mathcal{F}_W \geq 0.9999$), respectively. Therefore, we follow the procedures proposed in Ref. [65] to lump both the gate success probability and fidelity into a single cost function. Specifically, the cost function we try to minimize here is $C = -\mathcal{P}_W + H(\mathcal{F}_W)$, where $H(\mathcal{F}_W) = \beta(\mathcal{F}_W) \cdot (0.9999 - \mathcal{F}_W)$ and $\beta(\cdot)$ is a multistage, relative-violated function. We choose

$$\beta(\mathcal{F}_W) = \begin{cases} 100 & ; \ 0 \leq \mathcal{F}_W < 0.9 \\ 50 & ; \ 0.9 \leq \mathcal{F}_W < 0.99 \\ 25 & ; \ 0.99 \leq \mathcal{F}_W < 0.999 \\ 10 & ; \ 0.999 \leq \mathcal{F}_W < 0.9999 \\ 0 & ; \ 0.9999 \leq \mathcal{F}_W < 1, \end{cases} \tag{1.12}$$

which reduces the penalty for fidelity as it approaches unity. For a sanity check, we follow the PSO with another quick run of *fmincon* using the best solution found in PSO as the initial point and see if the performance can be further improved.

This is the method we adopt in Chapter 5, in which we find its success rate (i.e., the frequency of attaining the ideal solution) better than the previous nonlinear constraint method. However, one of the issues we encounter is that the choice of the penalty functions seems very arbitrary, and it seems there is no literature stating how to pick the best parameters.

1.3.3 Particle Swarm Optimization with Single Cost Function

In our recent simulations, we have found that one cost function can potentially outperform other candidates and is suitable for any kind of gate design. We use particle swarm optimization to minimize the following cost function (C):

$$C = \begin{cases} \mathcal{P}_W \log_{10}(1 - \mathcal{F}_{\mathcal{W}}) & ; \ 0 \leq \mathcal{F}_W < 0.9999 \\ -4\,\mathcal{P}_W & ; \ 0.9999 \leq \mathcal{F}_W < 1, \end{cases} \tag{1.13}$$

We again follow PSO with another run of *fmincon* for a sanity check.

The reason we choose such cost function is inspired by how we usually evaluate the performance of a given gate operation—fidelity is a relatively *forgiving* metric, and so one needs to push this number as close to one as possible to obtain visually appealing solutions. As an example, consider the implementation of a Hadamard gate (also known as the balanced beamsplitter). The ideal transformation can be described as $U = \frac{1}{\sqrt{2}} \begin{pmatrix} 1 & 1 \\ 1 & -1 \end{pmatrix}$, and suppose our experimental transformation is $W = \begin{pmatrix} \sqrt{t} & \sqrt{r} \\ \sqrt{r} & -\sqrt{t} \end{pmatrix}$ with t^2 and r^2 representing the beamsplitter transmissivities and reflectivites. A beamsplitter with reflectivies (transmissivities) as bad as 40% (60%) still retains a fidelity $\sim 99\%$!

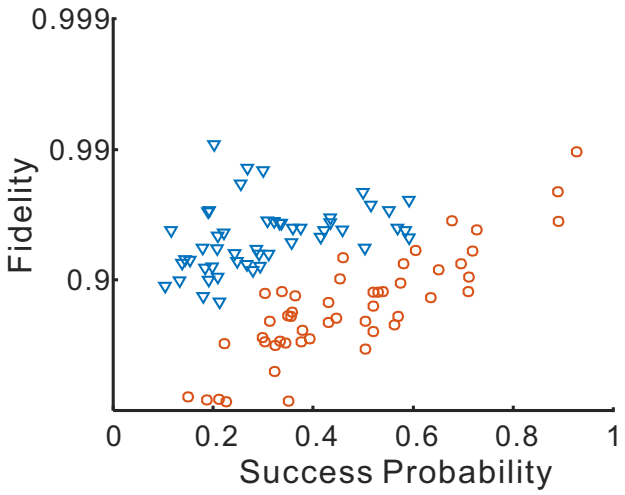

Fig. 1.4. **Algorithm comparison.** Scatter plots of the solutions obtained from 50 independent trials of *fmincon* (blue) and PSO (red) optimization. The average runtimes for *fmincon* and PSO are 22 ± 4 and 95 ± 60 seconds per trial, respectively.

1.3.4 Method Comparison

It is indeed difficult to compare the performance of aforementioned methods in all possible problems. Here we revisit one of the examples, where we are searching for the solutions for 7-dimensional DFT gates on a 2EOM/1PS QFP driven by $p = 6$ tones. We describe the pulse shaper transformation with a 64×64 diagonal matrix while only updating the 32 pulse shaper phases in the middle (setting other 32 as zero), and limit the maximum RF amplitude to 5 rad. Figure 1.4 plots the comparison between the methods discussed in Section 1.3.1 and 1.3.3. Across 50 independent trials, *fmincon* cannot find any decent solution, while PSO manages to find one.

See Appendix A for a detailed list of simulation results.

2. ELECTRO-OPTIC FREQUENCY BEAM SPLITTERS AND TRITTERS

2.1 Background

The coherent translation of quantum states from one frequency to another via optical nonlinearites has been the focus of considerable research since the early 1990s [66, 67]; yet only fairly recently have such processes been explored in the more elaborate context of time-frequency quantum information processing (QIP). Important examples include the quantum pulse gate [68, 69], which uses nonlinear mixing with shaped classical pulses for selective conversion of the time-frequency modes of single photons [70–73], and demonstrations of frequency beamsplitters based on both $\chi^{(2)}$ [33, 34] and $\chi^{(3)}$ [35, 36] nonlinearities. These seminal experiments have shown key primitives in frequency-based QIP, but as we discussed in Chapter 1, many challenges still remain.

In the previous chapter, we have described a fundamentally distinct platform for frequency-bin manipulations, relying on electro-optic phase modulation and Fourier-transform pulse shaping for universal QIP [12]. Our approach requires no optical pump fields, is readily parallelized, and scales well with the number of modes. In this chapter, we apply this paradigm to experimentally demonstrate the first electro-optic-based frequency beamsplitter. Our frequency beamsplitter attains high fidelity, operates in parallel on multiple two-mode subsets across the entire optical C-band (1530-1570 nm), and retains excellent performance at the single-photon level. Moreover, by incorporating an additional harmonic in the microwave drive signal, we also realize a balanced frequency tritter, the three-mode extension of the beamsplitter. This is the first frequency tritter demonstrated on any platform, and establishes our electro-optic approach as a leader for high-dimensional frequency-based QIP. Com-

bined with its native parallelizability and absence of optical noise sources, our mixer design offers new opportunities for a range of quantum information applications, including linear-optical computation [12], quantum cryptography [74], high-dimensional quantum communication [75], and quantum state transfer between two dissimilar matter qubits [76, 77]. The tritter also serves as an elementary building block for a frequency version of three-mode directionally-unbiased linear-optical multiports [78], which find application in quantum simulations [79], and substantially reduce the required hardware resources for complex quantum walks [80].

2.2 Hadamard Gate: Frequency Beamsplitter

For our first experimental demonstration, we focus on the 50/50 beamsplitter with phases chosen to match the Hadamard gate:

$$U_{2\times 2} = \frac{1}{\sqrt{2}} \begin{pmatrix} 1 & 1 \\ 1 & -1 \end{pmatrix}, \tag{2.1}$$

the top row corresponding to mode 0 (ω_0) and the bottom to mode 1 (ω_1). The major improvement from our original solution in [12], which results in a more practical experimental setup, is the usage of only phase-shifted sinewaves as the electro-optic modulation functions—rather than arbitrary waveforms—theory still predicts $\mathcal{F}_W = 0.9999$ and $\mathcal{P}_W = 0.9760$. This near-ideal performance even with such simple microwave modulation represents a major theoretical advance in terms of practicality and scalability, removing the need for a high-bandwidth arbitrary waveform generator (AWG) to realize the Hadamard gate. The numerical optimized solutions can be found in Fig. 2.6(a-b), followed by more detailed discussions in Chapter 2.5.

In our experimental scheme (shown in Fig. 2.1), the preparation of input states, frequency mixing, and detection of the final output states are all built on commercial fiber-optics instrumentation, such as modulators, pulse shapers and single-photon counters. A tunable continuous-wave (CW) laser operating in the C-band is firstly sent to an intensity modulator (IM; Photline MX-LN-40) driven at 25 GHz, which

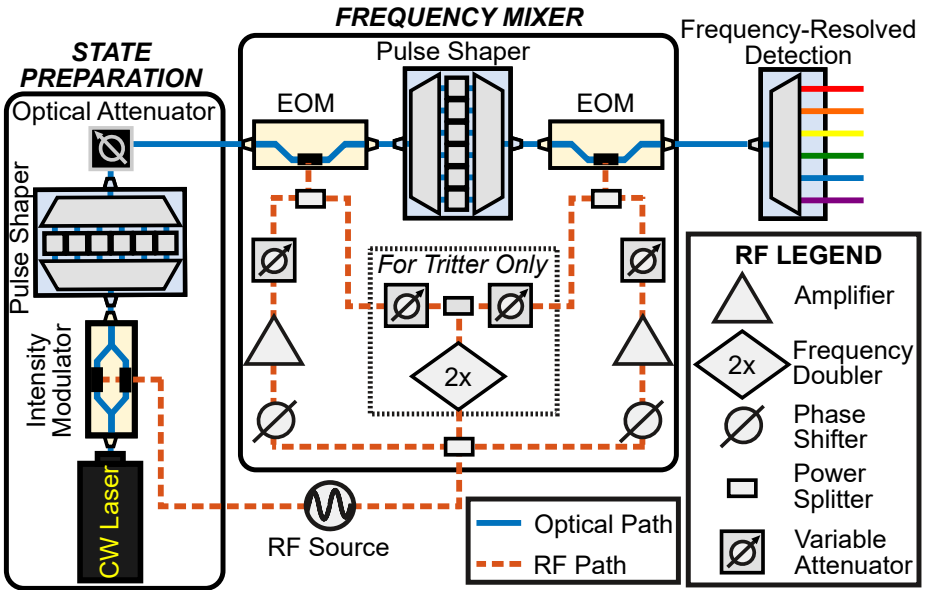

Fig. 2.1. **Experimental setup of frequency beamsplitter and tritter implementation.** Different input frequency superpositions are prepared in the form of electro-optic frequency comb (state preparation stage) and sent to an 2EOM/1PS QFP circuit for single-qudit frequency-bin operations (frequency mixer stage). The final output state is either characterized with an optical spectrum analyzer, or frequency-demultiplexed by a wavelength-selective switch and measured with an InGaAs single-photon avalanche photodiode.

creates a total number of three frequency bins with a spacing of 25 GHz[1]. The subsequent pulse shaper (Finisar WaveShaper 1000S)—which possesses ∼10-GHz spectral resolution, 1-GHz addressability, with operating wavelength from 1527.4 nm to 1567.5 nm—then performs amplitude and phase filtering to prepare either pure mode or superposition states as input to the following frequency mixer. We use an RF oscillator (Agilent E8257D) to generate a 25-GHz sinewave, and split it three ways feeding amplifiers for the first IM for state preparation and the two 40-Gb/s EOMs (EOSpace) of the QFP. Accurate control of the amplitude and the timing of RF signals is achieved by the usage of variable attenuators and phase shifters, by which we fine tune every

[1]The use of an intensity, rather than phase, modulator was purely from equipment availability: a phase modulator would produce many more comblines with greater efficiency, but the IM suffices for the number of modes needed in this experiment.

RF component until we have correlation above 99.9% between the experimentally obtained intensity spectrum after each EOM and the theoretical prediction. With estimated EOM half-wave voltages of $V_\pi = 5.37$ V at 25 GHz, the total RF power required at each EOM for the solution in Fig. 2.6(a) is roughly 12.9 dBm.

The central pulse shaper (another Finisar Waveshaper) applies the numerically optimized spectral phase pattern [Fig. 2.6(b)] for the Hadamard gate. The ∼10-GHz spectral resolution of this pulse shaper ultimately limits the tightest frequency-mode spacing (and thus total number of modes) we can utilize in our setup; experimentally we have found detectable reduction in $\mathcal{F}_W$ and $\mathcal{P}_W$ for spacings below ∼18 GHz. To characterize the full frequency-bin multiport, we probe it with an electro-optic frequency comb, and utilize an optical spectrum analyzer (OSA; Yokogawa) to obtain output spectra for different input frequency superpositions. This coherent-state-based characterization algorithm represents the analogue of the spatial version proposed and demonstrated in [81], applied here for the first time to frequency modes[2]. We also adopt the convention [81] which specifies zero phase as the input superposition state that maximizes the power in the zeroth frequency bin of the output; the phase values of any subsequent state (as set by the state preparation pulse shaper in Fig. 2.1) are thus only defined relative to this operating point. At a center wavelength of 1545.04 nm ($\omega_0 = 2\pi \times 194.036$ THz), we measure fidelity $\mathcal{F}_W = 0.99998 \pm 0.00003$ and success probability $\mathcal{P}_W = 0.9739 \pm 0.0003$, where error bars give the standard deviation of five independent measurement sequences.

Fig. 2.2 shows four experimentally recorded input/output combinations: the top row shows the equi-amplitude superpositions resulting from input in either mode 0 or mode 1; the second row reveals the single-wavelength output with the input in the superposition states $|\alpha_{\omega_0}(\pm\alpha)_{\omega_1}\rangle$.[3] The small bumps in adjacent modes -1 and $+2$ reflect the nonunity success probability, a limitation which—as noted above—could

[2]The detailed matrix reconstruction procedures and example of obtained transformation matrices are discussed in Appendix B

[3]Expressed in the form of coherent state. For example, $|\alpha_{\omega_0} 0_{\omega_1}\rangle$ denotes a coherent state $|\alpha\rangle$ of a known intensity $|\alpha|^2$ in the mode 0.

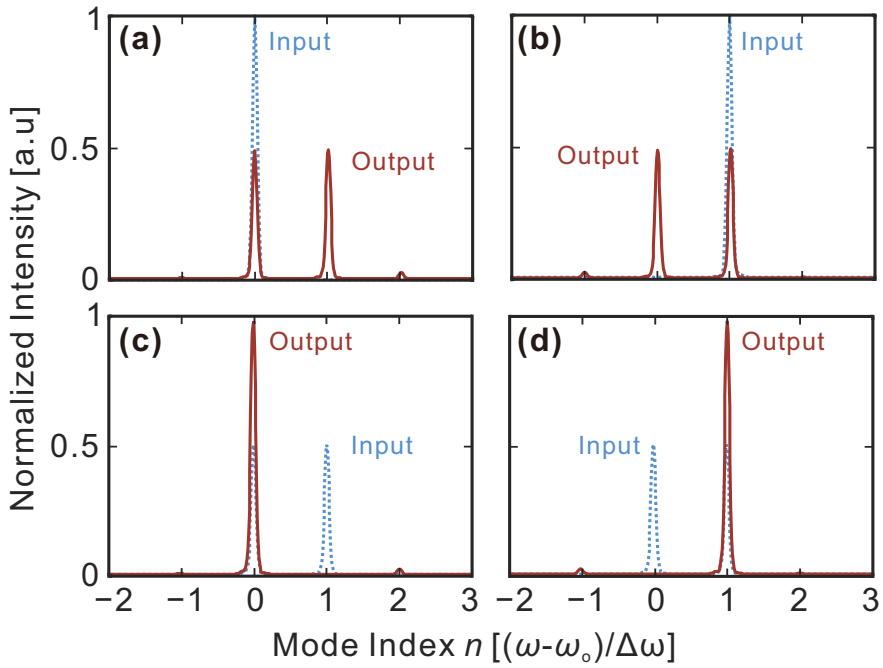

Fig. 2.2. **Experimentally obtained beamsplitter (Hadamard gate) output spectra for specific coherent state inputs.** Modes 0, and 1 denote the computational space. (a) Pure mode 0: $|\alpha_{\omega_0} 0_{\omega_1}\rangle$. (b) Pure mode 1: $|0_{\omega_0} \alpha_{\omega_1}\rangle$. (c) Mode 0 and mode 1 in phase: $|\alpha_{\omega_0} \alpha_{\omega_1}\rangle$. (d) Mode 0 and mode 1 out of phase: $|\alpha_{\omega_0} (-\alpha)_{\omega_1}\rangle$. The small bumps outside of the computational space (e.g., in mode -1 and 2) signify the nonunity success probability ($\mathcal{P}_W \approx 0.97$) due to the usage of a pure sinewave phase modulation.

be removed by more sophisticated modulation waveforms. And even in the current arrangement with $\mathcal{P}_W \approx 0.97$, the impact such residual scattering could have on gates downstream—i.e., by coupling back into the computational space and introducing errors—can be eliminated, either by using an additional pulse shaper to selectively attenuate these modes, or by sending them to a fiber tap for detection.

A crucial claim in favor of our beamsplitter is its suitability for parallelization. Ironically, the very characteristic which precludes a deterministic frequency beamsplitter using a single EOM—frequency-translation invariance—enables nearly effortless parallelization. We utilize the central pulse shaper to apply a dispersion of -0.4

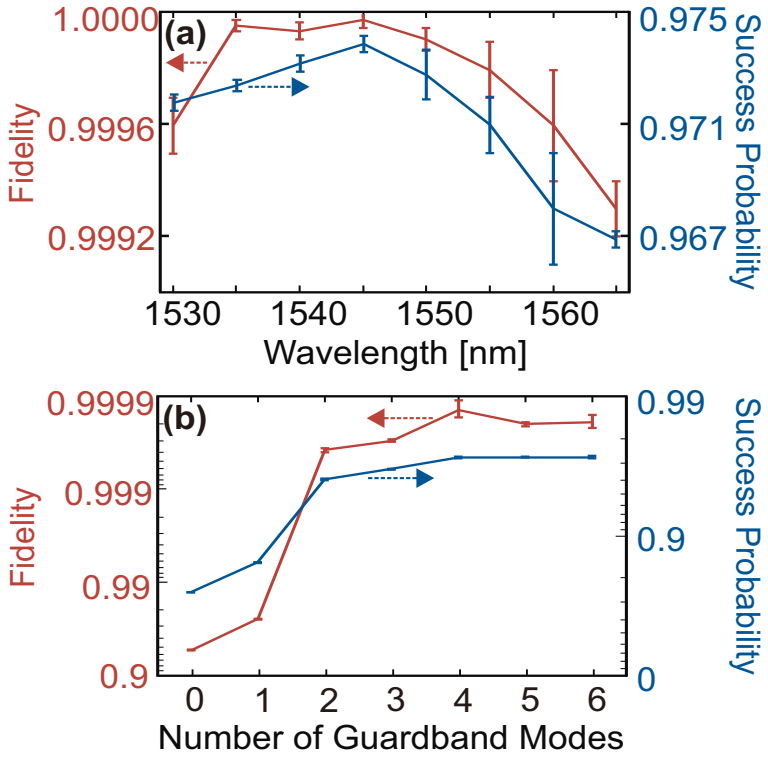

Fig. 2.3. **Implementation of parallel beamsplitters.** (a) Fidelity and success probability as a function of center wavelength. The wavelength of the central gate mode is scanned in 5-nm increments over the full C-band. (b) Parallel beamsplitter performance against frequency separation. The fidelity and success probability for the collective operation are investigated with respect to the number of guardband modes between two parallel beamsplitters.

ps/nm, properly compensating all frequency-dependent delay between the two EOMs (including the residual dispersion in the pulse shaper itself), and thus ensure proper timing between EOMs across the full C-band. Otherwise, the beasmplitter would not be able to preserve the correct split ratio for all parallel gates *simultaneously*. We then scan the wavelength of the central gate mode in 5-nm increments and measure $\mathcal{F}_W$ and $\mathcal{P}_W$ at each step over the full C-band. Fig. 2.3(a) shows that the fidelity exceeds 0.9990 for all test points, and the success probability does not drop below 0.965.

A second question, complementary to the total acceptance bandwidth, is the minimum frequency spacing: how close can two single-qubit gates be placed without performance degradation? Since sidebands adjacent to the computational space are populated mid-calculation, one would expect that a finite number of dark, guard-band modes are required to prevent cross-contamination. We address this question experimentally by implementing two beamsplitters in parallel and characterizing the total operation as a function of the number of initially empty modes between mode 1 of the low-frequency gate and mode 0 of the higher frequency one. The fidelity and success probability for the collective parallel operation are plotted in Fig. 2.3(b); they reach their asymptotic values for separations of just four modes. Combined with the 40-nm (5-THz) bandwidth of Fig. 2.3(a) and the 25-GHz mode spacing, these results imply that the present system can realize 33 frequency beamsplitters in parallel—a remarkable indication of the promise of our approach in scalable QIP.

2.3 Toward High Dimension: Frequency Tritter

Thus far, quantum frequency mixers have focused on the basic two-mode case [33–36], yet the inherent high dimensionality of frequency-bin states makes them well-suited for more complex qudit operations as well. Accordingly, generalizing mode mixers to dimensions beyond $d = 2$ represents an important milestone for frequency-based QIP. For $d = 3$, the most natural operation is the uniform frequency tritter—the frequency analogue of a 3×3 spatial coupler with equal split ratios [82], which has been shown to enable fundamentally richer quantum physics than the two-mode case [83]. For our purposes, a particularly convenient operation satisfying the equi-amplitude requirement is the 3-point discrete Fourier transform (DFT):

$$U_{3\times3} = \frac{1}{\sqrt{3}} \begin{pmatrix} 1 & 1 & 1 \\ 1 & e^{2\pi i/3} & e^{4\pi i/3} \\ 1 & e^{4\pi i/3} & e^{2\pi i/3} \end{pmatrix}. \tag{2.2}$$

Numerically, we find that incorporating an additional harmonic in the EOM drive signals allows our current configuration to reproduce the above frequency tritter with predicted fidelity $\mathcal{F}_W = 0.9999$ and success probability $\mathcal{P}_W = 0.9733$. The fact that the modulation remains so simple even for the tritter operation—consisting of the sum of just two phase-shifted sinewaves—again manifests the fortuitous practicality of our Fourier-series approach, beyond even the original proposal which relied on specialized RF waveforms [12]. Numerical obtained solutions can be found in Fig. 2.6(c-d), again followed by discussions regarding the scalability of the QFP in Chapter 2.5.

Experimentally, we incorporate an RF frequency doubler (Spacek Labs AQ-2X) into the setup (see dotted box in Fig. 2.1) to produce the necessary second harmonic signal. Due to a combination of doubling efficiency and loss in current microwave components, we also reduce the drive frequency—and hence, mode spacing—from 25 GHz to 18.1 GHz, for a doubled component at 36.2 GHz [4]. Considering the predicted EOM half-wave voltages at 18.1 and 36.2 GHz ($V_\pi = 4.78$ and 6.02 V, respectively), the expected RF power at the input of each EOM is 14.1 dBm at 18.1 GHz and 7.89 dBm at 36.2 GHz. Also, because of the relative difficulty to manually phase shift both harmonics synchronously, we set the relative phase of the two combined frequencies on both EOMs independently, then match the overall delay between EOMs by applying additional linear spectral phase on the central pulse shaper.

Running the coherent-state-based characterization algorithm [81], we measure fidelity $\mathcal{F}_W = 0.9989 \pm 0.0004$ and success probability $\mathcal{P}_W = 0.9730 \pm 0.0002$, again extremely close to theoretical predictions. Fig. 2.4 plots several important input/output spectra: for any single-line input, the output exhibits equal lines in the same three modes; conversely, three-mode input superpositions of the appropriate phases excite single lines at the output. This high-fidelity, balanced frequency tritter—the first of its kind—confirms that our electro-optic technique scales well to higher dimensions, with only a minor increase in the system complexity.

[4] Higher frequencies could be obtained by using appropriate V-band (40-75 GHz) hardware

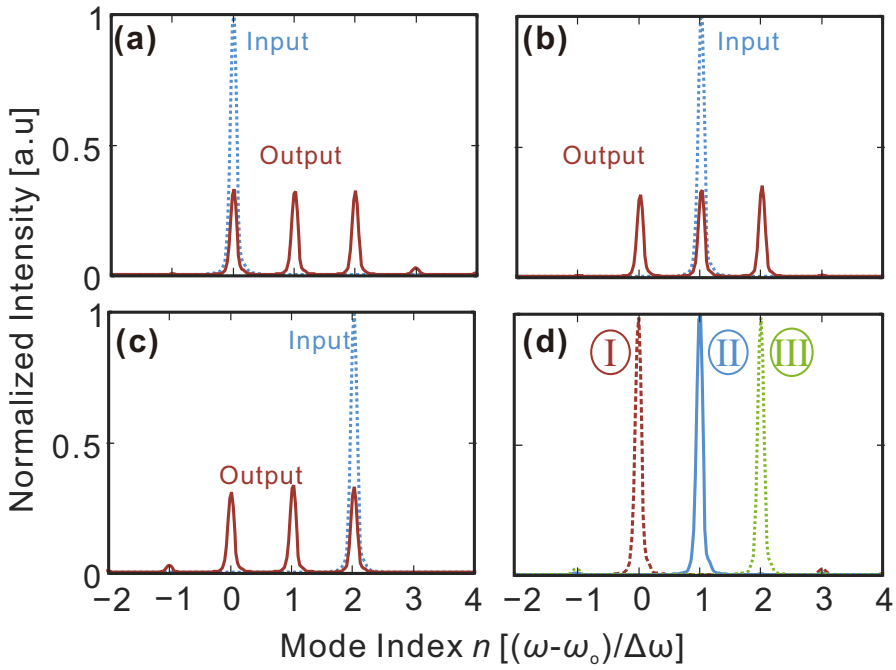

Fig. 2.4. **Experimentally obtained tritter output spectra for specific coherent-state inputs.** Modes 0, 1, and 2 denote the computational space. (a) Pure mode 0: $|\alpha_{\omega_0} 0_{\omega_1} 0_{\omega_2}\rangle$. (b) Pure mode 1: $|0_{\omega_0} \alpha_{\omega_1} 0_{\omega_2}\rangle$. (c) Pure mode 2: $|0_{\omega_0} 0_{\omega_1} \alpha_{\omega_2}\rangle$. (d) Outputs for the superposition state input $|\alpha_{\omega_0}(e^{-i\phi}\alpha)_{\omega_1}(e^{-2i\phi}\alpha)_{\omega_2}\rangle$ for: (I) $\phi = 0$, (II) $\phi = 2\pi/3$, and (III) $\phi = 4\pi/3$.

2.4 Single-photon Level Operation

Finally, to verify that these frequency mode mixers maintain performance at the single-photon level, we attenuate the input state $|\alpha_{\omega_0}(e^{-i\phi}\alpha)_{\omega_1}\rangle$ for the beamsplitter and $|\alpha_{\omega_0}(e^{-i\phi}\alpha)_{\omega_1}(e^{-2i\phi}\alpha)_{\omega_2}\rangle$ for the tritter to ∼0.1 photons per detection window at the gate input (i.e., before loss through the frequency mixer) and scan the input phase ϕ. The output state is frequency-demultiplexed by a wavelength-selective switch (WSS; Finisar WaveShaper 4000S), and measured by an InGaAs single-photon avalanche photodiode[5]. The resulting interference patterns for these weak coherent

[5]Beamsplitter: Aurea SPD_AT_M2, 1-ns gate @1.25 MHz, 20% efficiency, and ∼400 dark counts/s. Tritter: ID Quantique id-200, 2.5-ns gate @4 MHz, >10% efficiency, and ∼150 dark counts/s

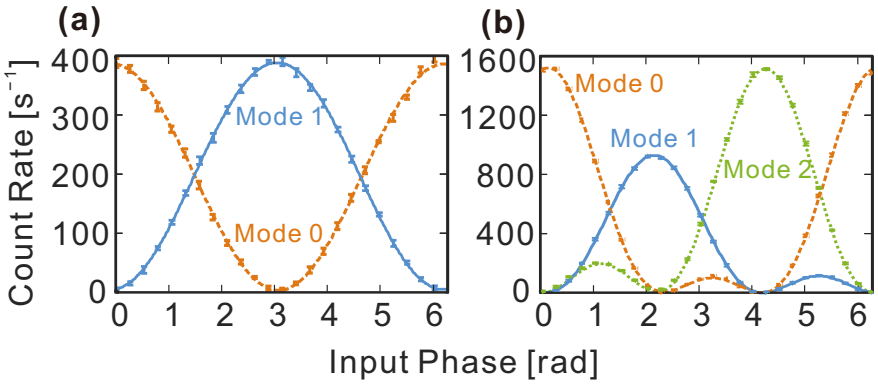

Fig. 2.5. **Spectral interference with weak coherent states.** (a) Output count rates for the two modes of the beamsplitter, as the phase ϕ of the single-photon-level state $|\alpha_{\omega_0}(e^{-i\phi}\alpha)_{\omega_1}\rangle$ is scanned. (b) Counts for the three output modes of the frequency tritter as the phase ϕ of the three-mode state $|\alpha_{\omega_0}(e^{-i\phi}\alpha)_{\omega_1}(e^{-2i\phi}\alpha)_{\omega_2}\rangle$ is scanned. The plotted best-fit curves are Fourier series of the form $\sum_n A_n \cos(n\phi + B_n)$, summed from $n = 0$ to 1 for (a), and $n = 0$ to 2 for (b).

states allow us to predict operation fidelity for true single-photon states as well. This follows because the gate itself is a *one-photon* operation, and thus the interference visibility depends only on the average flux and any extra noise introduced by the gate—not on the photon number statistics of the input.

Fig. 2.5(a) plots the counts in modes 0 and 1 for the beamsplitter, after subtracting the average detector dark count rate (error bars give the standard deviation of five repeated measurements). Moving on to the three-mode case, we obtain the detection rates for modes 0, 1, and 2 shown in Fig. 2.5(b). The oscillations now trace a sum of two sines, with respective peaks at $\phi = 0, 2\pi/3$, and $4\pi/3$, as expected for the ideal matrix in Eq. (2.2). The reduced flux for mode 1 is primarily due to the WSS, as its 12.5-GHz channel specificity do not match the 18.1-GHz line spacing; in our filter definitions, the center of mode 1 is close to one passband edge, and thereby experiences an additional ∼1-dB attenuation. Overall, both the beamsplitter and tritter perform exceptionally well at the single-photon level, with detector-dark-count-subtracted visibilities from 97-100%. Such low-flux visibilities far exceed those of

previous $\chi^{(2)}$ or $\chi^{(3)}$ frequency beamsplitters, which suffer from optical noise generated by the powerful pump fields; our approach inherently contributes no excess noise photons, making it particularly well-suited for quantum applications.

2.5 Simulations: Scalability of the QFP

As we mentioned earlier in Chapter 1.3, the numerical optimization procedures start with discretizing each temporal and spectral modulation into an $M \times M$ matrix, computing the transformation matrix V, and searching for solutions which maximize $\mathcal{P}_W$ while constraining $\mathcal{F}_W > 0.9999$. In the simulation, we choose $M = 128$ ($M \gg d$) such that the numerically computed V provides an accurate approximation to the physical transformation.

Here we record the specific solutions for the pulse shaper and each EOM in the optimal frequency beamsplitter and tritter. Figs. 2.6(a) and (b) show the results for the frequency beamsplitter, with $\mathcal{F}_W = 0.9999$ and $\mathcal{P}_W = 0.9760$. The temporal phases on both EOMs are just phase-shifted sinewaves driven by a single RF tone. In addition, the spectral phase on the pulse shaper, shown in Fig. 2.6(b), turns out to be a step function with a π-phase jump between mode indices 0 and 1, readily implemented in the line-by-line pulse shaping scheme.

The solution for the frequency tritter is presented in Figs. 2.6(c) and (d). We incorporate an additional RF harmonic to both EOMs while maintaining the three-element setup, and numerically we achieve $\mathcal{F}_W = 0.9999$ and $\mathcal{P}_W = 0.9733$. As shown in Fig. 2.6(c), the temporal phases are still time-shifted replicas, but now composed of two harmonics. The introduction of the additional harmonic couples more optical power to high-frequency modes, and relatively more complicated spectral phase control is needed for the frequency tritter, as plotted in Fig. 2.6(d). Note that both solutions are achievable experimentally: the maximum temporal phase shifts [Figs. 2.6(a) and (c)] are well within values available from commercial EOMs, and the number of frequency modes requiring spectral shaping is $\lesssim 20$ [Figs. 2.6(b) and

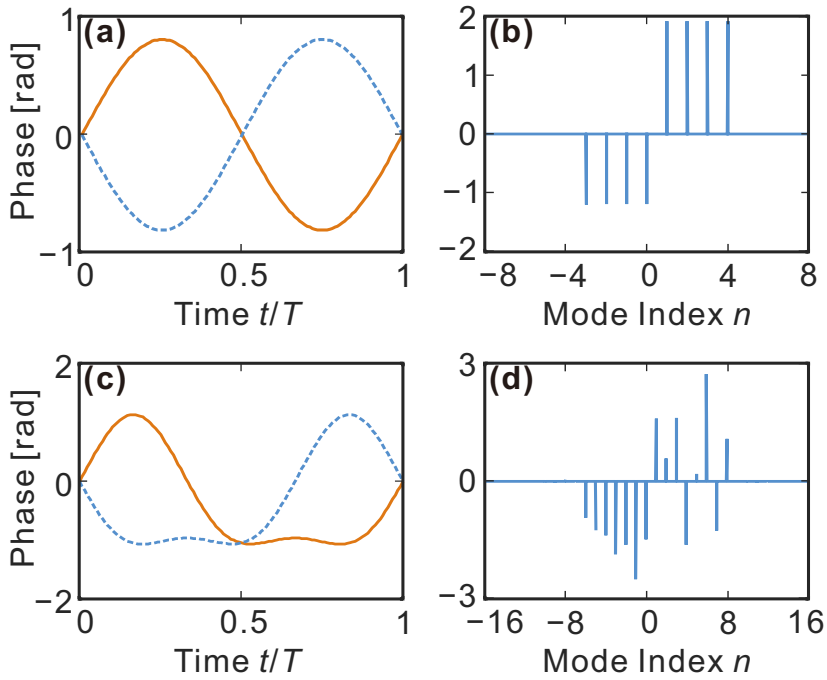

Fig. 2.6. **Hadamard and three-dimensional DFT gate design.** Numerical solutions for the time-frequency phases required to implement optimal beamsplitter and tritter on a 2EOM/1PS QFP circuit. For the frequency beamsplitter: (a) temporal phase modulation applied to the first EOM [solid red] and second EOM [dotted blue], plotted over one period T; (b) phases applied to each frequency mode by the PS, where modes 0 and 1 denote the computational space. For the frequency tritter: (c) temporal phase modulation for first [solid red] and second [dotted blue] EOM; (d) phases applied to each frequency mode by the PS, where now modes 0, 1, and 2 denote the computational space.

(d)]—much less than the full M-mode space, indicating 128 samples are fully sufficient to characterize the solution.

Furthermore, we discover a new recipe to implement high-dimensional DFT gates and found there to be a linear scaling between the number of harmonics and the dimensionality of DFT that can be implemented with high fidelity and success probability. Additional simulations show that this three-element setup can implement the frequency DFT up to $d = 10$ while maintaining $\mathcal{P}_W > 0.95$ with $\mathcal{F}_W \sim 0.9999$

constraint, using drive signals consisting of only $d-1$ single-frequency harmonics. To further quantify the experimental specifications (such as pulse shaper bandwidth), we take the optimal solution as the starting points, rerun the optimization while trimming down the accessible shaper bandwidth, and record the corresponding gate performance. These results are summarized in Figure 2.7, with each plot showing the performance of an d-dimensional DFT gate for a QFP with access to $d-1$ RF tones. The x-axis in each of these plots corresponds to the number of modes addressed by the pulse shaper. Such analysis is helpful for future designs of integrated QFPs under the system-level constraints imposed by integration and packaging, such as the maximum number of RF and DC connections. These findings indicate favorable scaling in our paradigm, effectively sublinear in the number of components (i.e., pulse shapers and EOMs) and preserving high $\mathcal{F}_W$ and $\mathcal{P}_W$. If we consider an integrated pulse shaper where each frequency channel can be realized with two microring resonators (MRRs) [84], our preliminary results in Fig. 2.7 suggests the total number of MRRs scales linearly with the the dimensionality of DFT.

Another approach one can envision to extend toward higher dimension is increasing the total number of components (Q), i.e., cascading additional EOMs and PSs, for complexity. Our recent work [61] investigate the required resource for frequency broadcasting operation in a wavelength-division multiplexed optical network for classical communication, in which we adopt the same numerical optimization approaches to simulate high-dimensional DFT operations with QFPs, and finds a linear scaling of Q with the network size d (assumed single-sinewave modulation on all EOMs).

2.6 Outlook

In this chapter, we have described the experimental realization of a high-fidelity, intrinsically parallelizable quantum frequency mixer based on EO modulation and pulse shaping, and showcased its potential in operating quantum states beyond qubits. We have also discussed the scalability of the QFP in the previous section. To realize

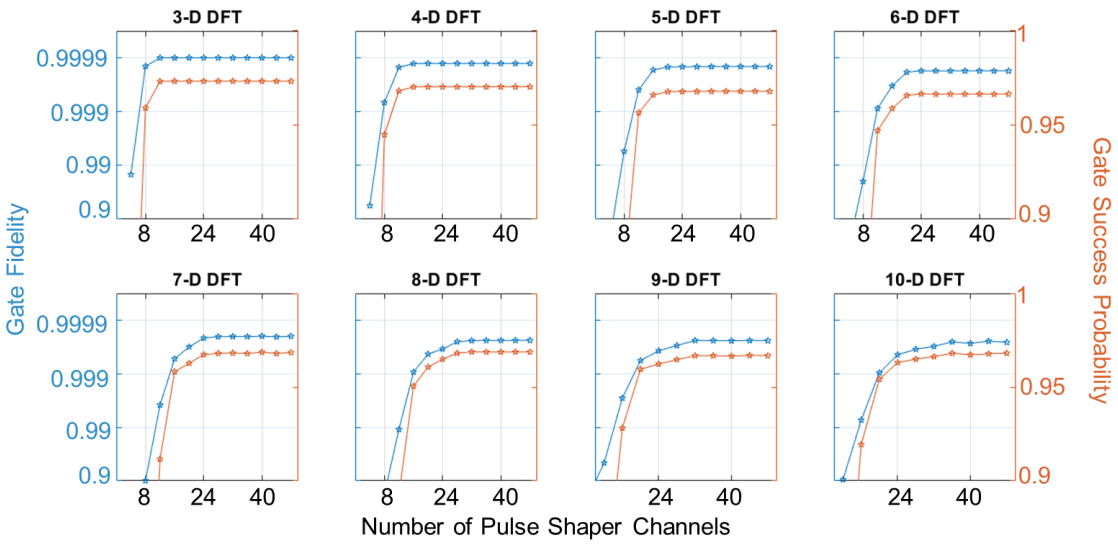

Fig. 2.7. **High-Dimensional DFT gate design.** Numerical simulation of high-dimensional discrete-Fourier transform (DFT) gates on a three-element QFP driven by $d-1$ RF tones. Fidelity and success probability as a function of number of pulse shaper channels.

more complex operations, we can either (i) introduce more harmonics in the temporal modulations or (ii) increase the total number of components.

Nevertheless, potential roadblocks could emerge for both methods. For (i), given the limited availability of high-speed RF components (AWG, amplifiers, phase shifters, attenuators, etc), it will be extremely valuable if the frequency-bin spacing can be reduced to a few GHz. This, however, will require advanced design for the BFC generation [85, 86], as well as the high-resolution spectral shaping. For (ii), on the other hand, the insertion loss from these off-the-shelf components, which already accounts for ∼12.5 dB in this three-element QFP[6], hampers the possibility of building larger circuits with the current designs. Importantly, though, frequency-bin encoding and the QFP operations themselves prove well suited for on-chip integration. EOM and pulse shaper photonic circuits have the potential to attain not only greater scalability,

[6]The EOMs contribute ∼2.8 dB each; the pulse shaper, ∼4.7 dB; and the remainder comes from fiber patch cord connections and polarization controllers.

but also better raw performance at the component level, than the discrete fiber-optic devices employed in experimental demonstrations thus far.

3. QUANTUM INTERFERENCE AND CORRELATION CONTROL OF FREQUENCY QUBITS

To establish our QFP as a reliable device for scalable QIP with frequency-encoded qubits, we must move beyond single-photon gates (irrespective of dimensionality), demonstrate verifiably quantum features relying on multiphoton interference, and apply *independent and distinct* gates to multiple qubits on demand in a low-noise and efficient fashion. In this Chapter, we demonstrate that tunable and independent single-frequency-qubit operations can be implemented in parallel on co-propagating qubits, thanks to the inherent parallelizability of the pulse shaper. Specifically, we realize a single-qubit operation which can be tuned smoothly between the identity $\mathbb{1}$ and Hadamard H gates, and can realize any combination thereof in parallel in the same device. We characterize this operation's tunability with frequency-bin Hong-Ou-Mandel (HOM) interference, obtaining 97% visibility for distinct frequency bins, the highest yet observed for photons of different colors. We then implement this operation as two separate quantum gates on frequency-bin qubits within the same fiber-optic mode, obtaining a high-fidelity flip of spectral correlations on two entangled photons. These demonstrations are considerably more impactful than what we present in Chapter 2 on frequency beamsplitters and tritters, for it exploits quantum entanglement (i.e., nonclassical two-qubit, rather than just single-qubit, effects) and realizes different operations in the same device simultaneously, rather than the *same* operation in parallel over many modes.

3.1 Overview

Fig. 3.1 sketches an example of processing co-propagating frequency-bin qubits in a parallel frequency processor, with the particular operations chosen to match the

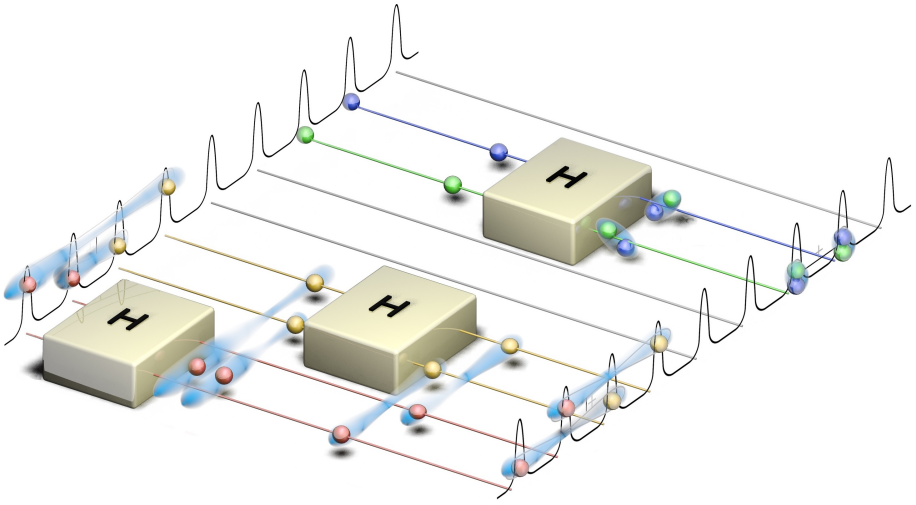

Fig. 3.1. **High-level vision of quantum frequency processor.** An input quantum state consisting of a superposition of photons (spheres) spread over discrete frequency bins propagates through a parallelized network of quantum gates (boxes) performing the desired set of operations. Spheres of a specific color represent the probability amplitudes of finding a *single photon* in a particular frequency mode– that is, an ideal measurement will result in precisely one click for each color. Frequency superpositions are represented by spheres straddling multiple lines, while entangled states are visualized by clouds. Two specific operations we realize experimentally are described here: Hong-Ou-Mandel interference between two spectrally distinguishable photons (top), and two-qubit rotation on a maximally-entangled frequency-bin Bell state (bottom).

experiments in this article. In general, an input quantum state consisting of frequency-encoded qubits is manipulated by the designed QFP network, which applies various unitary operations to combinations of frequency bins. Note that, although we draw each frequency bin as a separate "rail" for conceptual purposes, the physical encoding occurs within a single fiber-optic spatial mode, thereby enabling natural phase stability and providing compatibility with current fiber networks. After each step in the quantum frequency processor, a subset of modes could be extracted with optical add-drop multiplexers and measured, with the results used to update operations downstream. Any pair of distinct quantum gates which can be implemented in paral-

lel in our approach must satisfy two requirements: (i) their physical implementations must differ only in the spectral phase applied by each, since the temporal modulation is shared by all frequency-bin gates in a single spatial mode; and (ii) they must be able to be realized independently in two frequency bands without crosstalk. These considerations are general, holding for any proposed set of parallel gates. Yet in the particular example we consider here, a tunable frequency beamsplitter, we can connect these two requirements directly to non-classical phenomena of particular significance in quantum photonics: Hong-Ou-Mandel (HOM) interference [22] and the Einstein-Podolsky-Rosen (EPR) paradox [87].

In the conventional HOM interferometer, two photons mixed on a 50/50 spatial beamsplitter bunch, never exiting in different output ports. A general feature of bosons, HOM interference forms the basis of essentially all two-qubit gates in linear optics [88]. In our case, the overlap between frequency bins is set by the spectral phase of the quantum frequency processor, so that HOM interference relies precisely on the ability to tune a given operation through spectral phase control alone; in other words, high visibility provides confirmation of requirement (i) above. Similarly, quantum mechanics allows two particles to share a well-defined pure state even when the individual states of both particles are mixed. This property gives rise to EPR correlations when the joint state of the two particles is measured. While paradoxical to classical notions of reality [87], these correlations ultimately underpin Bell tests of nonlocality [89] and security in quantum key distribution [90]. Meeting requirement (ii) above signifies the ability to perform independent gates on entangled frequency-bin qubits. In particular, joint beamsplitter operations with different phases enable the realization of all combinations of Pauli Z and X basis measurements, which are sufficient for testing EPR correlations. Consequently, in the following experiments we utilize both quantum phenomena (HOM and EPR) as important test cases to assess gate performance.

3.2 Design a Tunable Frequency Beamsplitter

Before we move forward to discuss the results regarding HOM and EPR experiments in the following sections, we take a moment to describe how to implement this tunable frequency beamsplitter and how well we can control its reflectivity and transmissivity. The specific configuration for our Hadamard gate (cf. Chapter 2.5) relies on the temporal phase modulation $\varphi(t) = \pm\Theta \sin \Delta\omega t$ ($\Theta = 0.8169$ rad) on the first and second EOMs, respectively. And for a gate operating on bins 0 and 1, the discrete pulse shaper phases can be written as

$$\phi_n = \begin{cases} \phi_0 & ; n \leq 0 \\ \phi_0 + \alpha & ; n \geq 1. \end{cases} \tag{3.1}$$

Here ϕ_0 is an offset with no physical significance, while $\alpha = \pi$ for the ideal Hadamard, as shown in Fig. 3.2(a). Yet α can be tuned as well; doing so actually permits tunable

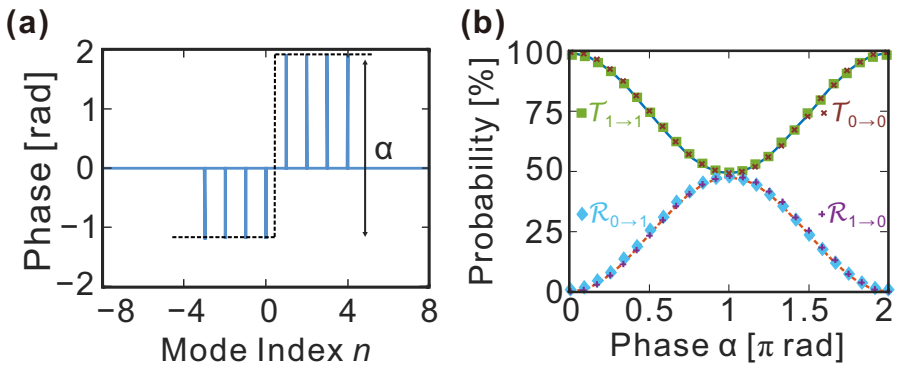

Fig. 3.2. **Tunable beamsplitter design.** Previously, the phase patterns to realize a frequency beamsplitter [See Chapter 2.5 and Figure 2.6 for details] consist of two π-phase-shifted sinewaves for the EO modulations, and a π-phase jump between the two computational modes on the pulse shaper. (a) By simply changing the depth of the phase shift α on the shaper while both EOM remain fixed, a beamsplitter with tunable reflectivities can be realized. (b) Beamsplitter reflectivities $\mathcal{R}$ and transmissivities $\mathcal{T}$ for all paths between frequency bins 0 and 1, as pulse shaper phase shift [α in (a)] is tuned. Markers denote the values measured with a laser probe, while curves give the theory.

reflectivity[1]. Specifically, if we write out the 2×2 transformation matrix on modes 0 and 1 as a function of this phase,

$$V = \begin{bmatrix} V_{00}(\alpha) & V_{01}(\alpha) \\ V_{10}(\alpha) & V_{11}(\alpha) \end{bmatrix}, \tag{3.2}$$

we can define the variable reflectivities $\mathcal{R}$ (i.e., mode-hopping probabilities) and transmissivities $\mathcal{T}$ (probabilities of preserving frequency) as

$$\begin{aligned} \mathcal{R}_{0\to1} = |V_{10}(\alpha)|^2 &= \left|(1-e^{i\alpha})\sum_{k=1}^{\infty} J_k(\Theta)J_{k-1}(\Theta)\right|^2 \\ \mathcal{R}_{1\to0} = |V_{01}(\alpha)|^2 &= \left|(1-e^{i\alpha})\sum_{k=1}^{\infty} J_k(\Theta)J_{k-1}(\Theta)\right|^2 \\ \mathcal{T}_{0\to0} = |V_{00}(\alpha)|^2 &= \left|J_0^2(\Theta) + (1+e^{i\alpha})\frac{1-J_0^2(\Theta)}{2}\right|^2 \\ \mathcal{T}_{1\to1} = |V_{11}(\alpha)|^2 &= \left|e^{i\alpha}J_0^2(\Theta) + (1+e^{i\alpha})\frac{1-J_0^2(\Theta)}{2}\right|^2, \end{aligned} \tag{3.3}$$

where $J_k(\Theta)$ is the Bessel function of the first kind. We note that, when $\alpha = \pi$, the elements $\{V_{00}, V_{01}, V_{10}\}$ are all real and positive, while V_{11} is real and negative—in accord with the ideal Hadamard and leading to destructive HOM interference between the reflect/reflect and transmit/transmit two-photon probability amplitudes. Additionally, these expressions satisfy $\mathcal{R}_{0\to1} = \mathcal{R}_{1\to0} \equiv \mathcal{R}$ and $\mathcal{T}_{0\to0} = \mathcal{T}_{1\to1} \equiv \mathcal{T}$. As α is tuned over $0 \to \pi \to 2\pi$, $\mathcal{R}$ follows from 0 to a peak of 0.4781 and back to 0, while $\mathcal{T}$ starts at 1, drops to 0.4979, and returns to 1. The sum $\mathcal{R}+\mathcal{T}$ defines the gate success probability, which drops slightly at $\alpha = \pi$ due to the use of single-frequency electro-optic modulation. Fig. 3.2(b) plots the theoretically predicted (curves) and experimentally measured (symbols) beamsplitter transmissivities and reflectivities between bins 0 and 1, when probing the system with a laser and scanning the shaper phase. A phase setting of π results in an H gate; 0 and 2π phase shifts yield

[1]This design is inspired from the elegance of the numerically obtained solution. For $\alpha = \pi$, we have an Hadamard gate (H). While for $\alpha = 0$, it permits an identity gate ($\mathbb{1}$) as the EO modulations are simply π-phase-shifted sinewaves and will cancel out each other. We are then curious to know whether their is a smooth transition from $\mathbb{1}$ to H when α is tuned.

an $\mathbb{1}$ gate. It is important to emphasize that both EOMs remain fixed throughout the scan, so that the tunability is effected only by adjusting the phase applied by the pulse shaper.

3.3 Experimental Arrangement

Fig. 3.3(a) shows our setup for processing quantum information encoded in frequency. We couple a continuous-wave Ti:sapphire laser (M Squared) into a fiber-pigtailed periodically poled lithium niobite (PPLN; SRICO) waveguide, temperature

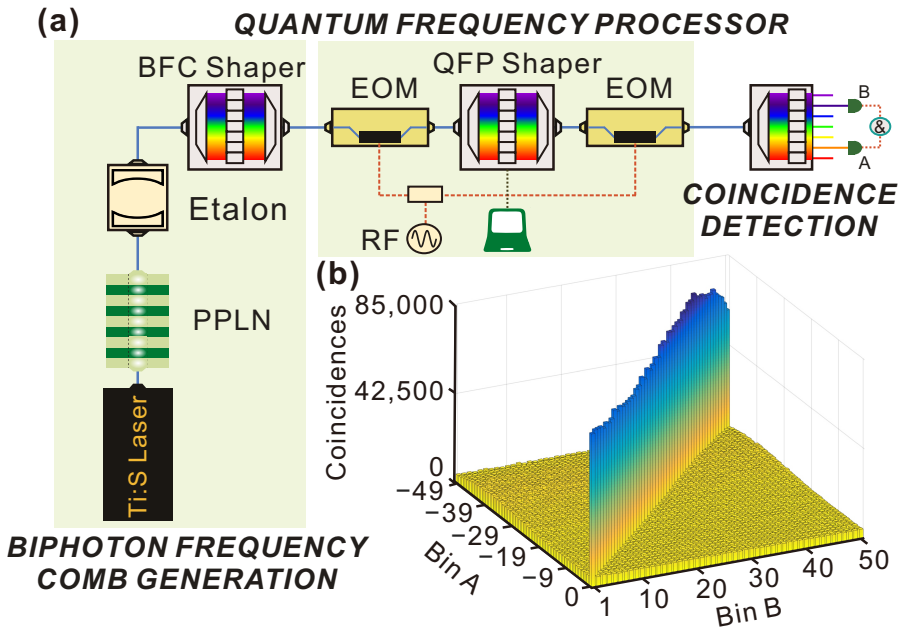

Fig. 3.3. **Processing biphoton frequency comb with QFP.** (a) Experimental configuration. A 25-GHz-spacing biphoton frequency comb (BFC) is generated via parametric down-conversion in a periodically poled lithium niobite (PPLN) waveguide followed by an etalon for spectral filtering. A wavelength-selective switch (WSS) is used to route photons in different frequency bins for coincidence detection. (b) Joint spectral intensity (JSI) measurement of the BFC source, measured with etalon output connected directly to coincidence detection setup (bypassing the central QFP). Strong correlations exist for frequency bin satisfying $n_A + n_B = 1$, whereas other combinations are at the expected accidental level. Counts are collected over 5 seconds.

controlled at ∼85°C for spontaneous parametric down-conversion under type-0 phase matching. Spectrally entangled photon pairs spanning >2.5 THz are subsequently filtered by a Fabry-Perot etalon (Optoplex) with 25 GHz mode spacing to produce a biphoton frequency comb (BFC), with each comb line possessing a full-width at half-maximum linewidth of 1.8 GHz. The center frequency of the pump laser is carefully locked to align the generated signal-idler pairs with etalon peaks, i.e., to maximize coincidences between the spectrally filtered modes. We utilize a pulse shaper (BFC shaper) to perform amplitude and phase filtering to prepare particular input states for quantum frequency processing. The resulting state is of the form $|\Psi\rangle = \sum_{n\geq 1} c_n |1_{\omega_{1-n}}\rangle_A |1_{\omega_n}\rangle_B$, where the coefficients c_n are set by the BFC shaper.

Each frequency-bin index n corresponds to the filter centered at $\omega_n = \omega_0 + n\Delta\omega$, where $\omega_0/2\pi = 193.6000$ THz and $\Delta\omega/2\pi = 25$ GHz. Party A is assigned all modes $n_A \in \{n \leq 0\}$, while the rest are given to B ($n_B \in \{n \geq 1\}$). The output photons are frequency-demultiplexed by an wavelength-selective switch (WSS) having 12.5 GHz channel specificity. Each time we route two different spectral modes (each takes up two pixels on the WSS) to two superconducting nanowire single-photon detectors (SNSPD; Quantum Opus) to record single counts as well as the coincidences within 1.5 ns bins. We plot the measured frequency correlations of this source [Fig. 3.3(b)], obtained by bypassing the central QFP, scanning the filters of the output WSS, and counting coincidences between two detectors. Over this 50×50 mode grid, we observe high coincidence counts only for frequency-bin pairs satisfying $n_A + n_B = 1$, as expected by energy conservation.

The central QFP, as we describer earlier, consists of a pulse shaper sandwiched between two high-speed EOMs driven by a 25 GHz sinusoidal voltage. This combination was shown to enable Hadamard operation with a measured 99.998% fidelity and only 2.61% photon leakage outside of the computational space [21], and is capable of realizing tunable beamsplitters simply by changing the phase pattern imparted on the QFP shaper, as discussed in the previous section.

3.4 Frequency-bin Hong-Ou-Mandel Interference

Hong–Ou–Mandel (HOM) interference [22] is the foundational quantum effect underlying two-qubit gates in the LOQC paradigm. In conventional HOM, one mixes two photons on a 50/50 spatial beamsplitter while scanning some parameter to control their overlap, observing photon bunching at the exit ports as a result of quantum interference between indistinguishable two-photon probability amplitudes; a visibility exceeding 50% indicates nonclassicality [22]. In the case of photons sharing a single spatial mode but different colors, the quantum interference can instead be realized with a frequency mixer [91] where, e.g., the distinguishability is controlled by introducing a temporal delay between the two input modes [33] or scanning the photon frequency spacing relative to that of the frequency beamsplitter [60, 92]. Here we adjust the mixing probability of the operation itself, as controlled by the phase scanned in Fig. 3.2(a), analogous to varying the reflectivity of a spatial beamsplitter.

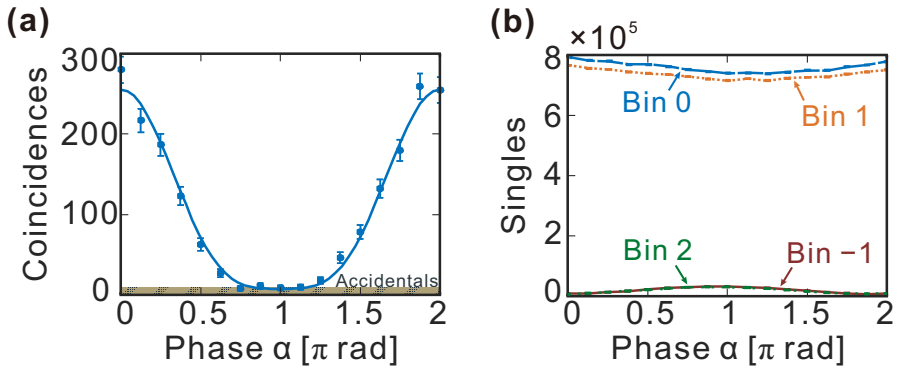

Fig. 3.4. **Frequency-bin Hong-Ou-Mandel (HOM) interference.** (a) Measured output coincidence counts (with no accidentals subtraction) between bins 0 and 1 given a two-photon state input $|1_{\omega_0}\rangle_A|1_{\omega_1}\rangle_B$. The solid curve is the theoretical prediction scaled and vertically offset to math the data points via linear least squares. The HOM visibility is 0.971 ± 0.007. (b) Registered single counts in bins 0, 1, and adjacent bins -1 and 2. Here detector dark counts are subtracted to compare output flux. For both (a) and (b), counts are recorded over 180 s, and error bars assume Poissonian statistics.

In this experiment, we prepare the input state in the form of $|\Psi\rangle \propto |1_{\omega_0}\rangle_A |1_{\omega_1}\rangle_B$ by filtering out all frequency-bin pairs in the BFC except for the first pair. A tunable beamsplitter, whose mode transformation V is defined in Eq. 3.3, is implemented on these two modes, 0 and 1. At the output of the beamsplitter, we measure the spectrally resolved coincidences between bin 0 and 1, i.e.,

$$C_{01} = \langle \Psi | \hat{b}_0^\dagger \hat{b}_1^\dagger \hat{b}_1 \hat{b}_0 | \Psi \rangle, \tag{3.4}$$

as well as the single counts in each output frequency bin

$$S_0 = \langle \Psi | \hat{b}_0^\dagger \hat{b}_0 | \Psi \rangle; S_1 = \langle \Psi | \hat{b}_1^\dagger \hat{b}_1 | \Psi \rangle, \tag{3.5}$$

where $\hat{b}_n$ denotes the annihilation operator in the frequency bin centered at ω_n after the gate operation (cf. Eq. 1.3). Plugging in Eq. 3.3, we thus predict the coincidences and singles while scanning the QFP shaper phase α:

$$\begin{aligned} C_{01} &= |V_{00}V_{11} + V_{01}V_{10}|^2 = |\mathcal{R}(\alpha) - \mathcal{T}(\alpha)|^2 \\ S_0 = |V_{00}|^2 + |V_{01}|^2 = S_1 &= |V_{10}|^2 + |V_{11}|^2 = \mathcal{R}(\alpha) + \mathcal{T}(\alpha) \\ S_{-1} = S_2 &\approx 1 - \mathcal{R}(\alpha) - \mathcal{T}(\alpha), \end{aligned} \tag{3.6}$$

where the nonunity success probability $[\mathcal{R}(\pi) + \mathcal{T}(\pi) = 0.976]$ results in some photons scattering into bins -1 and 2. The expression for C_{01} also perfectly describes the destructive interference between reflect/reflect and transmit/transmit two-photon probability amplitudes (cf. Eq. 3.3; V_{11} is negative, while other terms are positive).

The measured coincidence counts between output bins 0 and 1 are shown in Fig. 3.4(a). The solid curve is the theoretical prediction, scaled and vertically offset to match the data points via linear least squares; the visibility obtained from this fit is 0.971 ± 0.007, with the reduction from unity completely consistent with the accidentals level expected for our measured counts and timing resolution. This visibility far exceeds the previous values measured for frequency-domain HOM interference with-

out subtraction of accidentals[2]—namely, 0.71 ± 0.04 [33] and 0.68 ± 0.03 [92]. Such a significant improvement in visibility can be explained by the reduced optical noise present in our approach, compared to those relying on powerful pump fields, as well as the fine controllability of our operation, enabled by the purely electrical control parameters (i.e., microwave power/phase, and pixel voltages for the pulse shaper), which allows us to precisely optimize the spectral overlap between the two modes.

We also record the singles counts for bins 0 and 1, as well as the adjacent sidebands (-1 and 2). As shown in Fig. 3.4(b), the two central modes retain nearly constant flux across the full scan, showing that the dip in coincidence counts results from truly quantum HOM interference as opposed to photon loss. Moreover, the small reduction in singles counts around π—accompanied by the increase in singles counts for bins -1 and 2—also qualitatively matches expectations, given the fact that the full H gate scatters 2.61% of the input photons out of the computational space into adjacent sidebands. We note that even this scattering could be removed by driving the EOMs with more complicated waveforms [12].

3.5 Two-photon State Manipulation

Our quantum operation's tunability, invoked in the above realization of HOM interference, can then be applied to realize two different gates—that is, distinct pairs of $\mathcal{R}$ and $\mathcal{T}$ in Fig. 3.2(a)—by setting different phase shifts on appropriate subbands in the pulse shaper's bandwidth. To demonstrate this, we set the BFC shaper to filter out all modes except $\{-4, -3, 4, 5\}$, preparing the input entangled state $|\Psi\rangle \propto |1_{\omega_{-4}}\rangle_A |1_{\omega_5}\rangle_B + |1_{\omega_{-3}}\rangle_A |1_{\omega_4}\rangle_B$. The reason we have six initially empty modes between A and B is to make sure we can apply operations on both parties without any fear of the photon in A jumping over to B's modes, and vice versa (cf. guardband discussion in Chapter 2). On each pair of frequency bins—$\{-4, -3\}$ and $\{4, 5\}$—we set the

[2]Standard practice is to report visibility without accidentals subtraction as we have done in the main text. If the visibility presented here is accidentals subtracted, we will have ∼100% as the coincidence count reaches a minimum approximated to the expected accidentals level.

spectral phase to apply either the identity $\mathbb{1}$ or Hadamard H gates, and then measure coincidence counts between the frequency bins at the output. Accordingly, we can express the coincidence probability for any $(n_A \leq 0, n_B \geq 1)$ as

$$C_{n_A n_B} = \left| V_{n_A,-3} V_{n_B,4} + V_{n_A,-4} V_{n_B,5} \right|^2 . \tag{3.7}$$

This expression accounts for all aspects of the potentially non-ideal mode transformation. Focusing on the qubit modes ($n_A \in \{-4, 3\}, n_B \in \{4, 5\}$), we have the ideal coincidences under all four cases of Fig. 3.5 as:

$$\begin{aligned}
V(\mathbb{1}_A \otimes \mathbb{1}_B) \Longrightarrow \quad C_{n_A n_B}^{\mathbb{1}_A \otimes \mathbb{1}_B} &= \frac{1}{2} \left(\delta_{n_A,-3} \delta_{n_B,4} + \delta_{n_A,-4} \delta_{n_B,5} \right) \\
V(\mathbb{1}_A \otimes H_B) \Longrightarrow \quad C_{n_A n_B}^{\mathbb{1}_A \otimes H_B} &= \frac{1}{4} \left(\delta_{n_A,-3} \delta_{n_B,4} + \delta_{n_A,-3} \delta_{n_B,5} + \delta_{n_A,-4} \delta_{n_B,4} + \delta_{n_A,-4} \delta_{n_B,5} \right) \\
V(H_A \otimes \mathbb{1}_B) \Longrightarrow \quad C_{n_A n_B}^{H_A \otimes \mathbb{1}_B} &= \frac{1}{4} \left(\delta_{n_A,-3} \delta_{n_B,4} + \delta_{n_A,-3} \delta_{n_B,5} + \delta_{n_A,-4} \delta_{n_B,4} + \delta_{n_A,-4} \delta_{n_B,5} \right) \\
V(H_A \otimes H_B) \Longrightarrow \quad C_{n_A n_B}^{H_A \otimes H_B} &= \frac{1}{2} \left(\delta_{n_A,-4} \delta_{n_B,4} + \delta_{n_A,-3} \delta_{n_B,5} \right) ,
\end{aligned} \tag{3.8}$$

where δ_{nm} is the Kronecker delta function. These expressions predict perfect negative correlations for the case $\mathbb{1}_A \otimes \mathbb{1}_B$—i.e., detecting the low frequency of A occurs in coincidence with the high frequency of B, and vice versa —while positive correlations result for $H_A \otimes H_B$. For the other two cases, no frequency correlations are present, with all four combinations equally likely. The transition from $\mathbb{1}_A \otimes \mathbb{1}_B$ to $H_A \otimes H_B$ can flip the correlations entirely, eliminating the negative frequency dependence resulting from pump energy conservation in favor of a positive dependence.

Fig. 3.5 furnishes the results for all four combinations of $\mathbb{1}$ and H. When the two gates match, near-perfect spectral correlations result [(a) and (d)], whereas mismatched cases produce uniform population of the two-qubit space [(b) and (c)]. By measuring correlations in adjacent bins as well, we confirm the self-contained nature of our operation; even in the worst case [Fig. 3.5(d)], less than 6% of the total coincidences lie outside of the 2×2 subspace, whereas similar state manipulation with only one EOM suffers from high probability of qubit scattering [53, 54, 60]. The loss of photon energy to unwanted sideband modes is intrinsic to frequency-bin operations

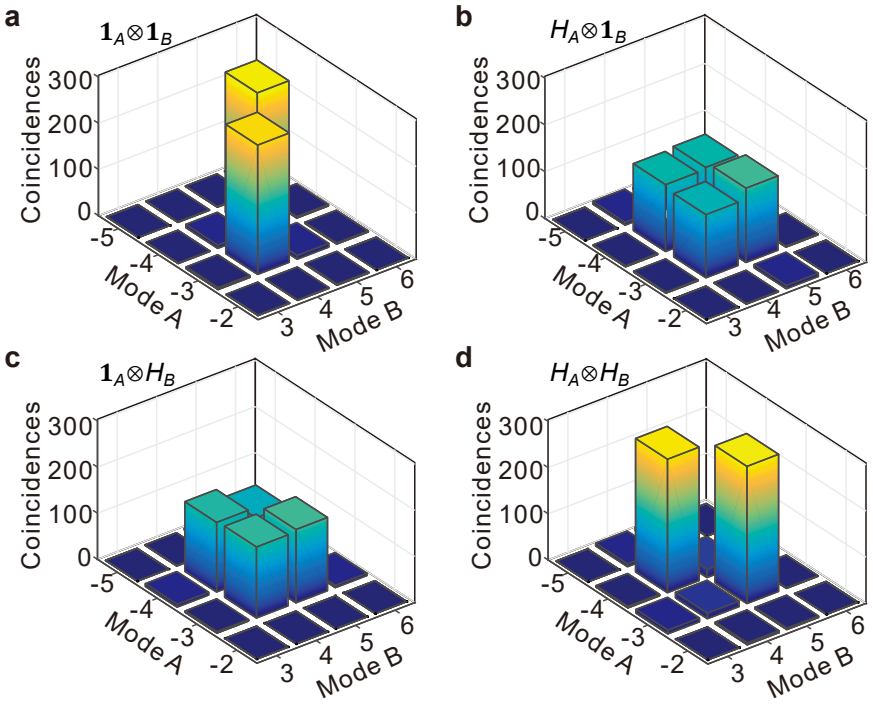

Fig. 3.5. **Two-photon state manipulation.** Coincidences between output frequency bins after application of the following gates on the input entangled state $|\Psi\rangle \propto |1_{\omega_{-4}}\rangle_A |1_{\omega_5}\rangle_B + |1_{\omega_{-3}}\rangle_A |1_{\omega_4}\rangle_B$: (a) identity operations on both photons; (b) Hadamard on photon A; (c) Hadamard on photon B; (d) Hadamard on both photons. The transition from $\mathbb{1}_A \otimes \mathbb{1}_B$ to $H_A \otimes H_B$ results in a high-fidelity flip of spectral correlations on two entangled photons. Coincidences are collected over 120 s.

based on a single EOM (see discussion in Chapter 1.2). Thus, they are inherently non-deterministic and can be viewed at best only as postselected single-photon gates. By contrast, the manipulations shown in Fig. 3.5 do represent frequency-bin gates in this proper sense, and thus offer potential in constructing more general quantum information processing networks. In particular, because our frequency-bin operations retain photons in their respective computational spaces, they can be concatenated in systems containing several successive gates, without the massive reduction in success probability inherent to previous approaches.

Moreover, the quality of our state manipulation can be analyzed by equivalently viewing the unitary *rotations* on our input state followed by coincidence detection as *measurements* of the state in bases other than computational. As one example, we can test the EPR-like nature of this state using the strong correlations in two mutually unbiased bases (MUBs) Z and X (gate operations $\mathbb{1}$ and H)[3].

We define the conditional entropies $\mathcal{H}(\mathbb{1}_A|\mathbb{1}_B)$ and $\mathcal{H}(H_A|H_B)$ as the uncertainty of the measured frequency mode of A $\{-4,-3\}$ given knowledge of B's result $\{4,5\}$, for the two cases of matched transformations [Fig. 3.5(a) and (d)]. Retrieving the probabilities from the raw counts via Bayesian mean estimation (BME) [93, 94] with no accidentals subtraction (See Appendix C.1 for detailed analysis), we recover

$$\begin{aligned} \mathcal{H}(\mathbb{1}_A|\mathbb{1}_B) &= 0.19 \pm 0.03 \\ \mathcal{H}(H_A|\mathbb{1}_B) &= 0.997 \pm 0.003 \\ \mathcal{H}(\mathbb{1}_A|H_B) &= 0.993 \pm 0.005 \\ \mathcal{H}(H_A|H_B) &= 0.29 \pm 0.04. \end{aligned} \tag{3.9}$$

As expected, the mismatched bases have near-maximal entropy (1 bit), while matched cases are much lower. This is similar to the concept behind entanglement-based QKD, where Alice and Bob share entangled photon pairs and perform local measurements using one of the MUBs; When they choose the same basis, Alice's measurement can perfectly predict Bob's and vice versa (i.e., zero conditional entropy), even though locally the results are completely random. Contrarily, when they choose different bases, their measurement results are completely decorrelated (i.e., maximal entropy).

The bipartite entanglement can be quantified by violation of the Maassen-Uffink bound for separable states: $\mathcal{H}(\mathbb{1}_A|\mathbb{1}_B)+\mathcal{H}(H_A|H_B) \geq q_{MU}$ [95,96], where the Maassen-Uffink bound q_{MU} depends on the overlap between the basis vectors in the rows of $\mathbb{1}_\mathbb{A}$ and H_A; for measurements with perfect MUBs in d-dimension, $q_{MU} = \log_2 d$ bit. In our case, the bound q_{MU} is computed to be 0.971, just smaller than 1 because of slight imbalance in our H operation. With the sum, $\mathcal{H}(\mathbb{1}_A|\mathbb{1}_B) + \mathcal{H}(H_A|H_B) = 0.48 \pm 0.05$,

[3]Applying unitaries H, $HS^\dagger$, and $\mathbb{1}$ followed by measurement in the computational basis are equivalent to perform Pauli-X, Y, and Z measurement, respectively; $S^\dagger$=[1,0; 0,-i]

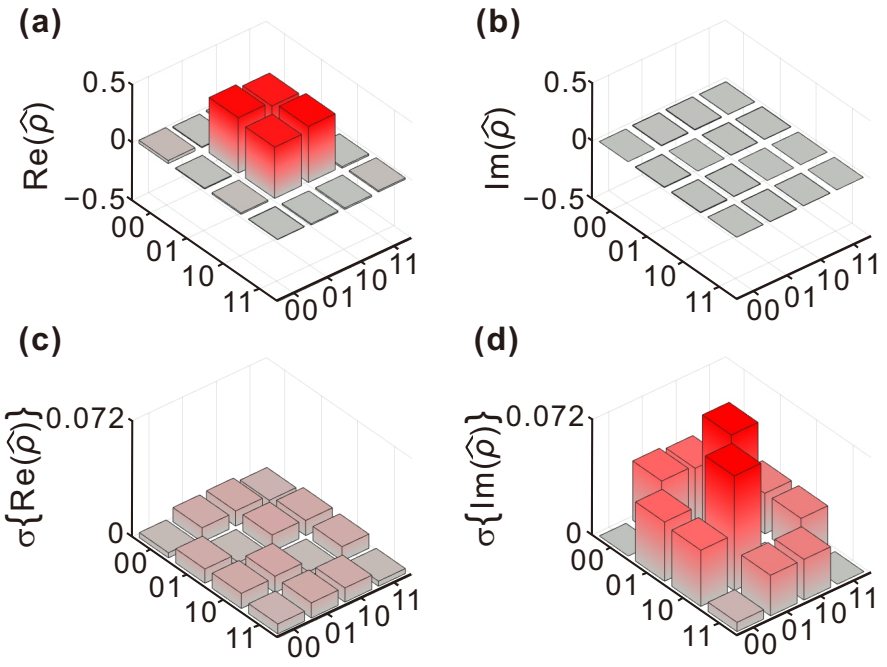

Fig. 3.6. **Reconstructed density matrix by BME.** (a) Real part of average density matrix. (b) Imaginary part. (c) Standard deviations of the real density matrix elements. (d) Standard deviations of the imaginary elements. Shorthand label definitions: $00 \equiv |1_{\omega_{-4}}\rangle_A|1_{\omega_4}\rangle_B$, $01 \equiv |1_{\omega_{-4}}\rangle_A|1_{\omega_5}\rangle_B$, $10 \equiv |1_{\omega_{-3}}\rangle_A|1_{\omega_4}\rangle_B$, $11 \equiv |1_{\omega_{-3}}\rangle_A|1_{\omega_5}\rangle_B$.

we thus violate the q_{MU} bound by 9.8 standard deviations, providing a clear witness of entanglement in our system.

Moreover, BME allows us to estimate the full density matrix from just the four measurements in Fig. 3.6, with any missing tomographic information reflected naturally in the retrieved uncertainty [93, 94]. As mentioned earlier, the operations above—$\mathbb{1}$ and H followed by frequency-bin detection—are equivalent to measurements in the Pauli Z and X bases, respectively. Using this information, BME produces the density matrix $\hat{\rho}$ in Fig. 3.6: the mean values of the real and imaginary components are plotted in panels (a) and (b); their associated standard deviations in (c) and (d) (see Appendix C.2 for model details). The power of Bayesian inference is particularly evident in the error. It is extremely low for the real elements, due to our complete coverage of the Z and X bases, yet much larger on several of the imaginary

components, as expected given the absence of results in the Pauli Y basis. Since physical requirements do bound this error, we can still strongly bound our estimate of the fidelity compared to the the ideal state $|\Psi^+\rangle \propto |1_{\omega_{-4}}\rangle_A|1_{\omega_5}\rangle_B + |1_{\omega_{-3}}\rangle_A|1_{\omega_4}\rangle_B$. Specifically, the Bayesian estimate is $\mathcal{F}_W = \langle\Psi^+|\hat{\rho}|\Psi^+\rangle = 0.92 \pm 0.01$. This result provides positive corroboration of our frequency-bin control, and is fairly conservative, given that: (i) dark counts are not removed, and thus can degrade the state; and (ii) we intentionally lump any imperfections in our system onto the state itself, so that impurities in either the input state or quantum frequency processor will contribute to lower $\mathcal{F}_W$. Such findings demonstrate the utility of our quantum frequency processor for manipulating joint quantum systems coherently and independently, preserving a state's built-in entanglement in the process—an essential functionality in frequency-bin qubit control.

3.6 Outlook

In this chapter, we significantly expand the paradigm introduced earlier, showing high-contrast interference of fully quantum frequency states. By making use of our gate's unique tunability, we demonstrate frequency-bin HOM interference with record-high visibility. And by incorporating such tunability with our method's parallelizability, we synthesize independent quantum frequency gates in the same device, realizing the first high-fidelity flip of spectral correlations on two entangled photons. These results demonstrate multiple functionalities in parallel in a single platform, representing a huge step forward for the frequency-multiplexed quantum internet.

Moving forward, a key question should be addressed to further bolster QFP's role in frequency-bin QIP platform is how *diverse* a set of parallel quantum gates can be, given they all share the same EO modulations? For the demonstration discussed in this chapter, the gate is smoothly tuned from $\mathbb{1}$ to H ($\mathcal{R} = 0 \rightarrow 0.5$) simply by changing the phase shift on the pulse shaper, but unfortunately, it cannot go all the way to a Pauli-X ($\mathcal{R} = 1$) gate. Indeed, additional simulations show that to realize a

X operation, the temporal modulation patterns applied to the EOMs are significantly different than those of $\mathbb{1}$ and H. We then ask, is it possible to implement all the desired quantum gates with the same RF drives but different spectral modulation patterns, and how many components in the QFP we will need in this case? This criterion, of course, is not a necessary condition for universal frequency-bin QIP, but it could be extremely valuable for efficient resource provisioning. For example, a single QFP can perform distinct quantum operations to multiple frequency-bin qubits in separate subbands and fully capitalize its inherent parallelizability, rather than introducing multiple QFPs and realizing the task with a divide-and-conquer strategy.

From a complementary point of view, we can also ask the same question but with a different premise: suppose the pulse shapers in the QFP are fixed, can we achieve all the quantum operations of interest, such as X, Y, Z, and H gates, simply by adjusting the EO modulations[4]? The potential of real-time updating the QFPs will be beneficial for networking-centric quantum applications, in which the user(s) holds a QFP to measure the flying qubits in different bases (in a QKD system), perform distinct operations with respect to the bit strings to transmit (in a superdense coding system), or simply route/process a quantum package upon receiving a header of classical pulse (in a quantum/classical coexistence network).

[4]The reason we assume pulse shapers are fixed is due to technical limitation. For a pulse shaper based on liquid-crystal modulators or realized with a bank of on-chip thermo-optic phase shifters, the update speed is in the scale of ms, which is significantly slower than that of EOMs (inverse of the electro-optic bandwidth).

4. A CONTROLLED-NOT GATE FOR FREQUENCY-BIN QUBITS

4.1 Background

Two-qubit *entangling* gate, which operates on one qubit conditioned on the state of the other, is a necessary component for constructing any arbitrary quantum operation to fulfill universal QIP [19]. While photonics excels for single-qubit gates, the inherent difficulty in realizing photon-photon interactions has made the two-qubit gate a persistent obstacle in photonic QIP. In the absence of a sufficient nonlinearity, such gates can still be achieved via quantum interference, ancilla photons, feed-forward operation, and single-photon detection. While two-qubit gates succeed only probabilistically in this paradigm, linear-optical quantum computation (LOQC) [23] is in principle scalable with polynomial auxiliary resource requirements and has laid the foundation for many subsequent advances in photonic QIP [88, 97–102]. Previously, we have discussed the experimental implementation of spectral LOQC [12]—a universal QIP scheme tailored to frequency-bin qubits which makes use of EOMs and PSs (or namely, the QFP). Single-qubit operations with near-unit fidelity have been reported in Chapter 2, but a two-photon frequency-bin gate has heretofore proven elusive and yet to be realized on any other platform. Nevertheless, the basic mechanism of two-photon gates relies on high-fidelity quantum interference, and the demonstration of frequency-bin HOM interference with near-unity visibility (cf. Chapter 3.4) indicates strong potential of realizing such gates with the QFP.

Theoretically, Lukens *et al* [12] have previously discovered EOM/PS configurations capable of realizing ancilla-based (heralded) two-qubit gates in spectral LOQC [12], where the success probability and ancilla photon requirements can match the best

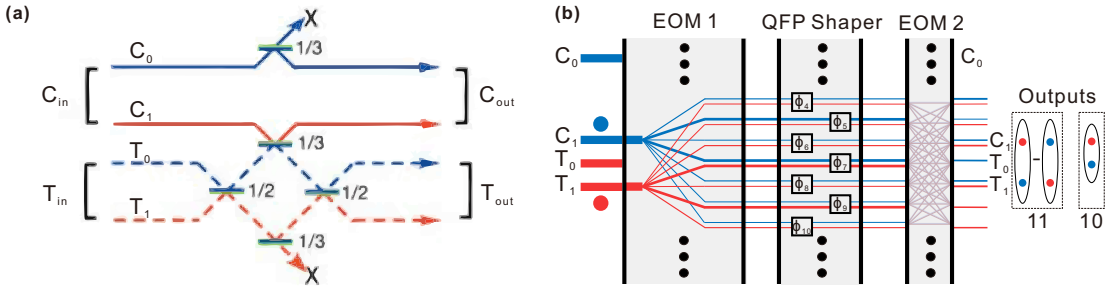

Fig. 4.1. **Coincidence-basis controlled-not gate.** (a) A photonic CNOT gate, firstly realized in the spatial-encoded platform [101], utilizes a sequences of beamsplitters (with 1/2 and 1/3 reflectivity) to induce non-classical interference between two photons owing to path indistinguishability. (b) Conceptual frequency-bin interference in the QFP, for the case of input state $|11\rangle$. Quantum interference suppresses the result $|11\rangle$ at the output, leaving only state $|10\rangle$ in the coincidence basis. While the general interference phenomena can apply to both platforms, the basic manipulations are significantly different.

known in any linear-optical platform[1]. Yet if one relaxes the gate requirements slightly, by conditioning on the presence of a photon in the desired qubit modes, it is well-known in standard LOQC that one can engineer a two-qubit gate with no ancillas and success probability $\mathcal{P}_W = 1/9$ [98, 100]. Assuming a quantum nondemolition measurement is unavailable, such gates are destructive (succeeding only when both information-carrying photons are themselves detected, also known as *coincidence-basis*). Yet they require only two-fold coincidences for characterization, making them excellent choices for experimental studies of basic quantum computing functionalities.

Before we move on to the details of the gate design, we believe it will be instructive to have a short discussion regarding the basic concept behind this coincidence-basis controlled-NOT (CNOT) gate—the first two-photon gate we choose to implement on our platform—which flips the state of the target qubit if the control qubit is in state $|1\rangle$. In Fig. 4.1, we provide a side-by-side comparison between the original path-

[1]A 4EOM/4PS QFP is capable of realizing a controlled-Z (CZ) gate with the best-known success probability of $\mathcal{P}_W = 2/27$ [12]. A CZ gate flips the sign of the target qubit when both inputs are $|1\rangle$.

encoded version and our version of CNOT gate. Fig. 4.1(a) describes one of the first experimental realizations of photonic CNOT gate [101], which consists of three spatial beamsplitters with 1/3-reflectivity, sandwiched by two balanced beamsplitters. This design was motivated by the fact that a CNOT operation can be decomposed as: $U_{CNOT} = (1 \otimes H)U_{CZ}(1 \otimes H)$, where H is equivalent to a 50/50 beamsplitter, and as derived in Ref. [98, 100], the quantum interference at the partial beamsplitter can give rise to a π phase shift for the $|11\rangle$ state (i.e., CZ operation) when postselecting on two-photon coincidence events. After the gate transformation, the input photon pair can end up in the same output spatial mode or dumped out of the circuit, but only when a coincidence event is registered between a control and target output mode then we know the gate succeeds.

On the other hand, Fig. 4.1(b) provides a conceptual example of the interference underpinning the frequency-bin CNOT, where the rails denote particular frequency bins and the lines trace out probability amplitudes of single photons initially in bins C_1 and T_1 (logical 1 for both control and target qubits); blue follows the control, red the target, and the thickness is proportional to the squared amplitude. Each EOM serves as a multimode interferometer mixing all bins simultaneously; in this particular example, the phases applied by the QFP shaper produce destructive interference of the two amplitudes yielding the output $|C_1T_1\rangle$, leaving only the possibility $|C_1T_0\rangle$ in the coincidence basis (the characteristic CNOT bit flip). This picture highlights that, while the general interference phenomena remain the same between path and frequency encoding, the basic manipulations are significantly different: standard beamsplitters interface two input modes with two outputs, while EOMs couple, in principle, infinitely many. Such a lack of direct correspondence between frequency-bin and path primitives is the reason for our use of numerical optimization of the full transformation, rather than constructing and combining individual frequency-bin beamsplitters.

4.2 Experimental Setup and Gate Design

To explore two-qubit gates with a QFP, we follow the optimization approach in Chapter 1.3, numerically finding phase patterns for an EOM/PS sequence which maximize success $\mathcal{P}_W$ constrained to fidelity $\mathcal{F}_W \geq 0.9999$, while restricting our simulations to sinewave-only EO modulation. We find that a 3EOM/2PS QFP can realize a frequency-bin CNOT at the optimal success probability of $\mathcal{P}_W = 1/9$, while a smaller 2EOM/1PS circuit can do so with reduced success: $\mathcal{P}_W = 0.0445$. Due to equipment availability and system complexity, we elect to implement this simpler 2EOM/1PS CNOT in the experiments below. See Appendix A for the specific EOM/PS modulation patterns, and numerically obtained mode and state transformation matrices.

Fig. 4.2 provides a schematic of the setup. The gate itself comprises the central EOM/PS/EOM sequence, and the frequency bins for encoding are defined according to $\omega_n = \omega_0 + n\Delta\omega$, where $\omega_0 = 2\pi \times 193.45$ THz and $\Delta\omega = 2\pi \times 25$ GHz,

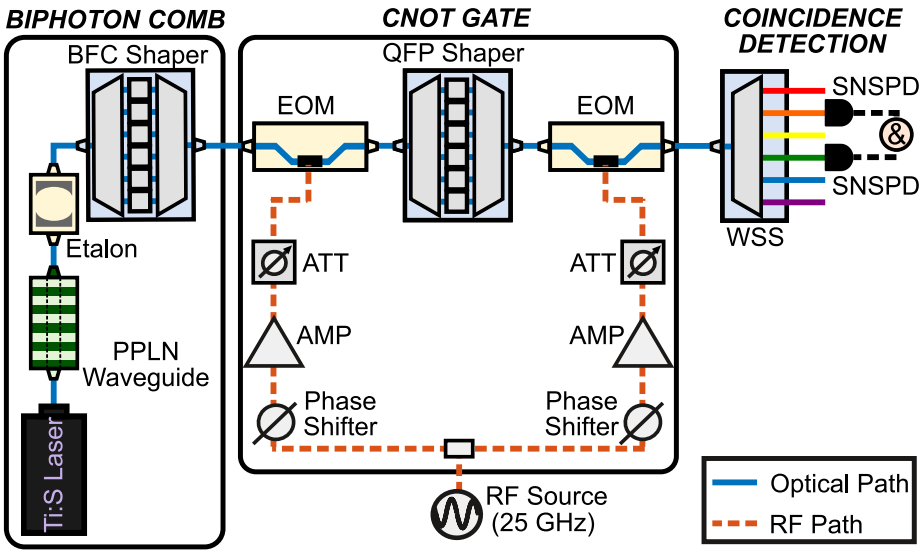

Fig. 4.2. **Realization of frequency-bin CNOT with the QFP.** The experimental arrangement is very similar to that described in Figure 3.3, with only a slight difference in the management of the Ti:S laser and the PPLN waveguide for preparing all four computational-basis states as the input. See text for more details.

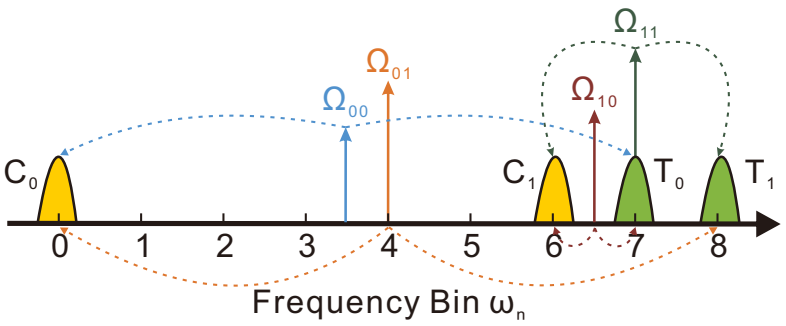

Fig. 4.3. **Mode definitions for control and target qubits.** The labels $\{\Omega_{00}, \Omega_{01}, \Omega_{10}, \Omega_{11}\}$ mark the pump frequency values (divided by two) needed to produce each of the computational basis states. The encoding frequency bins are defined according to $\omega_n = \omega_0 + n\Delta\omega$, where $\omega_0 = 2\pi \times 193.45$ THz and $\Delta\omega = 2\pi \times 25$ GHz.

corresponding to the standard ITU grid and facilitating low-crosstalk, line-by-line shaping by our 10 GHz resolution pulse shapers. The specific bins for encoding follow in Fig. 4.3, where $\{C_0, C_1\}$ and $\{T_0, T_1\}$ denote logical $|0\rangle$ and $|1\rangle$ for the control and target, respectively. Compared to single-qubit gates, where only the spacing between the two computational bins matters, two-qubit gates provide a much richer parameter space; namely, the placement of the four computational modes relative to each other can have a profound impact on the EOM/PS complexity needed to realize a specific operation. In general, we are guided by the intuition to spectrally isolate control mode 0 (C_0) while packing control mode 1 (C_1) close to both target modes[2]. This ensures a photon in mode C_0 leaves the target unchanged, while bin C_1 is close to both target bins, able to be coupled to T_0 and T_1 with equal strength. We have performed a thorough—though non-exhaustive—search over these possible mode placement combinations in each round of optimization. In our simulation, we have found more than one arrangement leading to similar gate performance, and thus we choose to work with the solution which demands smallest EO modulation depth to facilitate experimental implementation.

[2]This intuition comes from the design in the path-encoded CNOT. In Fig. 4.1(a), the control mode 0 (C_0) is spatially isolated and never interacts with other modes.

4.3 Coherent State Measurement

Since this gate is based on a linear-optical network, we can again estimate its performance using coherent-state-based characterization (See Appendix B), i.e., probing it with an EO comb and measuring the output spectrum for different input frequency superpositions. This technique allows us to estimate the mode transformation matrix V, which controls how input mode operators $\hat{a}_n$ at each frequency ω_n transform to the output operators $\hat{b}_n$: $\hat{b}_n = \sum_{n'} V_{nn'}\hat{a}_{n'}$. The mode matrix V, averaged over five independent measurements and projected onto the four computational modes, is shown in Fig. 4.4(a). We utilize phasor notation to represent the complex elements $V_{nn'}$; the filled color reflects the amplitude on a logarithmic scale, normalized to the maximum value in the matrix (0.499), and the arrow marks out the phase.

From this matrix V, we can compute the equivalent two-photon *state* transformation matrix[3] W

$$W_{C_rT_s\leftarrow C_kT_l} = V_{C_rC_k}V_{T_sT_l} + V_{C_rT_l}V_{T_sC_k};\ \{k,l,r,s\} \in \{0,1\}. \tag{4.1}$$

This equation perfectly captures the concept behind the coincidence-basis two-qubit gate: An operation succeeds only when one photon is detected at the control qubit (C_r) and another at the target qubit (T_s). The summation of the two terms describes the quantum interference between two possible pathways given by the mode transformation, i.e., ($C_k \rightarrow C_r, T_l \rightarrow T_s$) and ($T_l \rightarrow C_r, C_k \rightarrow T_s$). The inferred state transformation W is plotted for the coincidence basis in Fig. 4.4(b) and also normalized to its peak magnitude of 0.222.

Because this estimate predicts all four of the large elements of W to be in-phase, the corresponding inferred fidelity is $\mathcal{F}_{\mathrm{W,inf}} = 0.995 \pm 0.001$; the success probability is $\mathcal{P}_{\mathrm{W,inf}} = 0.0460 \pm 0.0005$. Both values are with respect to the ideal CNOT and in good agreement with theory. We emphasize that, unlike single-qubit gates which act on photons independently, two-qubit entangling gates rely on quantum interference

[3]In the case of two-photon gates, the mode transformation V is **no longer** equivalent to the state transformation W, which can only be *inferred* from V obtained in the coherent-state-based characterization method.

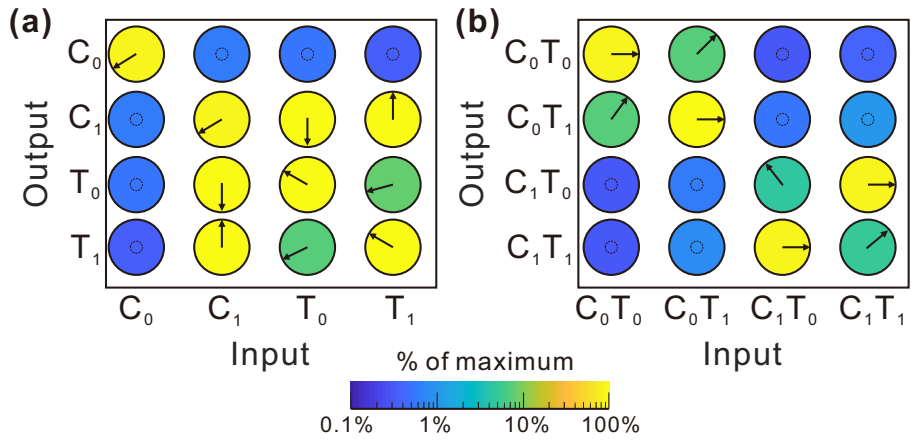

Fig. 4.4. **Coherent-state-based gate characterization.** (a) Experimentally obtained complex mode transformation V. (b) Inferred two-photon transformation W obtained from permanents of 2×2 submatrices of V. For both cases, we use phasor notation to represent the complex elements, with filled color signifying the amplitude (normalized by the matrix's maximum value, and shown on a logarithmic scale), and the arrow depicting the phase. Dotted circles denote phases we could not retrieve due to weak amplitudes.

effects that are inherently absent with high-flux laser fields. Thus this inferred fidelity is only an indirect estimate, based on extrapolating measured one-photon interference results to the two-photon case. Nevertheless, it provides strong initial evidence for the phase coherence and proper operation of our gate.

4.4 Quantum Measurement in the Computational Basis

To test our gate with truly quantum states, we prepare a biphoton frequency comb (BFC) by pumping a PPLN waveguide with a continuous-wave Ti:sapphire laser, followed by filtering the broadband biphotons with a 25 GHz spaced etalon (see Fig. 4.2 and discussion in Chapter 3 for more details). By translating the pump frequency to four different values (as shown in Fig. 4.3) and selecting the desired modes using the BFC shaper, we can prepare all inputs from the two-qubit computational basis: $|C_0T_0\rangle = |1_{\omega_0}1_{\omega_7}\rangle$, $|C_0T_1\rangle = |1_{\omega_0}1_{\omega_8}\rangle$, $|C_1T_0\rangle = |1_{\omega_6}1_{\omega_7}\rangle$, and $|C_1T_1\rangle = |1_{\omega_6}1_{\omega_8}\rangle$. To

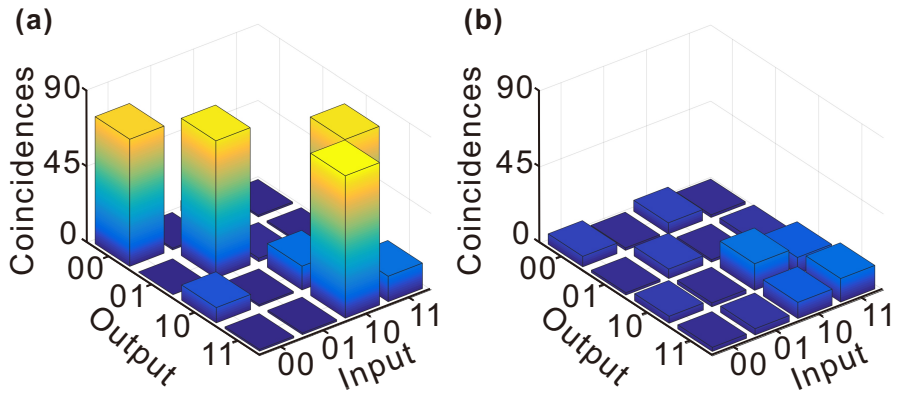

Fig. 4.5. **Measurement in the computational basis.** (a) Experimentally measured coincidences over 600 s for all input/output logical-basis state combinations, showing a characteristic CNOT bit flip. (b) Estimated number of accidentals computed from the product of single detector counts.

ensure the photon flux remains constant across the four inputs, we tune the PPLN temperature to align the peak of the phase-matching spectrum with the pump frequency. After the gate, the output photons are frequency-demultiplexed: we send control photon bins to detector A and target photon bins to detector B.

Fig. 4.5(a) shows the measured coincidences for all 16 input/output mode combinations, integrated over 600 s for each point. The results indicate our gate performs largely as designed—the quantum state holds with an input photon in C_0, while a photon in C_1 flips the target qubit. In Fig. 4.5(b) we plot the accidentals as determined by the product of the singles counts and our timing resolution [103, 104]. The nonuniform distribution of accidentals stems from the fact that the singles counts vary significantly across input/output state combinations. Indeed, this is a natural feature of coincidence-basis gates: they are designed to discard cases when one of the qubit spaces is empty or doubly occupied, so that photon detection rates in a specific mode can change without impacting the designed operation.

4.5 Gate Reconstruction via Bayesian Machine Learning

Such information-bearing features in the accidentals suggest that incorporating knowledge from single-detector events—as well as the coincidences—can add significant value for quantifying the performance of our gate in the presence of noise. To utilize all of our experimental data in a consistent fashion, we make use of Bayesian machine learning techniques to implement a numerical parameter inference approach built on Bayesian mean estimation (BME) [105]. In the context of quantum state retrieval, BME is a powerful method which returns uncertainties on any quantity directly and makes efficient use of all available information, in the sense that the confidence in any estimate naturally reflects the amount of data gathered [93]. BME models for photon pairs including single-detector events have been developed as well, permitting extraction of the quantum pathway efficiencies in conjunction with estimates of the input density matrix [94]. In our BME model here, not only do we account for noise effects, but we can also retrieve meaningful estimates of the full complex matrix V, even though we only prepare and measure states in the computational basis. This represents an entirely new capability in two-photon gate analysis, for previously such truth-table measurements [as in Fig. 4.5(a)] have only been used to establish *magnitudes* in the matrix transformation, with superposition states required to assess the phase [101].

The general model for extracting information using BME can be outlined as follows: We first define a set of unknown parameters of interest called β, usually represented by density matrix, gate transformation, pair generation rate, etc. Experimentally, we collect data $\mathcal{D}$, such as single counts and multiphoton coincidence events, from a number of trials in different experimental configurations. We can construct a multinomial likelihood function $P(\mathcal{D}|\beta)$, which mathematically describes what the probability of observing the data set $\mathcal{D}$ is, given the parameters β. After setting up a prior distribution $P(\beta)$—general knowledge about the parameters before making the inference—we compute the multivariate posterior probability distribution $P(\beta|\mathcal{D})$

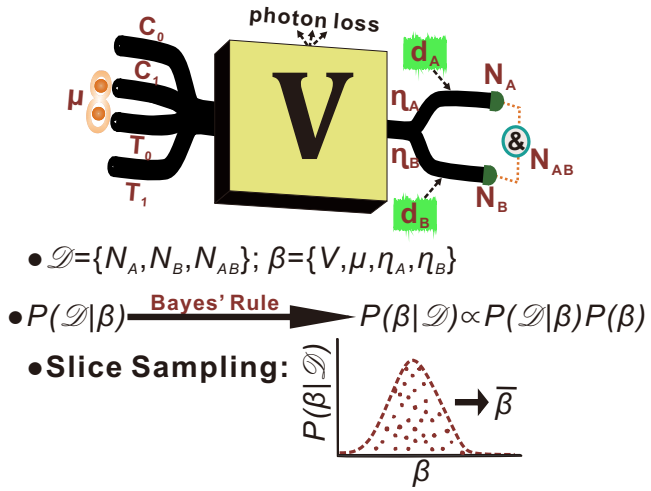

Fig. 4.6. **Outline of our Bayesian machine learning approach.** For every input/output combination, we can construct a multinomial likelihood function $P(\mathcal{D}|\beta)$ to connect the unknown parameters β with the experimental data $\mathcal{D}$, including single counts N_A and N_B and coincidences N_{AB}. Using Bayes' rule and slice sampling method, we can retrieve samples $\bar{\beta}$ from the posterior distribution, which can faithfully represent the parameters of interest.

using Bayes' rule: $P(\beta|\mathcal{D}) \propto P(\mathcal{D}|\beta)\,P(\beta)$, which represents complete knowledge of the parameters given the observed data. Finally, numerical sampling algorithm, such as Metropolis-Hastings and slice sampling [106], can be employed to extract a sufficient amount of samples from the posterior distribution. Suppose the samples can faithfully represent the distribution of interest, we can compute the means and error bars of the parameters from those samples.

Fig. 4.6 depicts the outline of our BME model, while more details can be found in Appendix C.3. The unknown parameters (β) to retrieve include: the mode transformation matrix V, the pair generation probability μ, and the total system efficiencies η_A and η_B preceding detection at the control and target photon detectors, respectively. Obtained from independent measurements, and thus taken as fixed and known, are the dark count probabilities d_A and d_B. All probabilities $\{\mu, d_A, d_B\}$ are specified for one resolving time τ ($\sim$1.5 ns). For the input photon state $|C_k T_l\rangle$ ($k, l \in \{0, 1\}$)

with detectors A and B set to respond to output modes C_r and T_s ($r, s \in \{0, 1\}$), respectively, the probability of a coincidence between detectors A and B is

$$p_{AB} = \mu\eta_A\eta_B \left|V_{C_rC_k}V_{T_sT_l} + V_{C_rT_l}V_{T_sC_k}\right|^2 + 2p_Ap_B. \tag{4.2}$$

Here p_A and p_B are the marginal probabilities for clicks on A or B, irrespective of clicks on the other, during a given time τ. This formula thus contains both a correlated term (from photons of the same pair; cf. Eq. 4.1) and an accidental term. The latter, equal to $2p_Ap_B$ [103, 104], represents the chance of simultaneous clicks in which at least one detector registers a dark count, or the photons come from different pairs (see Appendix C.3 for details).

The marginal probabilities p_A and p_B can be found by summing the contributions from each possible number of photons N being present in the monitored mode, sketched formally as, e.g., $p_A = \sum_N P(\text{click}|N \text{ photons})P(N \text{ photons})$. Writing out each term for $N = 0, 1, 2$, and simplifying, we ultimately arrive at the probabilities for a click on either detector within a time τ (see Appendix C.3):

$$\begin{aligned} p_A &= \mu\eta_A\left(\left|V_{C_rC_k}\right|^2 + \left|V_{C_rT_l}\right|^2\right) + d_A \\ p_B &= \mu\eta_B\left(\left|V_{T_sC_k}\right|^2 + \left|V_{T_sT_l}\right|^2\right) + d_B, \end{aligned} \tag{4.3}$$

valid under the assumptions $\mu, \eta_A, \eta_B, d_A, d_B \ll 1$—satisfied in our experiment. Crucially, the singles probabilities [Eq. (4.3)] depend only on the **moduli** of the V-matrix elements, whereas the coincidences also depend on the **relative phase** [via the permanent term in Eq. (4.2)]. It is this complementary dependence which underpins our ability to extract the full complex matrix from experimental data.

Specifically, for a single preparation/measurement configuration we possess three numbers as data: clicks on A (N_A), clicks on B (N_B), and coincidences (N_{AB}). This gives us the multinomial likelihood for this specific input/output configuration ($|C_kT_l\rangle \to |C_rT_s\rangle$):

$$\begin{aligned} P\left(\mathcal{D}^{C_rT_s}_{C_kT_l}|\beta\right) &= (p_A - p_{AB})^{N_A - N_{AB}}(p_B - p_{AB})^{N_B - N_{AB}} \\ &\quad \times p_{AB}^{N_{AB}}(1 - p_A - p_B + p_{AB})^{M - N_A - N_B + N_{AB}}, \end{aligned} \tag{4.4}$$

where $\mathcal{D}_{C_k T_l}^{C_r T_s} = \{N_A, N_B, N_{AB}\}$ contains all data values for the specific configuration. We have also reexpressed the events to make them mutually exclusive: click on A only, happening $N_A - N_{AB}$ times; click on B only, occurring $N_B - N_{AB}$ times; coincidence between A and B (N_{AB} times); and no clicks (all remaining frames). M equals the total number of τ frames considered in one counting period ($\sim 4 \times 10^{11}$ in our tests). The complete likelihood comprises 16 factors in the manner of Eq. (4.4) for all combinations of inputs and outputs.

After setting up the prior distributions for all parameters (See Appendix C.3), we have the posterior probability distribution from Bayes' rule. However, practically speaking, computing integrals or, equivalently, sampling from this many-parameter multimodal distribution is a formidable challenge. It is here that the techniques of Markov chain Monte Carlo (MCMC) sampling offer a solution, which—with minimal input—enable Bayesian machine learning of complex models. In our case, we employ slice sampling, an MCMC algorithm designed to produce a sequence of samples whose stationary distribution converges to the posterior [106].

Using the predicted matrix V as an initial guess for the slice sampler, a procedure which we found important to speed up convergence given the large search space of 28 independent variables, we ultimately converge to the Bayesian fidelity estimate $\mathcal{F}_{\mathrm{W,BME}} = 0.91 \pm 0.01$. Our truly quantum measurement does not reach the >0.99 classically inferred $\mathcal{F}_{\mathrm{W,inf}}$, which is a consequence of the relatively few coincidence counts (<100 in all cases) and additional noise from residual light. Nevertheless, the low uncertainty on $\mathcal{F}_{\mathrm{W,BME}}$ indicates high confidence in our BME model, especially in light of its ability to retrieve the full complex fidelity with computational basis measurements. To see how $\mathcal{F}_{\mathrm{W,BME}}$ translates into output state probabilities in the coincidence basis, we plot the Bayesian-estimated pathway probabilities in Fig. 4.7, where the four outcomes for each input state are normalized to sum to unity. The average probability for obtaining the correct output is 0.92 ± 0.01, computed by taking the mean of the four peaks in Fig. 4.7.

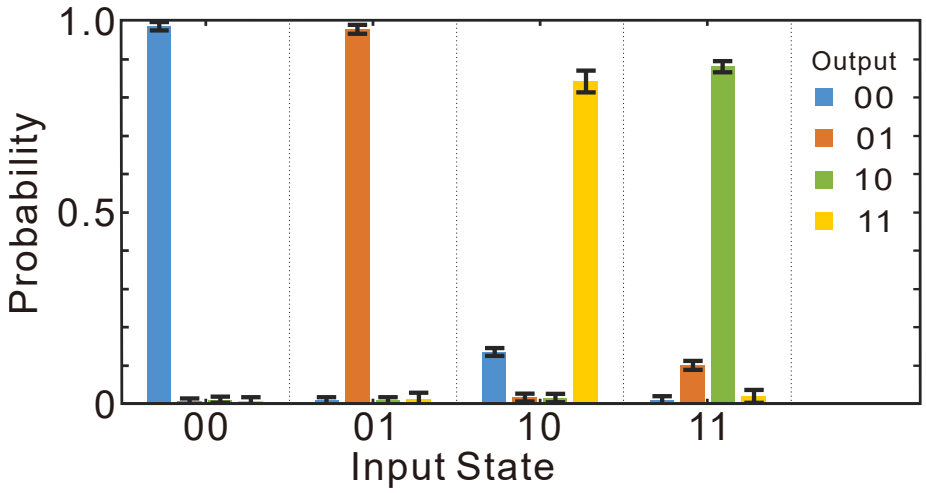

Fig. 4.7. **Retrieval of probabilities for the computational-basis operation via BME.** Utilizing a parameter inference approach based on Bayesian machine learning, we are able to reconstruct the full gate transformation from measurements in the logical basis alone. Translating the BME results into output state probabilities, we calculate an average probability of 0.92 ± 0.01 for obtaining the correct output, computed by taking the mean of the four peaks in the figure.

4.6 Outlook

In this chapter, we have realized an entangling gate in frequency-bin encoding. We confirm high-fidelity CNOT operation with two forms of characterization: coherent-state-based reconstruction and photon pair measurements in the computational basis. Both the classically inferred fidelity and Bayesian estimate suggest high performance in our system. As the sole realization of a two-photon entangling gate in frequency, our gate significantly expands the potential of single-spatial-mode, fiber-optic-based QIP. More generally, our Bayesian characterization approach provides further evidence of the potential of machine learning in analyzing quantum systems, particularly for extracting information within measurements which traditional methods overlook.

Hitherto, a crucial point missing in this chapter is to demonstrate this CNOT gate is truly **entangling**, i.e., producing an entangled two-qubit state from a separable state at the input. Such experiment usually involves with, for example, preparing the

input control qubit in a superposition state $|C_0\rangle \pm |C_1\rangle$ and the target in either $|T_0\rangle$ or $|T_1\rangle$, performing a full quantum state tomography on the output states for density matrix reconstruction, and finally calculating the fidelity between the retrieved state and the ideal output state (i.e., one of the Bell states) [101]. More interestingly, a CNOT circuit, due to its reversibility, can disentangle the entangled states. Introducing an extra Hadamard gate to the control output, one can deterministically discriminate any of the four input Bell states (i.e., Bell-state analyzer) from the other by reading the output coincidence pattern [98]. The capability of processing arbitrary two-qubit states with this CNOT gate will also be useful implementing photonic QIP algorithms such as the variational quantum eigensolver [107] and Shor factoring [108]. Moreover, the standard procedure for gate characterization such as quantum process tomography (QST) [109–111], which is designed to recover a quantum operation treating the system as a black box, also requires preparation of many linearly independent input states for measurement.

To prepare the input states beyond just the computational basis, extra components such as EOMs and shapers are required to fulfill this objective. For example, one could precede the CNOT operation with additional Hadamard operations on one or both input photons (cf. Chapter 3). Yet cascading additional elements at the moment is limited by technical loss; we predict that we could not at present obtain coincidences above the accidental level with the additional equipment required. On the other hand, an alternative solution is to absorb this technical loss *before* the photon generation, i.e., by engineering the pump. The two-photon state generated in our system is still limited to a certain form[4], mostly due to the usage of single-tone, continuous-wave pump. It is worth investigating whether arbitrary two-qubit states, or at least, all four Bell states can be prepared given the pump now contains multiple comblines and the etalon (shown in Fig. 4.2) is replaced by a pulse shaper for full amplitude and phase filtering.

[4]For example, our BFC state is usually in the form of $|1_{\omega_i} 1_{\omega_{-i}}\rangle \pm |1_{\omega_j} 1_{\omega_{-j}}\rangle$, which resembles two of the Bell states.

5. FULLY ARBITRARY CONTROL OF FREQUENCY-BIN QUBITS

5.1 Background

Drawing on arguments from LOQC [23], our QFP approach has been shown scalable in principle, and a collection of gates comprising a universal set have been realized experimentally [20, 21, 24, 25], as discussed in the past few chapters. Such scaling arguments prove crucial in establishing ultimate feasibility, yet leave many smaller—though highly practical—questions unanswered. For example, the fully arbitrary rotation of a single qubit represents a fundamental capability for any two-level system, yet neither a Solovay–Kitaev construction [112] in terms of basic gates, nor general resource bounds, reveals the optimal construction of general two-mode unitaries, particularly when subject to practical resource constraints.

In this chapter, we answer this important question through theoretical analysis and experimental verification of arbitrary single-qubit gates in frequency-bin encoding. We have established optimal designs for arbitrary single-qubit unitaries on frequency-bin qubits, for multiple quantum frequency processor setups subject to realistic constraints on modulation and elements. Our numerical simulations obtain three-element QFP configurations capable of any unitary operation with fidelity $\mathcal{F}_W \geq 0.9999$ utilizing single-tone modulation only; by either adding a second harmonic or cascading an additional pulse shaper/modulator pair, such operations achieve success probabilities $\mathcal{P}_W > 0.95$ or $\mathcal{P}_W > 0.999$, respectively. We reinforce these findings experimentally, synthesizing frequency-bin unitaries with performance in close agreement with theory. Finally, we highlight their use at the single-photon level in the rotation of a fixed input to arbitrary points on the Bloch sphere, obtaining output state fidelities $\mathcal{F}_\rho > 0.98$ with respect to the ideal. Our results represent the first full tomography

of arbitrarily rotated frequency-bin qubit states, establishing resource guidelines for future systems and providing tools for fundamental applications in communications and coherent control.

5.2 Problem Formulation

In discrete-variable frequency-bin encoding, a frequency-bin qubit can be described by annihilation (creation) operators $\hat{a}_0$ ($\hat{a}_0^\dagger$) and $\hat{a}_1$ ($\hat{a}_1^\dagger$) centered at frequency ω_0 and ω_1, respectively. A pure qubit state may be expressed as $|\psi\rangle = (c_0\hat{a}_0^\dagger + c_1\hat{a}_1^\dagger)\,|\text{vac}\rangle$, where $|\text{vac}\rangle$ is the vacuum state and $|c_0|^2 + |c_1|^2 = 1$. Logical basis states follow as $|n\rangle = \hat{a}_n^\dagger\,|\text{vac}\rangle$ ($n \in \{0, 1\}$). Any 2×2 unitary operating on these modes can be parameterized as [113]

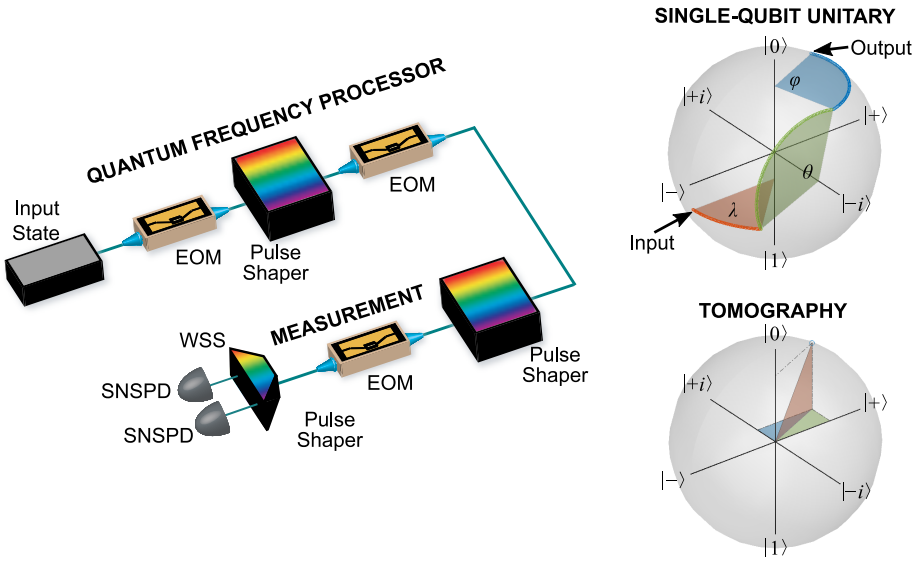

Fig. 5.1. **Experimental setup for arbitrary frequency-qubit operations and state measurement.** Insets show an example unitary rotation for an input state $|\psi\rangle = 0.6\,|0\rangle - 0.8\,|1\rangle$ and $(\theta, \varphi, \lambda) = (0.7\pi, 0.55\pi, 0.25\pi)$, with tomography represented in terms of projections onto each axis. Here $|\pm\rangle \propto |0\rangle \pm |1\rangle$ and $|\pm i\rangle \propto |0\rangle \pm i\,|1\rangle$.

$$U(\theta,\varphi,\lambda)=\begin{pmatrix}\cos\frac{\theta}{2} & -e^{i\lambda}\sin\frac{\theta}{2}\\ e^{i\varphi}\sin\frac{\theta}{2} & e^{i(\varphi+\lambda)}\cos\frac{\theta}{2}\end{pmatrix}, \tag{5.1}$$

where $\theta\in[0,\pi]$, $\varphi\in[0,2\pi)$, and $\lambda\in[0,2\pi)$. Further intuition can be gained by factorizing into the product $U(\theta,\varphi,\lambda)=D(\varphi)R(\theta)D(\lambda)$, where $D(\cdot)$ represents a diagonal unitary imparting a phase shift to bin 1 (R_z-rotation) and $R(\cdot)$ a mixing between both bins (R_y-rotation). Considering this as taking the inputs $\hat{a}_0$ and $\hat{a}_1$ to outputs $\hat{b}_0$ and $\hat{b}_1$, this implies that the output state coefficients, $|\phi\rangle=(d_0\hat{b}_0^\dagger+d_1\hat{b}_1^\dagger)\,|\text{vac}\rangle$, satisfy $\left(\begin{smallmatrix}d_0\\ d_1\end{smallmatrix}\right)=U\left(\begin{smallmatrix}c_0\\ c_1\end{smallmatrix}\right)$. An example unitary rotation is shown in the upper right inset of Fig. 5.1: starting at $|\psi\rangle=0.6\,|0\rangle+0.8\,|1\rangle$, the state rotates through $\lambda=0.25\pi$ around the z-axis, then $\theta=0.7\pi$ around y, and finally $\varphi=0.55\pi$ around z to end up at $|\phi\rangle=0.5547\,|0\rangle+0.8320\,e^{-i0.7130\pi}\,|1\rangle$.

This mathematical formulation applies generally to any qubit system. The nuances of the QFP approach appear, though, when describing (i) the bins ω_0 and ω_1 as embedded within a comb spaced at $\Delta\omega$ ($\omega_n=\omega_0+n\Delta\omega; n\in\mathbb{Z}$) and (ii) the transformation on all modes $\hat{b}_m=\sum_n V_{mn}\hat{a}_n$ as characterized by an alternating series of electro-optic phase modulators (EOMs) driven with $\frac{2\pi}{\Delta\omega}$-periodic waveforms and pulse shapers applying arbitrary phases to each bin. As modeled, V is unitary over the entire countably infinite collection of bins, though the 2×2 submatrix in the computational space—call this $W=\left(\begin{smallmatrix}V_{00} & V_{01}\\ V_{10} & V_{11}\end{smallmatrix}\right)$—may or may not prove unitary, due to coupling into adjacent bins. While an apparent disadvantage of the QFP in this case (particularly when compared to the isolated modes of alternative frequency-bin approaches [33, 35, 36, 91, 114, 115]), this natural coupling between many bins facilitates multiphoton interference between all underlying modes as required for LOQC. Moreover, by cascading additional pulse shapers and EOMs and employing more complex modulation patterns, such adjacent-bin coupling can be fully compensated for, to realize smaller-dimensional gates with unity efficiency [12, 61].

Within this overall framework, considerable progress has been made on a subset of $U(\theta,\varphi,\lambda)$: the phase-only gate $U(0,\varphi,\lambda)$ and the Hadamard $H=U(\frac{\pi}{2},0,\pi)$,

with the former requiring only a single pulse shaper, and the latter realizable with an EOM/pulse shaper/EOM QFP [21, 24] (cf. Chapter 2.2). These considerations engender optimism for experimental realization of arbitrary U, yet they do not answer the practical questions of explicit construction, nor elucidate the procedures involved in reconfiguring a given QFP for all possible unitaries.

5.3 Numerical Simulations

Here we focus on pure-sinewave EO modulation (either one or two tones), and QFPs with three or five elements. Limitation to odd-numbered QFPs follows from previous observations that adding a pulse shaper on either side of a QFP improves neither fidelity nor success probability. In fact, these remarks can be made rigorous in the present case of a single-qubit operation. Suppose that a particular QFP configuration realizes the gate $W = gU(\theta, 0, 0)$ (unitary up to an overall constant). Then, as derived in Appendix D, the same QFP can actualize the gate $gU(\theta, \varphi, \lambda)$ by delaying the RF signals applied to the first (last) EOM by $-\frac{\lambda}{\Delta\omega}$ ($\frac{\varphi}{\Delta\omega}$) and adding linear phases $k\lambda$ ($k\varphi$) to the first (last) pulse shaper [the sum $k(\lambda + \varphi)$ in the case of a single pulse shaper in a three-element QFP], with k the frequency-bin index.

This finding implies that, for the purpose of establishing performance under system constraints, one need only concentrate on $U(\theta, 0, 0)$ numerically. We emphasize that, while similar, these phase degeneracies prove fundamentally more significant than those resulting from the freedom to set a phase reference. As argued in Ref. [81] and invoked below in our own characterization procedure, the prerogative to define the "in-phase" condition across modes at the input and output planes of an optical multiport simplifies the process of extracting amplitudes and phases of the individual transformation elements V_{mn}. However, such phase reference flexibility does not imply the physical equivalence of operations that differ by this reference. For example, if one defines the reference so that the QFP realizes $U(\theta, 0, 0)$, modifying the transformation to $U(\theta, \varphi, \lambda)$ produces measurable differences in the output state, impacting

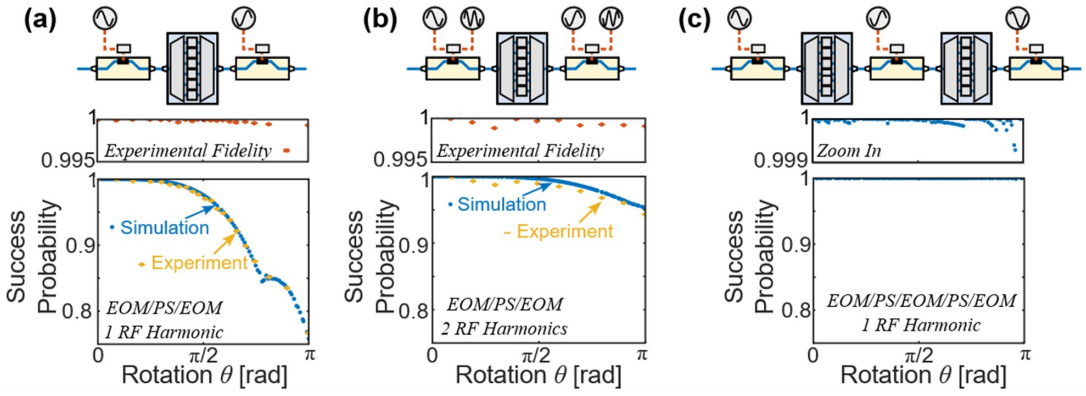

Fig. 5.2. **QFP configurations.** Optimized success probability of single-qubit gate $U(\theta, 0, 0)$ for different QFP configurations. (a) Three-element QFP, single-tone modulation. (b) Three-element QFP, two-tone modulation. (c) Five-element QFP, single-tone modulation.

any subsequent operations downstream. Accordingly, the relationship between phase and EOM delay discussed here is not just the establishment of a reference: it gives a means to realize a (φ, λ) combination for *any* reference definition.

To benchmark the performance of single-qubit gates synthesized on the QFP, we randomly generate 150 samples of $\theta \in [0, \pi]$ [corresponding to 150 different unitaries $U(\theta, 0, 0)$], and numerically find the solutions $U(\theta, 0, 0)$ for three different scenarios (see Fig. 5.2): three-element QFP driven by (a) one or (b) two RF tones and (c) five-element QFP driven by single tone. Case (a) is the baseline QFP which we have utilized in previous chapters, while cases (b) and (c) describe the two most immediate upgrades; (b) has been explored in a limited context for a frequency-bin qutrit operation in Chapter 2, while (c) has so far required too many resources for implementation. Yet all three are realizable with standard, commercially available components—no specialized RF or optical equipment required.

We then assess the performance of W with respect to the desired U according to gate success $\mathcal{P}_W = \mathrm{Tr}(W^\dagger W)/2$ and gate fidelity $\mathcal{F}_W = |\,\mathrm{Tr}(W^\dagger U)|^2/(4\,\mathcal{P}_W)$ metrics, where $\mathcal{P}_W$ describes the probability of a photon remaining in the computational space,

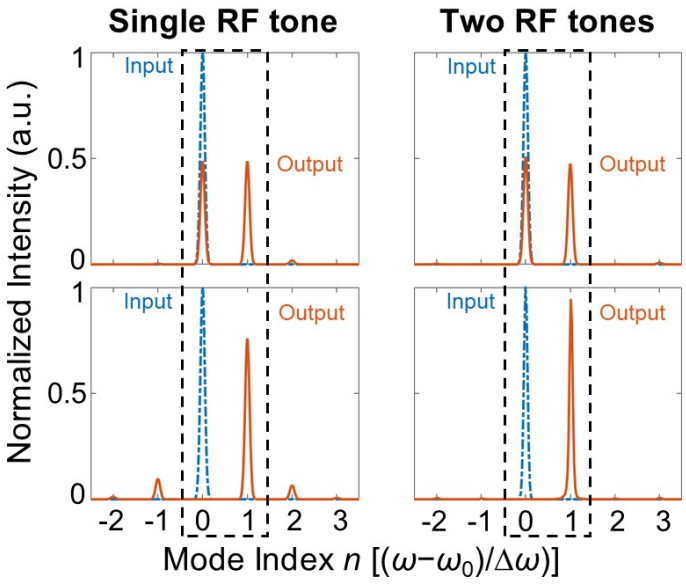

Fig. 5.3. **Mode-transformation spectra.** Experimentally obtained spectra for Hadamard (top row) and Pauli-X (second row) operation with three-element QFP driven by single and two RF tones. The dashed box represents the computational space.

and $\mathcal{F}_W$ defines the quality of the operation [62]. Figure 5.2 plots the simulation results. $\mathcal{P}_W$ shows a strong dependence on θ, suggesting that those unitaries with small θ are easier to realize. This matches our intuition as the identity and phase-only gates ($\theta = 0$) can be realized without any EOM, while gates like Pauli X and Y ($\theta = \pi$) require proper engineering of the mixing process such that the photon can be completely hopped to the opposite bin. Additionally, the results indicate that gate performance can be significantly boosted with increased complexity in the controls, by introducing either an additional RF harmonic [Fig. 5.2(b), $\mathcal{P}_W > 0.95$] or extra components [Fig. 5.2(c), $\mathcal{P}_W > 0.999$]. Here, we experimentally focus on the setup in Fig. 5.2(a) and (b) due to equipment availability—i.e., lack of EOMs and pulse shapers for (c).

5.4 Gate Characterization

Figure 5.1 provides a schematic of the experimental setup. A high-frequency RF oscillator generates 25-GHz sinusoidal voltages to drive both EOMs, where their amplitudes and delays are set with manual phase shifters and attenuators. [1] Meanwhile, the optimized spectral phase pattern is programmed onto the QFP shaper. Experimentally, we select 21 out of the 150 previous solutions from Fig. 5.2(a). To investigate whether each gate performs as anticipated, we utilize a coherent-state–based characterization approach [21,81] by probing our QFP with an electro-optic frequency comb and measuring the output spectrum for different input superpositions. As a result, we are able to reconstruct the mode-transformation matrix W and compute the experimental $\mathcal{F}_W$ and $\mathcal{P}_W$, as shown in Fig. 5.2(a) and (b). All measured gate fidelities are above 0.9993 (except for one, unexplained outlier), and the success probabilities track closely the theoretical prediction. Figure 5.3 presents a comparison between the single-tone and two-tone QFP performance for the Hadamad and Pauli-X operations. The success probability, i.e. the power preserved in the computational space, improves significantly with the introduction of the extra RF harmonic.

5.5 Quantum State Tomography and Bayesian Reconstruction

The previous tests confirm synthesis of arbitrary frequency-qubit operations, when viewed in terms of optical modes. Yet in the context of photonic QIP, these *mode* transformations are valuable insofar as they enable high-fidelity operations on quantum *states*. Accordingly, we explore these gates at the single-photon level, focusing specifically on their ability to convert a fixed input to an arbitrary output state. For example (see Fig. 5.1), given a well-defined qubit $|\Psi\rangle$ as the input of the QFP, we can convert it to an output state anywhere on the Bloch sphere through an unitary oper-

[1] To implement the configuration in Fig. 5.2(b), i.e., three-element QFP driven by two RF tones, please refer to Chapter 2 for more detailed discussion. The drive frequency is reduced to 20 GHz (and 40 GHz for the doubled tone) given the available RF bandwidth.

ation $U(\theta, \varphi, \lambda)$. We can then assess the quality of this manipulation by performing quantum state tomography (QST) on the output photon. [2]

For single-qubit QST, we perform three Pauli measurements (Z, X, and Y) to project the output state onto the eigenvectors $|t\rangle$ (six in total): $\{|0\rangle, |1\rangle, |\pm\rangle, |\pm i\rangle\}$. To realize these three Pauli measurements (Z, X, and Y) for QST, one needs to apply $\mathbb{1}$, H, and $HS^\dagger$ prior to computational-basis measurement, where H is the Hadamard operation and $S = \left(\begin{smallmatrix} 1 & 0 \\ 0 & i \end{smallmatrix}\right)$. Experimentally, we follow the gate operation (namely, the last EOM in the QFP) with a pulse shaper to filter out any photons outside of mode 0 and 1 such that residual scattering will not affect the operations downstream—i.e., by coupling back to the computational space and introducing measurement errors. For the H operation, we elect to use a single EOM to realize a probabilistic version of the Hadamard gate; driving this EOM with a sinusoidal RF voltage with a modulation index of 1.434 rad, we have equal power splitting between mode 0 and 1, as shown in Fig. 5.4(a). This approach inevitably scatters more photons ($\sim$40%) out of the single-qubit space than its near-deterministic counterpart using a three-element QFP [21], but can be implemented with the limited number of EOMs available in our laboratory. Figure 5.4(b) and (c) show examples of projecting $|+\rangle$ and $|-\rangle$ states to $|0\rangle$ and $|1\rangle$, respectively. The clear contrast between two output frequency modes shows that this approach, while reducing the efficiency of the tomographic process, does not sacrifice projection accuracy.

We emphasize that the RF drive applied to this EOM is synchronized with those in the QFP, and its relative timing should be properly set as well. Experimentally, we first program a Hadamard operation on the QFP and send the output photons (now in the $|+\rangle$ state) through the pulse shaper (applying zero phase to all bins) and EOM for tomography, and fine tune the delay of this electrical drive via a manual RF phase shifter while recording the photon counts in two computational modes. Once we obtain maximal (minimal) amount of photons in the frequency mode 0 (mode 1),

[2]Here our focus will be the simplest QFP configuration—three-element QFP driven by single RF tone.

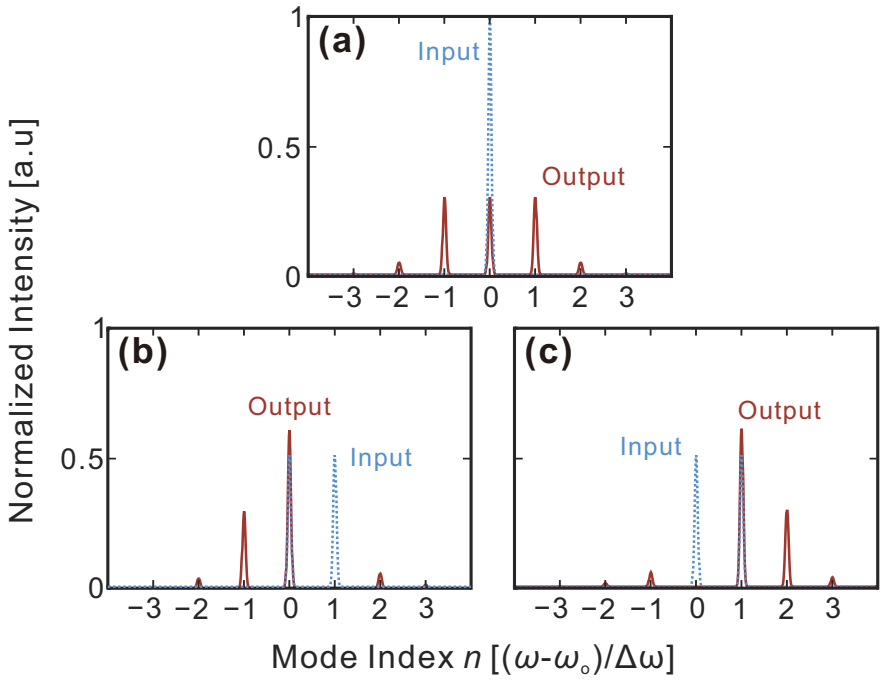

Fig. 5.4. Probabilistic Hadamard operation for QST. Example of simulated output spectra for specific inputs. (a) Pure mode 0, $|0\rangle$. (b) Mode 0 and 1 in phase, $|+\rangle \propto |0\rangle + |1\rangle$. (c) Mode 0 and 1 out of phase, $|-\rangle \propto |0\rangle - |1\rangle$. 40% of the photons are scattered outside of the computational space due to the usage of single EOM.

this EOM is aligned to perform the desired H measurement and the delay setting is fixed throughout the rest of the experiment. Then, by applying a phase of $-\frac{\pi}{2}$ to frequency bin 1 on the measurement pulse shaper, we can realize the necessary $S^\dagger$ operation for $|\pm i\rangle$ measurement as well.

Finally, for computational-basis projection, we demultiplex the photons by color with a wavelength-selective switch (WSS), and records the counts in $|0\rangle$ and $|1\rangle$ with superconducting nanowire detectors (SNSPDs). For each measurement setting, we record the counts over 1 s, then subtract the average detector dark counts and obtain a final dataset $\mathcal{D} = \{N_0, N_1, N_+, N_-, N_{+i}, N_{-i}\}$ with all outcomes for subsequent tomographic analyses. For reconstruction, we employ Bayesian mean estimation [93], an advanced tomographic technique which avoids unjustifiably low-rank estimates and

furnishes natural error bars. We parameterize the density matrix $\hat{\rho}(\mathbf{x})$ and sample a posterior distribution $\pi(\mathbf{x}) \propto L_{\mathcal{D}}(\mathbf{x})\pi_0(\mathbf{x})$ with multinomial likelihood

$$L_{\mathcal{D}}(\mathbf{x}) = p_0^{N_0} p_1^{N_1} p_+^{N_+} p_-^{N_-} p_{+i}^{N_{+i}} p_{-i}^{N_{-i}}, \tag{5.2}$$

where $p_t \equiv \langle t|\hat{\rho}(\mathbf{x})|t\rangle$ is the probability of measuring the state $|t\rangle$ given the proposed state $\hat{\rho}(\mathbf{x})$. We adopt the parametrization, prior distribution $\pi_0(\mathbf{x})$, and sampling procedure recently proposed in Ref. [116], obtaining $R = 1024$ density matrix samples $\hat{\rho}_r$ for each tomographic dataset, from which we estimate the fidelity according to the mean and standard deviation of the values of the individual samples ($\mathcal{F}_r = \langle\phi|\hat{\rho}_r|\phi\rangle$).

5.5.1 Arbitrary State Rotation

Following the QFP with a set of projective measurements, we reconstruct its density matrix ($\hat{\rho}$) through QST and compute the state fidelity with respect to the ideal output state $|\phi\rangle$ via $\mathcal{F}_\rho = \langle\phi|\hat{\rho}|\phi\rangle$. [3] We prepare a single-photon-level source by attenuating a continuous-wave laser at frequency ω_0 to $\sim 10^6$ counts/s (1/10 of the detector saturation level) prior to the QFP. Since neither the QFP operation nor QST involve multiphoton interference, the results of a weak coherent state are fully equivalent to those of true single photons at the same average flux. To show that we can bring this input state, $|0\rangle = \hat{a}_0^\dagger |\text{vac}\rangle$, at the north pole of the Bloch sphere, to any arbitrary state within the whole sphere, we choose 11 values of $\theta \in [0, \pi]$ and assign a few different φ to each, amounting to a total of 41 gates to implement. The ideal output state is $|\phi\rangle = \cos\frac{\theta}{2}|0\rangle + e^{i\varphi}\sin\frac{\theta}{2}|1\rangle$.

Figure 5.5 depicts the QST results. We map the ideal output states and the retrieved Bayesian samples onto the Bloch sphere [Fig. 5.5(a)]. Three of the transformations are highlighted in the zoomed-in inset, where the Bayesian samples follow the ideal states closely. This suggests strong agreement between the design and experimental implementation, confirmed by Bayesian mean state fidelities above 98% across all gates [Fig. 5.5(b)].

[3] Note the change in definition from the Hilbert–Schmidt fidelity $\mathcal{F}_W$ used for gate characterization.

5.5.2 Tunable Beamsplitter Design

In addition to a randomly chosen set of single-qubit rotations, we can also explore coherent quantum state control across a specified trajectory. Previously, we found a set of analytical solutions for tunable frequency beamsplitters [24] (cf. Chapter 3.2),

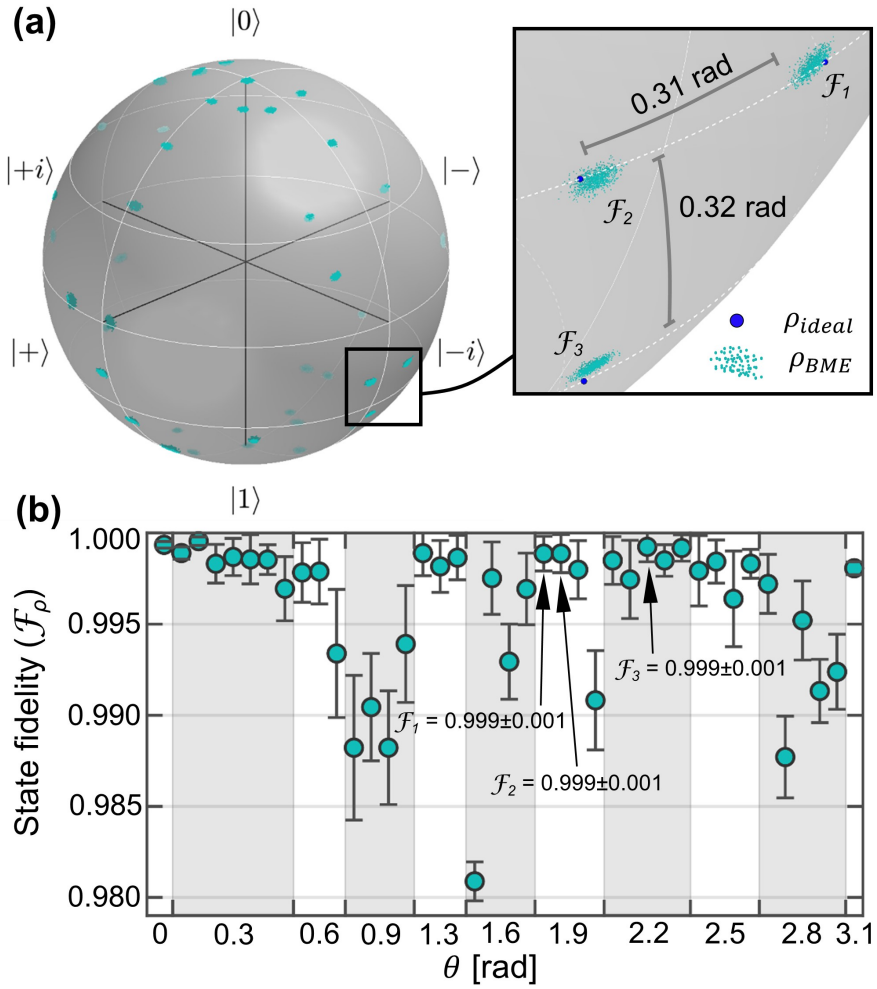

Fig. 5.5. **Arbitrary single-qubit rotations on the QFP.** (a) Retrieved Bayesian samples plotted on the Bloch sphere (green dots) following 41 different transformations $U(\theta, \varphi, 0)$. Three examples are highlighted in the inset, where blue dots mark the corresponding ideal states. (b) Associated state fidelities, grouped by θ value, with each data point corresponding to a randomly chosen φ. The mean and standard deviation are computed from 1024 Bayesian samples.

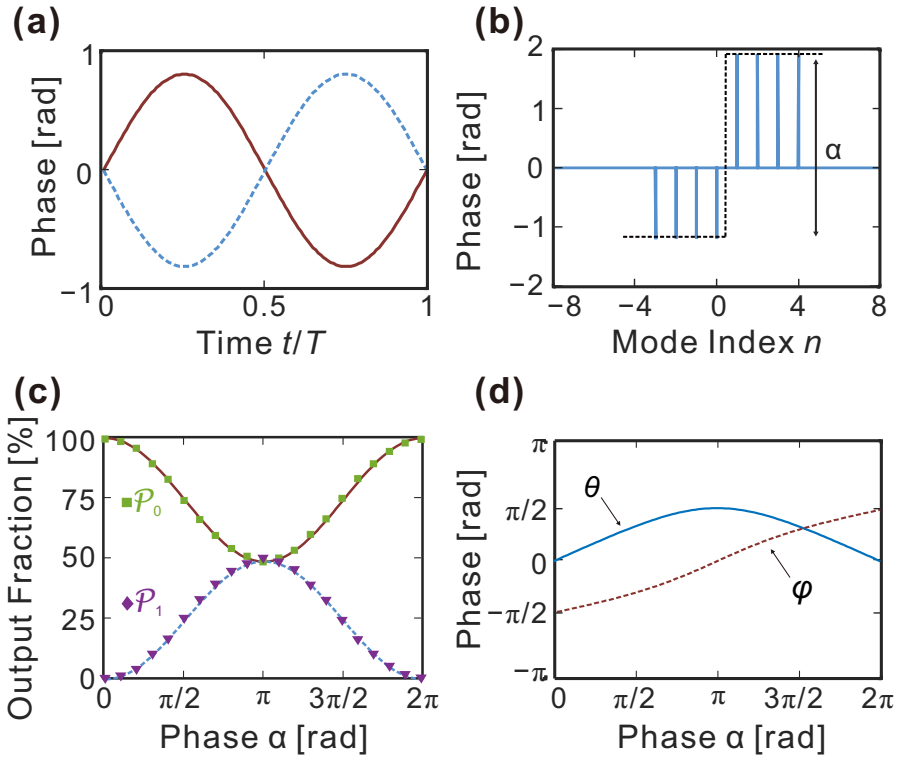

Fig. 5.6. **Tunable beamsplitter design.** (a) Temporal phase modulation applied to the first EOM (solid red) and second EOM (dotted blue). (b) Spectral phase pattern applied by the pulse shaper, where modes 0 and 1 denote the computational space. (c) Theoretical beamsplitter transmissivity $\mathcal{T}$ (solid red) and reflectivity $\mathcal{R}$ (dotted blue). Markers denote the values measured with single-photon-level input. (d) Extracted parameters for the corresponding unitary $U(\theta, \varphi, 0)$.

where the reflectivity can be set anywhere between 0 and 0.5 simply by changing the depth of the phase shift α imparted by the QFP shaper between frequency bins 0 and 1 (while both EOMs remain fixed). We revisit such design but with only a slight modification in the EO modulation—previously, the modulation index was set at 0.8169 rad, which can numerically realize a fidelity $\mathcal{F}_W = 0.9999$ and success probability $\mathcal{P}_W = 0.9760$ for the Hadamard operation (when α is π). Here we adjust the the modulation index to 0.829 rad, and the theoretical fidelity for the Hadamard gate is boosted to $\mathcal{F}_W = 0.9999999$ after a small reduction in the success probability, $\mathcal{P}_W = 0.9746$. Figure 5.6(a-b) depicts the specific configuration for this design.

Figure 5.6(c) plots the theoretical $\mathcal{T}$ (solid red) and $\mathcal{R}$ (dotted blue) with respect to α. On top of the two curves we also mark the (normalized) photon counts obtained in the Pauli Z measurement with single-photon-level input at frequency mode 0, which matches the theoretical prediction well. Finally, to visualize the trajectory of such a beamsplitting operation on the Bloch sphere, we map the output state $V_{00}(\alpha)\,|0\rangle + V_{10}(\alpha)\,|1\rangle$ to the form of $\cos\frac{\theta}{2}\,|0\rangle + e^{i\varphi}\sin\frac{\theta}{2}\,|1\rangle$ from the equivalent unitary $U(\theta,\varphi,0)$ and compute the corresponding θ and φ [shown in Fig. 5.6(d)]. The maximum θ goes to $\pi/2$ (i.e., from north pole to equator) since our tunable beamsplitter design achieves maximum reflectivity of 50%, rather than a full frequency hop. As for φ, it follows a continuous path from $-\pi/2$ to $\pi/2$, which explains the counterclockwise trajectory shown in Fig. 5.7(a). Note that for better visualization, we wrap the parameter φ within $-\pi$ and π (instead of 0 to 2π as in the main text).

For full QST, we sample 21 evenly spaced $\alpha \in [0, 2\pi]$ for implementation, and again repeat the QST measurement for the same state input $|0\rangle$. Figure 5.7 depicts the experimental results. As we increase α, the output state is moved from the north pole ($|0\rangle$) to the equator ($|+\rangle = H\,|0\rangle$), and then back to the north pole ($|0\rangle$), following a counterclockwise trajectory on the Bloch sphere (dashed line in Fig. 5.7). Again all measurements are in excellent agreement with theory ($\mathcal{F}_\rho > 0.98$).

5.6 Outlook

In addition to addressing fundamental questions in frequency-bin quantum state control, the findings described here appear particularly relevant in the applications of quantum communications and networking. Indeed, one of the inherent benefits of frequency-bin encoding is its compatibility with fiber-optic communications: the QFP paradigm already leverages commercial telecom components (EOMs and pulse shapers), and frequency-bin operations can be extensively parallelized according to the principles of wavelength-division multiplexing (WDM). This synergy has enabled several recent quantum networking demonstrations invoking WDM for distributing

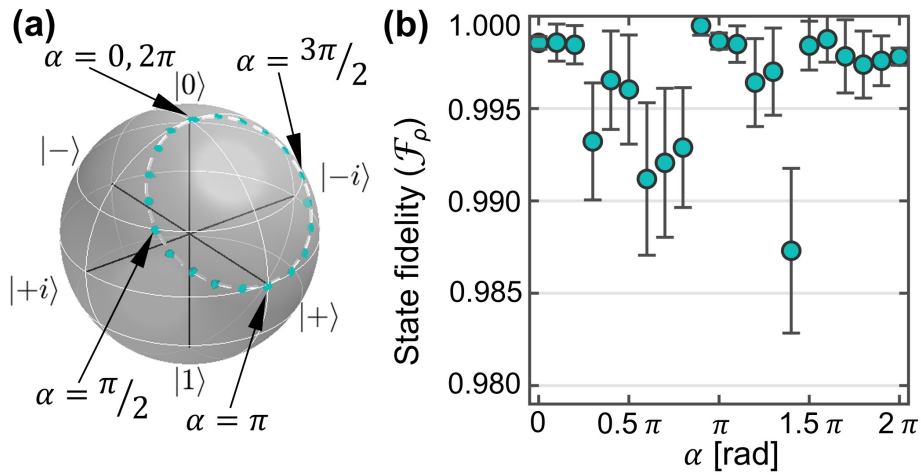

Fig. 5.7. **Tunable beamsplitter.** (a) Ideal output state trajectory (dashed line) and retrieved Bayesian samples (green dots) plotted on the Bloch sphere. (b) Bayesian state fidelities as function of pulse shaper phase α.

0

entanglement in other degrees of freedom [117–120]; the QFP approach moves even further by exploiting frequency bins for encoding quantum information as well, and the fully arbitrary unitaries realized here should make feasible an array of quantum networking protocols with frequency bins. Whereas the previously shown Hadamard ($\theta = \frac{\pi}{2}$) [21, 24] would be sufficient (along with the identity) for basis measurements in quantum key distribution [90], it is only through these more general unitaries that the full range of qubit quantum information protocols can be realized. For example, both superdense coding [27] and quantum teleportation [28] require single-qubit gates including a full 180° rotation ($\theta = \pi$), and the standard CHSH Bell inequality [121] relies on measurements preceded by unitaries with $\theta \in \{0, \frac{\pi}{4}, \frac{\pi}{2}, \frac{3\pi}{4}\}$.

Moreover, while we have focused specifically on the fundamental two-level qubit here, one of the salient features of the frequency degree of freedom is its natural compatibility with high-dimensional qudit ($d > 2$) encoding [53, 54, 86, 122]. Importantly, the same design procedure adopted here can be applied for the construction of arbitrary qudit operations as well. As initial examples, we have numerically found $2d + 1$

EOMs and pulse shapers sufficient for high-dimensional frequency hopping (up to $d = 5$) using single-tone RF modulation [61]; we have also found $d - 1$ RF harmonics capable of realizing d-dimensional discrete Fourier transformations (up to $d = 10$) on a single three-element QFP. Combined with general scaling arguments [12], these results highlight that arbitrary high-dimensional gates can be realized in an efficient fashion. The main limitations moving to higher dimensions, then, are technical in nature—namely, the complexity of RF drive waveforms and the number of pulse shapers and EOMs available.

On the characterization side, our focus on QST of an arbitrarily rotated state corroborates the gate performance estimated from classical measurements. On the other hand, quantum process tomography (QPT) would be required for a complete quantum-mechanical description of the gate itself [110]. This procedure relies on preparation of multiple input states (four in the case of a single-qubit operation), followed by QST of each output after the QFP, which would necessitate additional components beyond those available to us. Given our understanding of the physical mechanisms involved in the QFP, we do not expect fundamentally new insights from QPT. Nevertheless, realization of complete QPT—perhaps leveraging Bayesian techniques for experimental simplifications—would prove valuable in future work, as a means to further validate performance.

6. APPLICATIONS IN FREQUENCY-BIN QIP

6.1 Frequency-Domain Bell State Analyzer

6.1.1 Motivation

Within the overall landscape of quantum science and technology, the development of quantum networks is critical for applications such as blind quantum computing, connected quantum sensors, and distributed quantum computing [123]. Quantum networks can interconnect quantum information between physically separated matter qubits via entanglement swapping operations (ESO) on traveling photons[1]. First, each quantum system locally entangles their matter qubits with single photons and launches them into the fiber network. Next, photons from different quantum systems are brought together and processed by an apparatus called a "Bell-state analyzer"

[1]Here we omit the discussion of the simplest type of ESO designed for DLCZ protocols [124], where one utilizes a single spatial beamsplitter to mix the optical paths from two atomic ensembles such that the detection of a *single* photon erases all "which-way" information and projects the matter qubits onto an entangled state (i.e., coherent superposition of a single atomic excitation in one or the other ensemble).

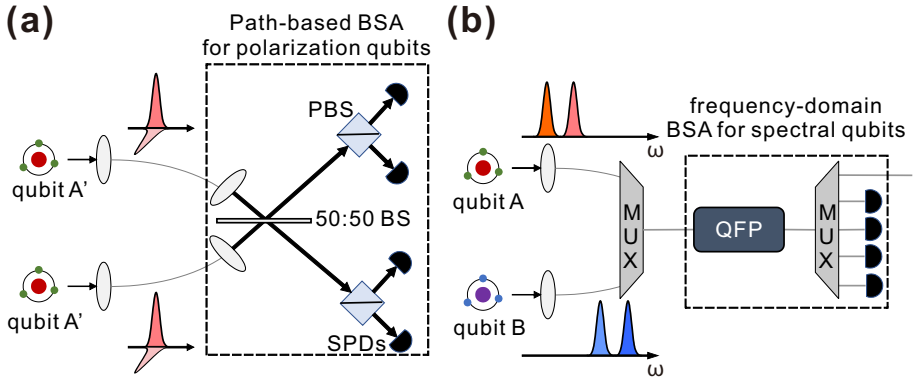

Fig. 6.1. **Photonic BSA.** Bell state analyzers based on (a) spatial and (b) frequency beamsplitters.

(BSA). When the measurement is successful, the BSA erases the information carried by the photonic qubits and projects the distant matter qubits, though they never interacted, onto an entangled state.

In the simplest conception of a Bell-state analyzer, two photons, each entangled with separate qubits (either matter-based or photonic), are mixed with a set of linear optics—usually a combination of spatial/polarizing beamsplitters. Quantum interference between two-photon outcomes leads to one of many detection events. A subset of the possible detection outcomes, usually signified by twofold coincident detections, herald projection of the undetected qubits onto an entangled state. This is a probabilistic process with a maximum efficiency of 50% when using linear optics and vacuum ancillas [125], i.e., only two out of four Bell states can be discriminated unambiguously. An optical module capable of carrying out such a measurement is often referred to as a two-state Bell state analyzer (2-BSA) and was first realized for polarization-encoded photons [126]. Figure 6.1(a) provides the concept of such an example, where orthogonal modes (H with H and V with V) are mixed in parallel at a $50:50$ spatial beamsplitter. Two of the Bell states, $|\Psi^{\pm}\rangle$, can be distinguished from their distinct coincidence patterns, while the $|\Phi^{\pm}\rangle$ family results in two photons bunching in the same detectors[2].

However, the quality of generated entanglement depends critically on the spectral indistinguishability of photons participating in the joint measurement. This is an inherent challenge in the case of frequency-bin encoding, as well as a practical challenge in networks with heterogeneous nodes, homogeneous nodes but in the presence of location-dependent energy shift, or those that rely explicitly on spectral multiplexing of quantum channels. To erase the frequency-distinguishable information between two photons, one can use time-resolved detection with fast detectors to increase the fidelity of remote entanglement, which reduces the entanglement rate owing to the need for temporal postselection [129]. Time-resolved detection in combination with

[2]Interestingly, this is not the *only* possible apparatus for two-state Bell-state measurement. Experimental demonstrations using extra polarization rotators [127, 128] can distinguish different Bell states, albeit still with 50% success probability (in this case, $|\Psi^{+}\rangle$ and $|\Phi^{+}\rangle$).

active feed-forward [130, 131] has been used to mitigate this issue, but fidelities are still lower than what one would obtain with spectrally indistinguishable photons.

6.1.2 Methods and Results

Among all the possible scenarios for spectrally distinguishable photons, we consider the case where two input photons, photon A and B, have quantum information directly encoded in four disparate, equispaced frequency modes $\{A_0, A_1\}$ and $\{B_0, B_1\}$, respectively [3]. To implement the frequency-domain BSA, we draw an analogy from the 2-BSA design for the polarization qubit in Fig. 6.1(a)—i.e., mixing modes A_0 with B_0 and A_1 with B_1 with frequency beamsplitters [H_1 and H_2 in Fig. 6.2(b)], followed by spectrally-resolved coincidence measurements.

Hitherto we have extensively explored and focused on frequency beamsplitters operating on "nearest-neighbor" modes on a three-element QFP with ultrahigh fidelity

[3]Other scenarios will be discussed in the following section.

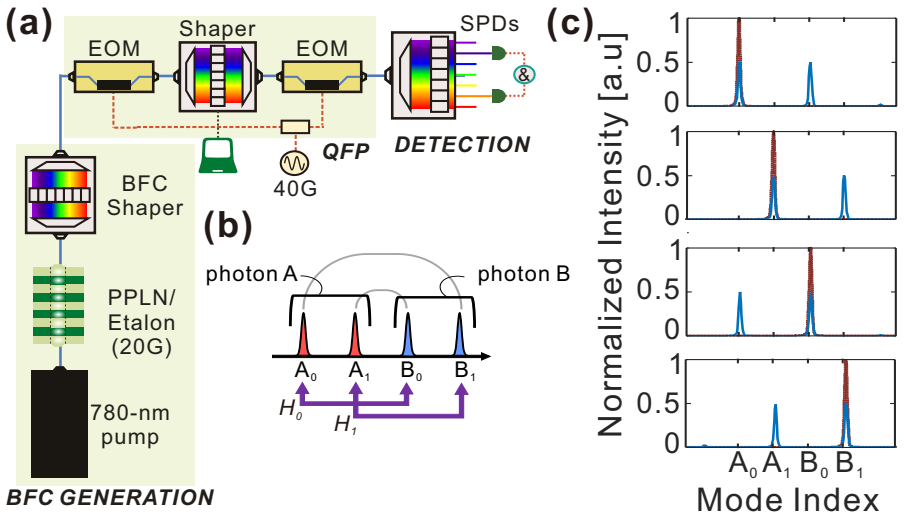

Fig. 6.2. **Frequency-domain BSA.** (a) Experimental configuration. (b) Concept illustration of interleaved Hadamard transformations (H_0 and H_1) for frequency-domain BSA. (c) Experimentally measured output spectra for single-frequency input at mode $\{A_0, A_1, B_0, B_1\}$.

[cf. Chapters 2 and 3], in which the microwave drive frequency equals the fundamental mode spacing ($\Delta\omega$). Setting the modulation frequency to an integer multiple $N\Delta\omega$ ($N = 2$ in this case), we can produce interleaved, parallel frequency beamsplitters for modes now spaced N modes apart, all while avoiding crosstalk with interior modes. This effectively creates two independent QFPs operating on separate "supergrids"! Figure 6.2(c) depicts the mode transformation spectra implemented in such a scenario. Finally, as with the spatial analog, only the $|\Psi^{\pm}\rangle \propto |1_{A_0}\rangle|1_{B_1}\rangle \pm |1_{A_1}\rangle|1_{B_0}\rangle$ states can be identified without ambiguity. Here we validate this functionality by demonstrating that each of these states gives rise to a unique coincidence pattern.

Figure 6.2(a) shows our experimental setup. Time-frequency–entangled photons are generated by pumping a periodically poled lithium niobate ridge waveguide (PPLN) with a continuous-wave laser at 780 nm. We use an etalon and pulse shaper (BFC shaper) to select four energy-correlated, narrowband frequency modes $\{A_0, A_1, B_0, B_1\}$, which projects the biphoton onto state $|\Psi^{\pm}\rangle$ (determined by phase applied to $|1_{A_0}\rangle|1_{B_1}\rangle$ by BFC shaper). The center-to-center separation between signal and idler is 40 GHz while the two modes in each computational space are 20 GHz apart with an intensity full-width at half-maximum of 0.8 GHz. Parallel and interleaved Hadamard transformations are implemented with the QFP driven by a 40 GHz sinusoidal voltage. The output of the QFP is frequency demultiplexed by another pulse shaper such

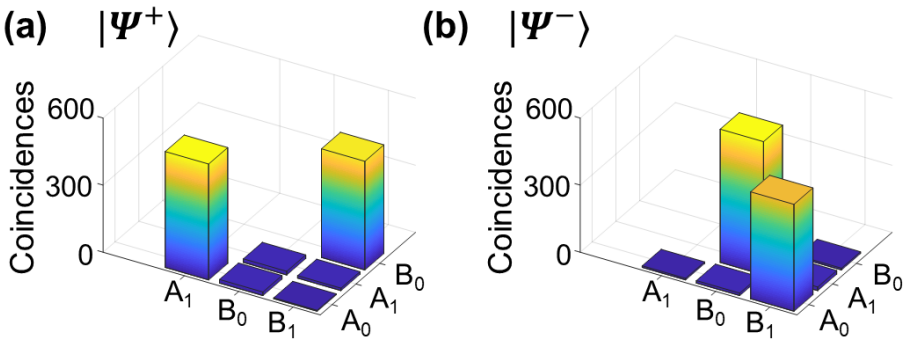

Fig. 6.3. **Two-state Bell state analyzer.** Coincidence counts registered after (a) $|\Psi^{+}\rangle$ and (b) $|\Psi^{-}\rangle$ pass through the BSA. Coincidences are integrated over a 1.15 ns window for a total of 120 seconds

that different frequency modes are routed to the two detectors (SPDs). Coincidence counts for all 6 combinations (excluding A_0A_0, A_1A_1, B_0B_0 and B_1B_1) are integrated over a 1.15 ns window for a total of 120 seconds.

Experimental results are presented in Figure 6.3. For the $|\Psi^+\rangle$ state [Fig. 6.3(a)], coincidences register between the two frequencies corresponding to the original idler modes (A_0A_1) or the two original signal modes (B_0B_1), as expected from theory [126]. On the other hand, the $|\Psi^-\rangle$ state [Fig. 6.3(b)] results in coincidences between one of the original idler modes with one of the original signal modes (A_0B_1 or A_1B_0), thereby allowing one to unambiguously distinguish $|\Psi^+\rangle$ from $|\Psi^-\rangle$. We then calculate the discrimination accuracy $F = N_c/N_T$, where N_c and N_T correspond to the sum of correct measurement results and the sum of four measurements (A_0A_1, B_0B_1, A_0B_1, and A_1B_0), respectively. For the two Bell states tested here, we achieve accuracy of 98.6% and 98.1% for $|\Psi^+\rangle$ and $|\Psi^-\rangle$, respectively, which are reported without accidental subtraction (The accuracy increases to 99.8% and 99.4% after accidental subtraction).

6.1.3 Outlook

Our demonstration represents an important step toward the long-term vision of a quantum internet that is compatible with both heterogeneous nodes and dense spectral multiplexing. While the specific 2-BSA realized here operated on frequency-bin entangled photons, the concept is easily extended to spectrally distinguishable photons encoded in other degrees of freedom (DoFs). For example, consider the case of two spectrally-distinguishable, polarization-encoded photons, a polarization-diverse version [132] of QFP can efficiently erase their frequency mismatch while preserving their polarization states. On the other hand, the reason we focus on direct frequency encoding is motivated by the many advantages of this DoF. Frequency (energy) is the most common encoding variable for matter-based qubits, as well as offers natural

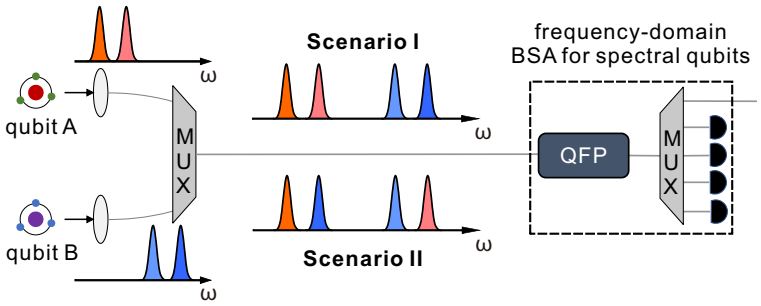

Fig. 6.4. **Frequency BSA for tunable photon frequency spacing.** Two different scenarios with mode spacing (I) smaller and (II) larger than the two-photon spacing.

stability in optical fiber, straightforward measurement with high-efficiency filters and detectors, and compatibility with wavelength-division multiplexing.

In our prototype demonstration, we address two photons populating four equispaced frequency modes. In the future, one could consider a more general version, where the four frequency modes are no longer equally spaced [cf. Fig. 6.4]. Such a scenario mimics ESO between two distinguishable quantum memories (i.e., different center frequencies) with the same Zeeman frequency splitting. Moreover, for realistic matter-qubit systems such as trapped ions or rare earth ion memories, the frequency modes can be separated by a few GHz or even less. In both cases, we anticipate needing to migrate our QFP system to an integrated platform, where the pulse shaper consists of a bank of narrow-linewidth, microring filters, capable of addressing tightly spaced frequency modes independently.

6.2 Quantifying Entanglement in Biphoton Frequency Combs

6.2.1 Motivation

In the optics community, the polarization DoF has historically been the most widely studied in the field of QIP. Tools to generate, manipulate and measure such two-level quantum states are easily accessible in the lab. Nevertheless, recent years have witnessed significantly increased attention to other discretized DoFs, such as path, orbital-angular-momentum (OAM), time-bin, and frequency-bin [122], all capable of supporting multilevel quantum information in a single particle. In comparison to standard qubit approaches, encoding quantum information on single and entangled qudits can offer crucial advantages for quantum communication and networking, such as higher information capacities, success rates and resistance to noise, to name a few.

Figure 6.5 highlights the recent progress in realizing high-dimensional QIP over the aforementioned DoFs. Given our interest in using photonic qudits for quantum communication tasks, we have paid most of our attention to the following functionalities:

- **State generation**: This includes the preparation of the entangled qudit states and certification/quantification of the amount of entanglement in the system.
- **State manipulation**: Contingent on the quantum communication protocols pursued, this can span from DFT gates (for measurement in the Fourier basis in QKD [133]) to more complex operations such as high-d cyclic shift operations (for encoding messages in superdense coding [134]).
- **Fiber compatibility**: We focus on fiber-optic network compatibility as well, due to the need for synergy between potential quantum encodings and aspects of the existing telecommunication infrastructure, such as dense wavelength division multiplexing (DWDM), FlexGrid, reconfigurable optical add-drop multiplexers (ROADMs), etc.

	Qu*D*it DOF	Path	OAM	Time-bin	Frequency-bin
Generation	**Method**	*D* nonlinear structures	1 nonlinear structure	Pulsed pump, 1 nonlinear structure	1 nonlinear structure
	Max. # of modes	16♠	100♦	32■	~ 1000 (PPLN)γ ~ 40 (MRR)δ
	Max. Entanglement	14 (certified)♠	100 (certified)♦	5 (certified)◊ 4 (full QST)Δ	4 (full QST)ζ
Manipulation	**Basic Units**	Beam splitters, Phase shifters	SLM, Phase-plates	Unbalanced interferometers, Active switching	EOMs, Pulse shapers
	Scalability	$O(D^2)$▲	O(1) - O(D)▼	$O(D^2)$	O(D) units; or O(D) RF tones
	Max. dimension	4 (Arbitrary)▲	5 (DFT, cyclic)▼	3 (cyclic)■	3 (DFT)
Fiber Transmission	**Network compatibility**	Multicore fiber	Few-mode fiber	SMF	SMF
	Longest distance	30 cm♣	1 km□	> 100 kmβ	> 40 kmζ
	Added sources of error	Phase stability between cores	Intermodal crosstalk	×	×

Fig. 6.5. **Multilevel quantum information.** A comparison of high-dimensional QIP in different photonic DoFs. List of references: ♠ [135], ▲ [136], ♣ [137], ♦ [138], ▼ [139], □ [140], ■ [141], ◊ [142], Δ [143], β [144], γ [86], δ [54], ζ [53].

A few points can be quickly summarized from Fig. 6.5. First of all, frequency-encoding undoubtedly has the best compatibility with fiber-optic networking and is more robust against certain fiber transmission impairments. Second, generation of high-dimensional frequency entangled states, usually in the form of biphoton frequency comb (BFC), can be as simple as pumping a nonlinear, resonant structure [cf. Chapter 1.1]. However, the main reason frequency encoding had received comparatively less attention than other DoFs lies in the fact that the tools required to manipulate quantum states were limited, and building high-dimensional quantum gates for photonic frequency appeared insurmountable. Indeed, this has been the main impetus behind our work in this dissertation.

Another interesting aspect to point out in Fig. 6.5 is the huge gap between the maximal number of frequency modes and the dimensionality of the entanglement characterized experimentally. Quantifying the amount of entanglement in a high-dimensional quantum system has been a long-standing question in the community, but it is more evident in the frequency DoF. For example, from the joint spectral *intensity* (JSI) measurement [cf. Fig. 3.3(b)], the number of correlated frequency modes is extremely large (∼50), but the entanglement dimensionality, which relies on the phase coherence across correlated frequency-bin pairs, remains uncharted.

Figure 6.6 provides the intuition behind this problem. With a single JSI measurement alone [equivalent to measurement in the two-photon logical basis; See

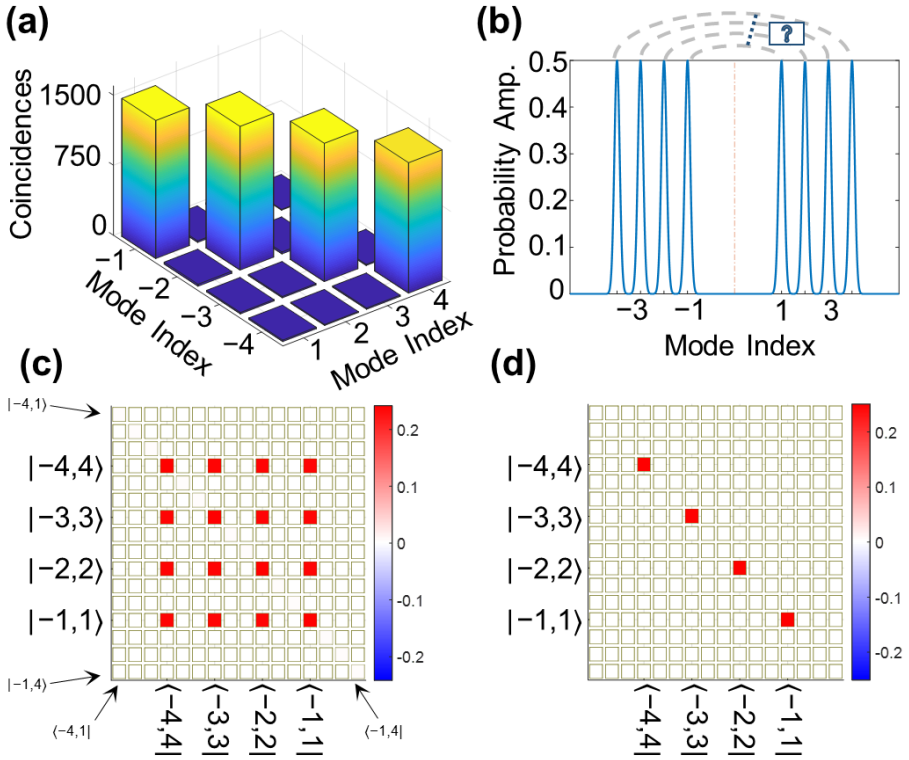

Fig. 6.6. **Phase coherence in BFCs.** (a) An example JSI measurement of the BFC source. (b) General form of BFC due to energy conservation. Density matrix plots of (c) highly entangled, pure state and (d) classically correlated, mixed state.

Fig. 6.6(a)], there is no information about the presence of inter-pair coherence [question mark in Fig. 6.6(b)]. Without extra measurements in complementary bases, it cannot be ascertained whether the BFC corresponds to a truly high-dimensional frequency-bin–entangled state, as illustrated in Fig. 6.6(c), or an incoherent mixture of comb line pairs (i.e., classically correlated state), as depicted in Fig. 6.6(d). This suggests complementary measurements are needed in order to investigate the entanglement in BFCs.

Existing literature has highlighted two major ways. First, one can directly measure the two-photon correlation in the *temporal* domain [32, 44, 86], i.e., a joint temporal intensity (JTI) measurement. Oscillations in the measured coincidence counts at a period equal to the inverse of the bin spacing signifies the existence of broadband phase coherence. However, such a scheme demands the detector resolution to be shorter than the time scales of the correlations, which is only possible for photon sources with narrow frequency-bin spacing (a few GHz), or alternatively using nonlinearity-based optically gated detection [43, 145]. The second method relies on pulse shapers and EOMs to mix the frequency bins, either probabilistically [53,54,59] or deterministically [cf. Chapter 3.5], and measure the coincidence counts with different phase settings at the input (equivalent to different measurement bases other than the computational). Nevertheless, mixing all frequency bins *equally* is a nontrivial task—a standalone EOM generates frequency sidebands with probability amplitudes following Bessel functions. On the other hand, though our QFP system provides a novel route, such as the implementation of Hadamard and 3-D DFT gate, extension to higher dimensions has so far required too many resources for implementation [4].

In the present work, we propose an alternative solution to this problem. Instead of attempting to mix all frequency bins equally at once, we utilize a pulse shaper and an EOM to apply a series of random quantum operations to the input biphotons and follow with JSI measurements. At each measurement setting, the output frequency bin pairs consist of different superpositions of the input bins, with the weightings de-

[4]Please refer to Chapter 2.5 for discussion regarding implementation of high-dimensional DFT gates.

termined by the EO modulation depth. Though these measurements are not mutually unbiased, they are random enough such that we can utilize state-of-the-art Bayesian statistical methods to extract the posterior distribution of the density matrix and estimate the amount of the entanglement in the system.

6.2.2 Methods

Figure 6.7(a) illustrates our proposed method. Our test source is a BFC state generated directly from on-chip optical MRRs or carved from continuous down-conversion spectra. We follow the BFC state generation with a pulse shaper and EOM. The pulse shaper is programmed to apply a set of random spectral phases onto the signal and idler bins (a total set of $2d$ phases), and the EOM is driven by sinusoidal voltages periodic at the frequency-bin spacing ($\Delta\omega$), resulting in a temporal phase modulation $e^{i\delta sin\Delta\omega t}$. The strength of the modulating RF field δ is chosen randomly—in the simulation, we assume $\delta \in [0, d/2]$[5]; while in the experiment, δ is randomly chosen between 0 and 2.5 radian, with the range limited by the amount of RF power we can generate at specific frequency (40 GHz in this case). Figures 6.7(b) and (c) provide two examples of JSI measurement results for $d = 4$. When the EOM is off, i.e., $\delta = 0$, the JSI is depicted in Fig. 6.6(a). When the EOM is turned on, the frequency correlations become more complex as photons are scattered into many frequency modes, and the JSIs are no longer diagonal. Moreover, as discussed in Chapter 1.2, if we only consider the $d \times d$ computational space, the mode transformation in the EOM is not unitary, i.e., photons can be scattered outside the computational space. This explains why the number of coincidence counts drops in Fig. 6.7(b) and (c) as we increase the RF amplitude. This method is inspired by a recent paper (Imany *et al.* [146]), where they noticed that the distinct features in the two-photon frequency correlations in the presence of EO modulation depend on the input state (dubbed as the "quantum frequency walk"). Here we take one step forward and realize the

[5]The optimal range of δ is still under research. Here we choose $d/2$ since this modulation strength is large enough to mix the first and the d-th frequency bin.

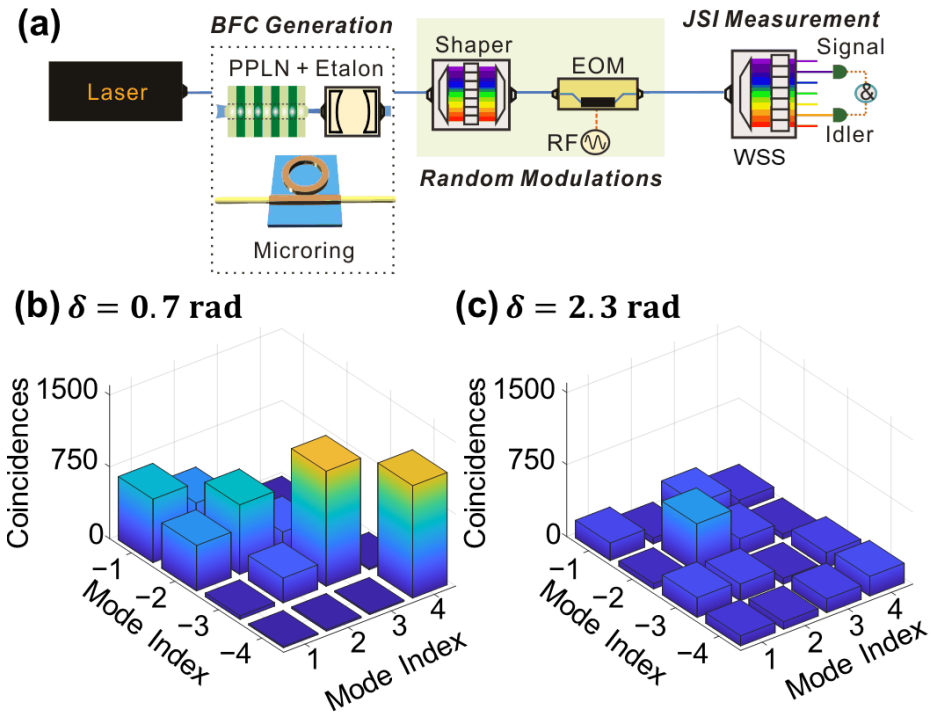

Fig. 6.7. **High-d Bayesian QST based on randomized measurements.** (a) Experimental setup. (b-c) Examples of random JSI measurements. See text for details.

retrieval of the unknown input state given the knowledge of the measurement results and the quantum operations applied in the system.

We consider a total of R measurement settings, the first of which is the traditional JSI measurements (i.e., EOM off), and the rest of which correspond to random spectral and temporal phase modulations applied by the shaper and the EOM. For each measurement setting, we collect coincidences for all d^2 combinations and disregard those photons scattered outside of the original subspace. We can thus construct a multinomial likelihood function

$$\mathcal{L}_D(\mathbf{x}) = \prod_{r=1}^{R} \prod_{m,n=1}^{d} \left[\frac{\langle f_{-m}, f_n | U_r \rho(\mathbf{x}) U_r^\dagger | f_{-m}, f_n \rangle}{\mathcal{Z}(\mathbf{x}, U_r)} \right]^{N_{mn}^{(r)}}. \tag{6.1}$$

where $N_{mn}^{(r)}$ is the measured coincidences between frequency mode f_{-m} (idler photon) and mode f_n (signal photon) at the r-th measurement setting, and $\mathcal{Z}(\mathbf{x}, U_r) =$

$\sum_{mn}\langle f_{-m}, f_n|U_r\rho(\mathbf{x})U_r^\dagger|f_{-m}, f_n\rangle$ normalizes the measurement outcome probabilities to sum to unity within the $d\times d$ computational space. The effect of pulse shapers and EOMs on two-photon state is given by $U_r = U_r^{(s)}\otimes U_r^{(i)}$, where $U_r^{(s)}$ and $U_r^{(i)}$ describe the random modulations [6] applied to signal and idler photons, respectively. $\rho(\mathbf{x})$ is the density matrix parameterized by some vector $\mathbf{x}$, and we follow the procedures developed in Ref. [116] such that any value within $\mathbf{x}$'s support returns a physical matrix. If we assume an uniform prior (i.e., no prior knowledge of $\mathbf{x}$), Bayes' theorem can immediately construct the posterior distribution of $\mathbf{x}$ from Eq. 6.1. Sampling this posterior distribution is equivalent to answering the following question—*Given the applied modulations, what are the possible states that can contribute to the photon counts distribution observed in the experiment?* Quantum states with higher likelihood than the others have better chance of being sampled in the Markov chain Monte Carlo (MCMC) algorithms. From the obtained density matrix samples, we can then estimate the mean and standard deviation of any function of interest (such as state fidelity).

6.2.3 Results

Figures 6.8(a) summarize our simulation results. We generate simulated tomographic data for entangled states in the form of Werner state [147]

$$\rho = \lambda\left|\Psi\right\rangle\left\langle\Psi\right| + \frac{1-\lambda}{d^2}I, \tag{6.2}$$

where $|\Psi\rangle = \frac{1}{\sqrt{d}}\sum_{k=1}^{d}|1_{f_{-k}}\rangle|1_{f_k}\rangle$ is the ideal, high-dimensional Bell state [an example of $d=4$ is depicted in Fig. 6.6(b)], and d is the dimension of each photon. I is the $d^2\times d^2$ identity matrix, and $\lambda\in[0,1]$ determines the overlap with respect to the ideal state $|\Psi\rangle$, i.e., fidelity $F_\rho = \frac{(d^2-1)\lambda+1}{d^2}$. Other useful metrics in quantum optics experiments can also be expressed by λ; for example, the coincidence-to-accidental

[6] $U_s^{(r)}$ and $U_i^{(r)}$ are infinite-dimensional mode transformation truncated to the dimension of each photo ($d\times d$ in this case). Please refer to Chapter 1 for detailed mathematical formalism.

ratio (CAR)—coincidences in a frequency-matched pair of bins divided by those in any mismatched pair—equals $1 + d\lambda/(1 - \lambda)$.

Here we consider the case of Werner state with $d = 5$ and two different λ (noise contributions). Photon counts are obtained by calculating the outcome probabilities in each measurement setting using Born's rule and drawing from a multinomial to emulate the experimental environment. Running the MCMC algorithm on these simulated datasets, we are able to estimate the state fidelity from the 1024 obtained samples. Bayesian mean fidelities converge to the theoretical prediction after $R \sim 10$ measurement settings, which is comparable to the traditional, full QST methods using mutually unbiased bases [$\sim (d + 1)^2$]. To quantify the amount of entanglement, we use log-negativity $E_{\mathcal{N}}(\rho) = \log_2 \|\rho^{\Gamma}\|_{\text{tr}}$ (ρ^{Γ} denotes the partial transpose of ρ and $\|\cdot\|_{\text{tr}}$ the trace norm), which gives an upper bound of distillable entanglement [148]. The amount of ebits in both scenarios match well with respect to theory.

Finally, we repeat this procedure using real experimental data, as depicted in Fig. 6.8(c). Our test source is a 40-GHz-spacing BFC with a total of 5 energy-correlated signal-idler pairs. We intentionally leave a $\sim$ 300-GHz gap between the signal and idler photons, such that we can apply strong EO modulations without any fear of the photon in signal modes jumping over to idler's modes, and vice versa. We adjust the pump power such that the CAR level is around 93, which if we assume a Werner state corresponds to the case $\lambda = 0.95$. We calculate the state fidelity with respect to the ideal state—a Bell state ($d = 5$) with additional quadratic phases accumulated in 20 meters of SMF-28 fiber [See Fig. 6.9(a) for its density matrix plots].

For $R = 1$ (single JSI measurement, EOM off), as discussed earlier, we have no information regarding the phase components of the states, let alone the phase coherence across the whole spectrum. The mean density matrix, as shown in Fig. 6.9(b), is very distinct from the ideal and resembles the classically mixed state. The fidelity starts to converge after $R \sim 10$ measurements, and for the final measurement $R = 21$, we report a state fidelity of $93 \pm 2\%$ and 2.23 ± 0.02 ebits[7]. Note that the theoret-

[7]Maximal amount of ebits for a bipartite is $\log_2 d$, equal to $\log_2 5 = 2.32$ ebits in this case

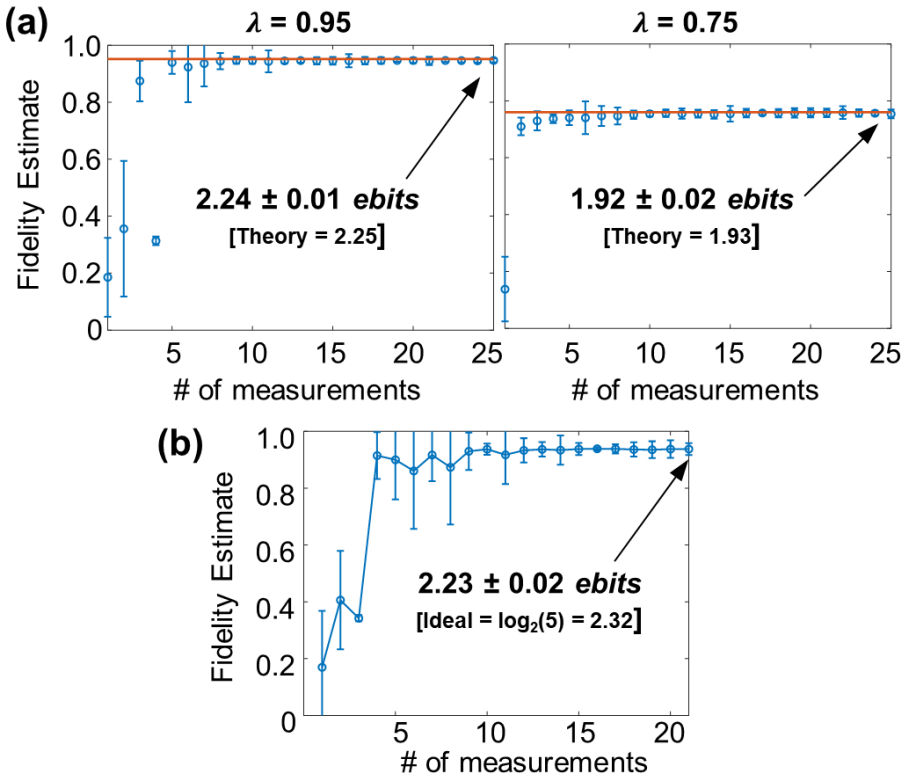

Fig. 6.8. **Summary of Bayesian QST results.** Convergence plots for (a) the $d = 5$ Werner state using simulated data sets, and (c) real experimental data sets for a $d = 5$ BFC input.

ical fidelity between the ideal Bell state and Werner state with $\lambda = 0.95$ is 95.2% in theory, which is consistent with the deviation in our fidelity from unity. Indeed, if we compute the fidelity with respect to the Werner state with $\lambda = 0.95$ instead, our converged fidelity is $98 \pm 2\%$, indicating strong overlap with a uniform noise model.

In this section, we propose and experimentally demonstrate high-dimensional QST using random measurements and Bayesian analysis to estimate the density matrix of a BFC state and quantify the dimensionality of the entanglement. There are various parts of our methods that are worth investigating in the future, including (i) connection to existing literature, (ii) the range and the number of EO amplitudes required, (iii) convergence for input states other than Werner states, etc. Nevertheless,

our preliminary results represent the highest dimensions demonstrated so far in the frequency-bin QIP community and can be effortlessly scaled to larger dimensions.

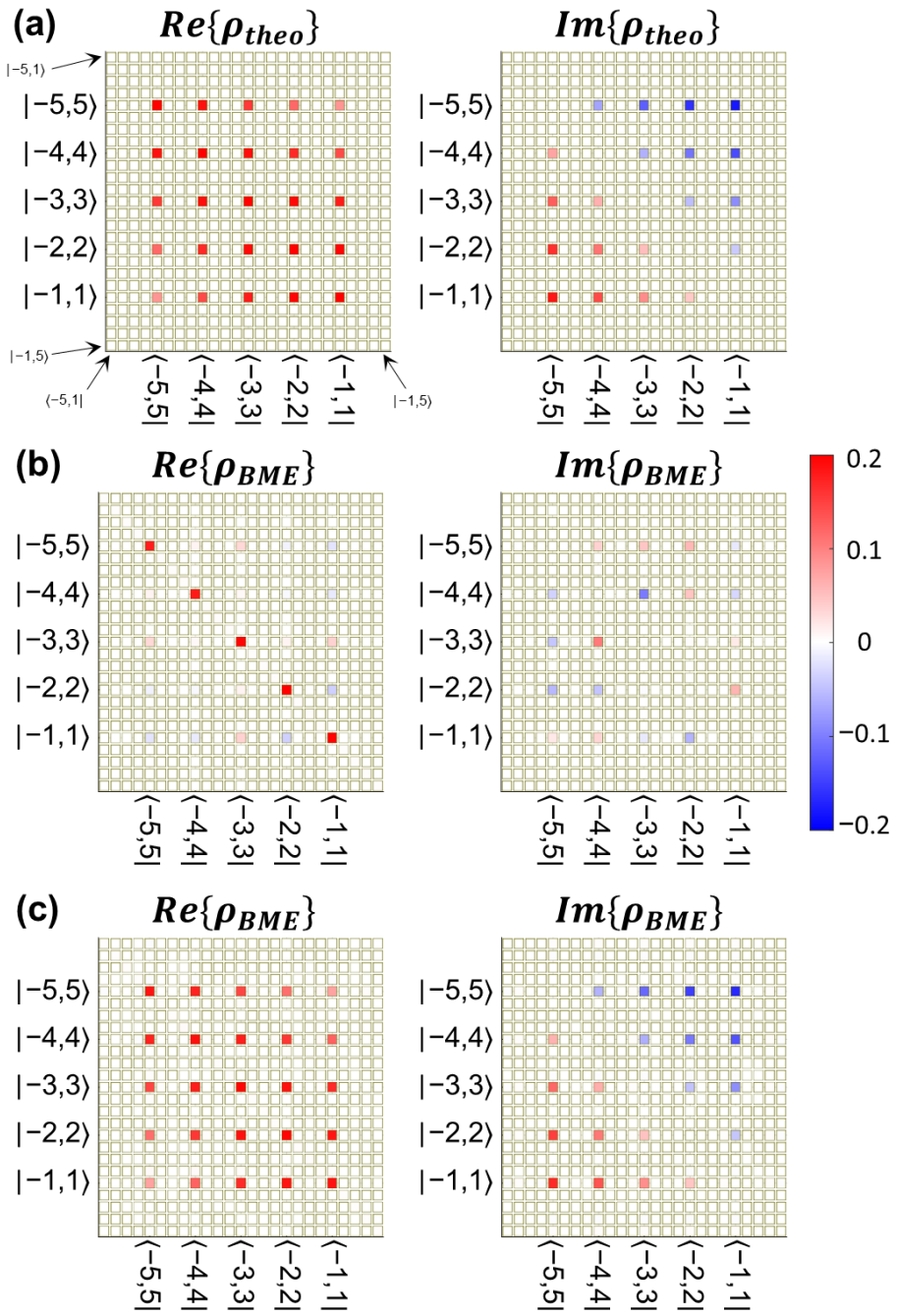

Fig. 6.9. **Density matrix plots.** (a) Ideal state, a $d = 5$ Bell states (cf. Eq. 6.2) with an added dispersion of 20-meter SMF fiber. (b-c) Real and imaginary part of the average density matrix from Bayesian QST, after a total number of (b) $R = 1$ and (c) $R = 21$ measurements.

6.3 In-Band Quantum Frequency Conversion (QFC)

6.3.1 Motivation

The management of optical wavelength resources is critical in classical communications, and will grow in importance for quantum communications as the size of deployed networks grows. Handling bandwidth contention at the network edge and interfacing with matter qubits will both benefit from agile conversion of optical carrier frequencies. In classical telecommunications, transferring data from one frequency channel onto another is a nontrivial task. From a practical side, the simplest approach is through optical-to-electrical-to-optical (OEO) conversion: detecting the symbols on one wavelength and electrically modulating them onto the desired output wavelength. However, such OEO conversion is precluded in any QIP protocol since optical detection inevitably destroys an arbitrary quantum state.

Accordingly, quantum frequency conversion (QFC) without OEO conversion is required. QFC has been the focus of dedicated research for many years, with typical approaches utilizing nonlinear parametric processes mediated by strong pump fields [66, 149, 150]. One approach that has shown particular promise is based on four-wave mixing Bragg scattering (FWM-BS), which has been demonstrated in both highly nonlinear fiber (HNLF) and optical microresonators. The FWM-BS process is particularly attractive because it supports QFC separations ranging from a few GHz to a few THz with, in theory, no additional noise. Conversion efficienes of 95% have been demonstrated in HNLF for separations of around 800 GHz [115], while frequency shifts tunable over a range of 0.7 THz – 1.7 THz have been reported using multiple pump fields [151]. One drawback to this approach is that suppression of Raman scattering requires low temperatures and one still needs optical filters to remove background noise from watt-class optical pumps. FWM-BS has also been demonstrated in nanophotonic platforms like silicon nitride [152–154], where resonant structures enable efficient QFC using pump fields with only tens of milliwatts of optical power. Light generated by quantum dots [153] and parametric down con-

verion [154] has been frequency shifted over hundreds of GHz, albeit with conversion efficiencies below 25%, as both up- and down-shifts occur with equal probability. Another drawback to this approach is that QFC is limited to multiples of the resonator free spectral range and the minimum achieveable shift is set by the dimensions of the device. In general, nonlinearity-based approaches are very suitable for interband QFC to transform photons in visible wavelengths (usually from stationary atomic memories) to traveling infrared photons for long-distance fiber transmission. However, arbitrary and reconfigurable control of QFC is extremely challenging with parametric approaches, which—coupled with the presence of noise (e.g., Raman) at optical wavelengths—poses difficulties for QFC in a DWDM network.

In terms of electro-optic approaches, one can use serrodyne modulation (sawtooth waveform) for unidirectional frequency shifts [155], but this method introduces unwanted distortion in the signal. Over the last couple of years, there have been several demonstrations of frequency swapping based on so-called "photonic molecules" or coupled-cavity EO modulators [49]. These devices mimic two-level systems and are capable of both frequency shifts and frequency swaps. While prototypes have delivered exceptional experimental results [114, 156, 157],the flexibility in choosing operating wavelengths and channel spacings remains unclear from the existing literature.

6.3.2 Methods and Preliminary Results

The QFP protocol offers a promising alternative to the standard QFC, especially for intraband-type conversion. The translation of optical frequencies is realized *all-optically*, yet the controls are pure electrical. This hybrid approach enables precise, reconfigurable frequency conversion within a specific band, while adding no extra noise to the quantum state. Moreover, the QFP allows not only uni-directional frequency shifts, but also *simultaneous* frequency swaps, interleaved frequency swaps, and any-to-any frequency hops in higher dimensions [61, 158]. [See Fig. 6.10].

Previously, we have experimentally demonstrated a Pauli-X gate [cf. Fig. 5.3] with near-unity fidelity and success probability close to 80% and 95% on a three-element setup driven by single and two RF tones, respectively. From the perspective of frequency-bin QIP, the Pauli-X gate can be visualized as an unitary operation which alters the quantum wave-function of a frequency-encoded single-qubit state. However, if a single photon (potentially carrying quantum information in another DoF) populates a single frequency mode, such an operation results in a unidirectional frequency conversion from, for example, mode 0 to mode 1; in addition, given two quantum signals originally occupying two different frequency channels, the Pauli-X gate realizes a *simultaneous* frequency swap between two input photons!

Due to the inherent high-dimensionality of the QFP platform, we can consider an even more general version of the frequency-swap operation—a cyclic frequency hop, which can be described by the $d \times d$ permutation matrix S_d, with elements

$$(S_d)_{mn} = \delta[(m - n - 1) \bmod d], \tag{6.3}$$

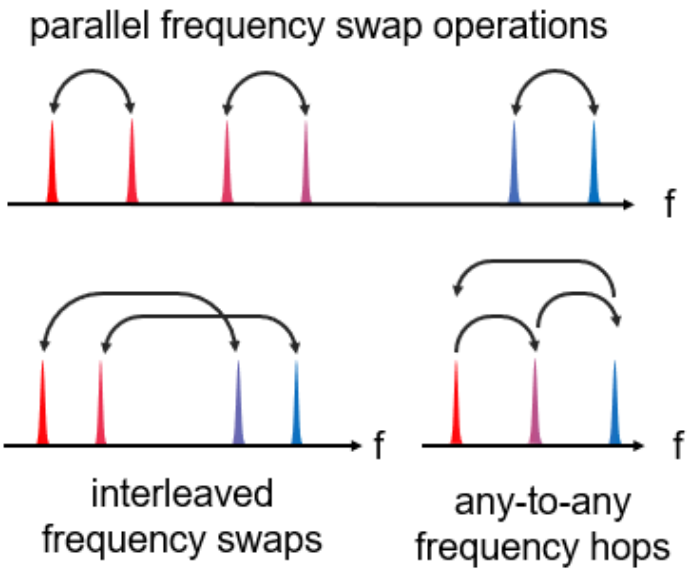

Fig. 6.10. **Frequency Hops with QFP.** Concept illustration of various forms of quantum frequency conversion supported by the quantum frequency processor protocol. [Courtesy of Navin Lingaraju]

and $m, n \in \{0, 1, ..., d-1\}$. In words, this transformation hops the fields at each frequency according to the prescription $\omega_0 \to \omega_1, \omega_1 \to \omega_2, ..., \omega_{d-1} \to \omega_0$. All other possible shifts that preserve this sense of ordering can then be written as powers of S_d: $S_d, S_d^2, ..., S_d^{d-1}$. ($S_d^d$ returns the identity and the sequence repeats.) Of these $d-1$ terms, only powers through floor$(d/2)$ need to be considered in design, as the remaining are simply transposes which can be obtained physically by reversing element order and conjugating all phases. We then repeat the optimization procedures and search for optimal solutions to implement cyclic frequency hop operations on a three-element QFP. Unlike the high-d DFT operation discussed earlier [cf. Chapter 2.5], there is no evident scaling relation between the dimension and the number of RF tones required. Appendix A summarize the results we obtained numerically, and the preliminary conclusion we can draw now is increasing the number of RF tones on a fixed QFP circuit does boost the success probability, but does not scale well

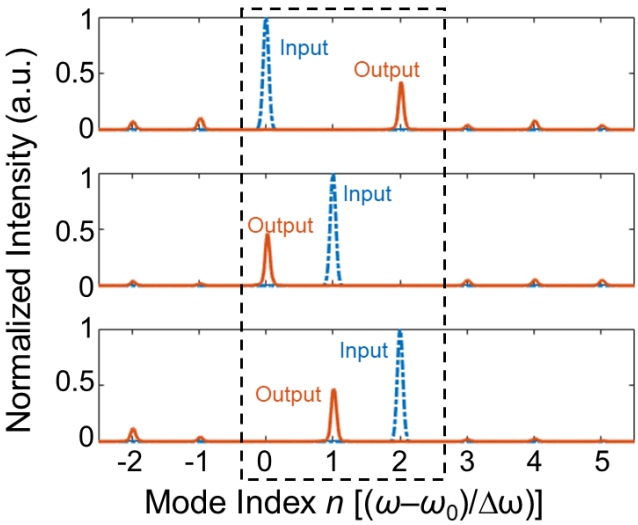

Fig. 6.11. **3-d cyclic hop.** Experimentally measured spectra for specific coherent state inputs. (a) Mode 0 $\to$ Mode 2, (b) Mode 1 $\to$ Mode 0, and (c) Mode 2 $\to$ Mode 1. The dashed box represents the computational space.

compared to the case of DFTs. Figure 6.11 is an example of experimentally obtained spectra for S_3^2 synthesized on our three-element QFP driven by two RF tones. [8]

Interestingly, we note that the chosen frequency-hopping transformation [Eq. (6.3)] can be related to the DFT operation F_d [Eq. (A.1)] by a straightforward decomposition: $S_d^x = F_d^\dagger D_d^x F_d$, where D_d is a diagonal matrix consisting of all dth roots of unity, i.e., $(D_d)_{mm} = e^{2\pi i m/d}$. This relationship implies that if one can realize the d-dimensional DFT, a permutation of any power follows simply by adding a pulse shaper and a second (conjugated) DFT. Since our previous exploration on high-D DFT operation suggests a three-element QFP with $d-1$ RF tones can potentially implement F_d with near-unity fidelity and success probability $\geq 95\%$ [cf. Chapter 2.5], a 4EOM/3PS system driven by $d-1$ RF tones should potentially realize any d-dimensional frequency cyclic hop, which can be an attractive route for future integrated QFP systems. Though more than doubling the number of components compared to the 2EOM/1PS QFP, such system offers better success probability ($\geq$ 95%) for all cyclic operations and does not require additional simulation to obtain the solution.

[8] This cyclic hop operation is equivalent to S_3^{-1}, which can be reconfigure from S_3 by reversing element order and conjugating phases.

7. FINAL THOUGHTS

In this dissertation, we have explored a thorough set of experiments in manipulating the quantum state of single and entangled photons in the frequency domain, including a universal gate set for scalable quantum computing; parallel quantum operations for two-qubit state control and tomography; arbitrary qubit rotations; and a frequency-domain Bell-state analyzer for potential applications such as dense coding, quantum teleportation, and entanglement swapping in future quantum networks. Each work represents a significant contribution to the field of frequency-bin QIP—though given that this field is still in an embryonic stage compared to other DoFs, it is difficult to predict its future directions and the specific roles our works will play.

At this point in time, there is still a huge gap between the development of tools to *generate* and to *control* such states. The presence of frequency entanglement is natural and ubiqutious since biphotons share the same temporal birth and follow energy conservation in the generation process. Indeed, generation of a broadband, frequency-entangled state is generally more straightforward than creating polarization-entangled photons. However, it was not until the past decade that scientists began developing the tools needed to explore this seemingly unbounded dimension of entanglement and further realize its potential. We have had the opportunity to be one of the pioneers to advance this field by filling that vacancy, but we also realize many more, general questions remain unsolved. For example, there remains the need to (i) develop quantum memories compatible with the frequency DoF, (ii) balance the tradeoffs in BFC sources (frequency-bin spacing is either too small to address, or too large to mix with), (iii) narrow the gap between the amount of inherent entanglement and the dimensionality we can truly exploit, (iv) derive analytical recipes for building arbitrary quantum operations, and (v) figure out the niche for the frequency DoF as the either the information carrier, an assisting DoF in hyper-entangled photons, or

a channel for information encoded in other DoFs. In addition to what we proposed in the outlook section at the end of each chapter, we believe the aforementioned questions can help trigger further discussion and help this community envision a future, large-scale quantum system based on photonic frequency.

REFERENCES

REFERENCES

[1] N. Picqué and T. W. Hänsch, "Frequency comb spectroscopy," *Nat. Photonics*, vol. 13, no. 3, pp. 146–157, 2019.

[2] S. T. Cundiff and J. Ye, "Colloquium: Femtosecond optical frequency combs," *Rev. Mod. Phys.*, vol. 75, no. 1, p. 325, 2003.

[3] S. T. Cundiff and A. M. Weiner, "Optical arbitrary waveform generation," *Nat. Photonics*, vol. 4, no. 11, pp. 760–766, 2010.

[4] V. Torres-Company and A. M. Weiner, "Optical frequency comb technology for ultra-broadband radio-frequency photonics," *Laser Photon. Rev.*, vol. 8, no. 3, pp. 368–393, May 2014.

[5] A. Baltuška, T. Udem, M. Uiberacker, M. Hentschel, E. Goulielmakis, C. Gohle, R. Holzwarth, V. Yakovlev, A. Scrinzi, T. W. Hänsch *et al.*, "Attosecond control of electronic processes by intense light fields," *Nature*, vol. 421, no. 6923, pp. 611–615, 2003.

[6] A. Cingöz, D. C. Yost, T. K. Allison, A. Ruehl, M. E. Fermann, I. Hartl, and J. Ye, "Direct frequency comb spectroscopy in the extreme ultraviolet," *Nature*, vol. 482, no. 7383, p. 68, 2012.

[7] M. T. Hassan, A. Wirth, I. Grguraš, A. Moulet, T. T. Luu, J. Gagnon, V. Pervak, and E. Goulielmakis, "Invited article: Attosecond photonics: Synthesis and control of light transients," *Rev. Sci. Instrm.*, vol. 83, no. 11, p. 111301, 2012.

[8] J. Ye and S. T. Cundiff, *Femtosecond optical frequency comb: principle, operation and applications*. Springer Science & Business Media, 2005.

[9] N. R. Newbury, "Searching for applications with a fine-tooth comb," *Nat. Photonics*, vol. 5, no. 4, pp. 186–188, Mar. 2011.

[10] Y. J. Lu, R. L. Campbell, and Z. Y. Ou, "Mode-locked two-photon states," *Phys. Rev. Lett.*, vol. 91, no. 16, p. 163602, Oct. 2003.

[11] M. Kues, C. Reimer, J. M. Lukens, W. J. Munro, A. M. Weiner, D. J. Moss, and R. Morandotti, "Quantum optical microcombs," *Nat. Photonics*, vol. 13, no. 3, pp. 170–179, Mar. 2019.

[12] J. M. Lukens and P. Lougovski, "Frequency-encoded photonic qubits for scalable quantum information processing," *Optica*, vol. 4, no. 1, pp. 8–16, 2017.

[13] C. Reimer, L. Caspani, M. Clerici, M. Ferrera, M. Kues, M. Peccianti, A. Pasquazi, L. Razzari, B. E. Little, S. T. Chu *et al.*, "Integrated frequency comb source of heralded single photons," *Opt. Express*, vol. 22, no. 6, pp. 6535–6546, 2014.

[14] C. Reimer, M. Kues, P. Roztocki, B. Wetzel, F. Grazioso, B. E. Little, S. T. Chu, T. Johnston, Y. Bromberg, L. Caspani, D. J. Moss, and R. Morandotti, "Generation of multiphoton entangled quantum states by means of integrated frequency combs," *Science*, vol. 351, no. 6278, pp. 1176–1180, Mar. 2016.

[15] J. A. Jaramillo-Villegas, P. Imany, O. D. Odele, D. E. Leaird, Z.-Y. Ou, M. Qi, and A. M. Weiner, "Persistent energy–time entanglement covering multiple resonances of an on-chip biphoton frequency comb," *Optica*, vol. 4, no. 6, pp. 655–658, Jun 2017.

[16] O. Pfister, "Continuous-variable quantum computing in the quantum optical frequency comb," *arXiv preprint arXiv:1907.09832*, 2019.

[17] J. Roslund, R. Medeiros de Araújo, S. Jiang, C. Fabre, and N. Treps, "Wavelength-multiplexed quantum networks with ultrafast frequency combs," *Nat. Photonics*, vol. 8, no. 2, pp. 109–112, Feb. 2014.

[18] M. Chen, N. C. Menicucci, and O. Pfister, "Experimental realization of multipartite entanglement of 60 modes of a quantum optical frequency comb," *Phys. Rev. Lett.*, vol. 112, no. 12, p. 120505, Mar. 2014.

[19] D. P. DiVincenzo, "The physical implementation of quantum computation," *Fortschritte der Physik: Progress of Physics*, vol. 48, no. 9-11, pp. 771–783, 2000.

[20] H.-H. Lu, A. M. Weiner, P. Lougovski, and J. M. Lukens, "Quantum information processing with frequency-comb qudits," *IEEE Photonics Technology Letters*, vol. 31, no. 23, pp. 1858–1861, 2019.

[21] H.-H. Lu, J. M. Lukens, N. A. Peters, O. D. Odele, D. E. Leaird, A. M. Weiner, and P. Lougovski, "Electro-optic frequency beam splitters and tritters for high-fidelity photonic quantum information processing," *Phys. Rev. Lett.*, vol. 120, no. 3, p. 030502, Jan. 2018.

[22] C. K. Hong, Z. Y. Ou, and L. Mandel, "Measurement of subpicosecond time intervals between two photons by interference," *Phys. Rev. Lett.*, vol. 59, no. 18, pp. 2044–2046, Nov. 1987.

[23] E. Knill, R. Laflamme, and G. J. Milburn, "A scheme for efficient quantum computation with linear optics," *Nature*, vol. 409, no. 6816, pp. 46–52, 2001.

[24] H.-H. Lu, J. M. Lukens, N. A. Peters, B. P. Williams, A. M. Weiner, and P. Lougovski, "Quantum interference and correlation control of frequency-bin qubits," *Optica*, vol. 5, no. 11, pp. 1455–1460, Nov. 2018.

[25] H.-H. Lu, J. M. Lukens, B. P. Williams, P. Imany, N. A. Peters, A. M. Weiner, and P. Lougovski, "A controlled-NOT gate for frequency-bin qubits," *npj Quantum Inf.*, vol. 5, p. 24, Mar. 2019.

[26] H.-H. Lu, E. M. Simmerman, P. Lougovski, A. M. Weiner, and J. M. Lukens, "Fully arbitrary control of frequency-bin qubits," *Phys. Rev. Lett.*, vol. 125, no. 12, p. 120503, 2020.

[27] C. H. Bennett and S. J. Wiesner, "Communication via one-and two-particle operators on einstein-podolsky-rosen states," *Phys. Rev. Lett.*, vol. 69, no. 20, p. 2881, 1992.

[28] C. H. Bennett, G. Brassard, C. Crépeau, R. Jozsa, A. Peres, and W. K. Wootters, "Teleporting an unknown quantum state via dual classical and einstein-podolsky-rosen channels," *Phys. Rev. Lett.*, vol. 70, pp. 1895–1899, Mar 1993. [Online]. Available: https://link.aps.org/doi/10.1103/PhysRevLett.70.1895

[29] Y. Shih, "Entangled biphoton source-property and preparation," *Rep. Prog. Phys.*, vol. 66, no. 6, p. 1009, 2003.

[30] A. M. Weiner, "Ultrafast optical pulse shaping: A tutorial review," *Opt. Commun.*, vol. 284, no. 15, pp. 3669–3692, Jul. 2011.

[31] D. Grassani, S. Azzini, M. Liscidini, M. Galli, M. J. Strain, M. Sorel, J. Sipe, and D. Bajoni, "Micrometer-scale integrated silicon source of time-energy entangled photons," *Optica*, vol. 2, no. 2, pp. 88–94, 2015.

[32] X. Guo, Y. Mei, and S. Du, "Testing the bell inequality on frequency-bin entangled photon pairs using time-resolved detection," *Optica*, vol. 4, no. 4, pp. 388–392, 2017.

[33] T. Kobayashi, R. Ikuta, S. Yasui, S. Miki, T. Yamashita, H. Terai, T. Yamamoto, M. Koashi, and N. Imoto, "Frequency-domain Hong–Ou–Mandel interference," *Nat. Photonics*, vol. 10, no. 7, pp. 441–444, 2016.

[34] T. Kobayashi, D. Yamazaki, K. Matsuki, R. Ikuta, S. Miki, T. Yamashita, H. Terai, T. Yamamoto, M. Koashi, and N. Imoto, "Mach-zehnder interferometer using frequency-domain beamsplitter," *Opt. Express*, vol. 25, no. 10, pp. 12 052–12 060, May 2017.

[35] H. J. McGuinness, M. G. Raymer, C. J. McKinstrie, and S. Radic, "Quantum frequency translation of single-photon states in a photonic crystal fiber," *Phys. Rev. Lett.*, vol. 105, p. 093604, Aug. 2010.

[36] S. Clemmen, A. Farsi, S. Ramelow, and A. L. Gaeta, "Ramsey interference with single photons," *Phys. Rev. Lett.*, vol. 117, no. 22, p. 223601, 2016.

[37] J. Carolan, C. Harrold, C. Sparrow, E. Martín-López, N. J. Russell, J. W. Silverstone, P. J. Shadbolt, N. Matsuda, M. Oguma, M. Itoh, G. D. Marshall, M. G. Thompson, J. C. F. Matthews, T. Hashimoto, J. L. O'Brien, and A. Laing, "Universal linear optics," *Science*, vol. 349, no. 6249, pp. 711–716, Aug. 2015.

[38] M. Reck, A. Zeilinger, H. J. Bernstein, and P. Bertani, "Experimental realization of any discrete unitary operator," *Phys. Rev. Lett.*, vol. 73, no. 1, pp. 58–61, Jul. 1994.

[39] A. M. Weiner, "Femtosecond pulse shaping using spatial light modulators," *Rev. Sci. Instrum*, vol. 71, no. 5, pp. 1929–1960, 2000.

[40] M. Shverdin, D. Walker, D. Yavuz, G. Yin, and S. Harris, "Generation of a single-cycle optical pulse," *Phys. Rev. Lett.*, vol. 94, no. 3, p. 033904, 2005.

[41] A. Pe'er, B. Dayan, A. A. Friesem, and Y. Silberberg, "Temporal shaping of entangled photons," *Phys. Rev. Lett.*, vol. 94, p. 073601, Feb. 2005.

[42] F. Zäh, M. Halder, and T. Feurer, "Amplitude and phase modulation of time-energy entangled two-photon states," *Opt. Express*, vol. 16, pp. 16 452–16 458, Oct. 2008.

[43] J. M. Lukens, A. Dezfooliyan, C. Langrock, M. M. Fejer, D. E. Leaird, and A. M. Weiner, "Demonstration of high-order dispersion cancellation with an ultrahigh-efficiency sum-frequency correlator," *Phys. Rev. Lett.*, vol. 111, p. 193603, 2013.

[44] C. Bernhard, B. Bessire, T. Feurer, and A. Stefanov, "Shaping frequency-entangled qudits," *Phys. Rev. A*, vol. 88, p. 032322, Sep 2013.

[45] J. M. Lukens, A. Dezfooliyan, C. Langrock, M. M. Fejer, D. E. Leaird, and A. M. Weiner, "Orthogonal spectral coding of entangled photons," *Phys. Rev. Lett.*, vol. 112, no. 13, p. 133602, 2014.

[46] Z. Jiang, D. E. Leaird, and A. M. Weiner, "Line-by-line pulse shaping control for optical arbitrary waveform generation," *Opt. Express*, vol. 13, no. 25, pp. 10 431–10 439, 2005.

[47] Z. Jiang, C.-B. Huang, D. E. Leaird, and A. M. Weiner, "Optical arbitrary waveform processing of more than 100 spectral comb lines," *Nat. Photonics*, vol. 1, no. 8, p. 463, 2007.

[48] A. J. Metcalf, V. Torres-Company, D. E. Leaird, and A. M. Weiner, "High-power broadly tunable electrooptic frequency comb generator," *IEEE J. Sel. Top. Quant. Electron.*, vol. 19, no. 6, pp. 231–236, 2013.

[49] M. Zhang, B. Buscaino, C. Wang, A. Shams-Ansari, C. Reimer, R. Zhu, J. M. Kahn, and M. Lončar, "Broadband electro-optic frequency comb generation in a lithium niobate microring resonator," *Nature*, vol. 568, no. 7752, p. 373, 2019.

[50] P. Kolchin, C. Belthangady, S. Du, G. Y. Yin, and S. E. Harris, "Electro-optic modulation of single photons," *Phys. Rev. Lett.*, vol. 101, p. 103601, Sep. 2008.

[51] S. Sensarn, G. Yin, and S. Harris, "Observation of nonlocal modulation with entangled photons," *Phys. Rev. Lett.*, vol. 103, no. 16, p. 163601, 2009.

[52] L. Olislager, J. Cussey, A. T. Nguyen, P. Emplit, S. Massar, J.-M. Merolla, and K. P. Huy, "Frequency-bin entangled photons," *Phys. Rev. A*, vol. 82, no. 1, p. 013804, 2010.

[53] M. Kues, C. Reimer, P. Roztocki, L. R. Cortés, S. Sciara, B. Wetzel, Y. Zhang, A. Cino, S. T. Chu, B. E. Little, D. J. Moss, L. Caspani, J. Azaña, and R. Morandotti, "On-chip generation of high-dimensional entangled quantum states and their coherent control," *Nature*, vol. 546, no. 7660, pp. 622–626, Jun. 2017.

[54] P. Imany, J. A. Jaramillo-Villegas, O. D. Odele, K. Han, D. E. Leaird, J. M. Lukens, P. Lougovski, M. Qi, and A. M. Weiner, "50-GHz-spaced comb of high-dimensional frequency-bin entangled photons from an on-chip silicon nitride microresonator," *Opt. Express*, vol. 26, no. 2, pp. 1825–1840, Jan. 2018.

[55] J. Nunn, L. Wright, C. Söller, L. Zhang, I. Walmsley, and B. Smith, "Large-alphabet time-frequency entangled quantum key distribution by means of time-to-frequency conversion," *Opt. Express*, vol. 21, no. 13, pp. 15 959–15 973, 2013.

[56] M. Karpiński, M. Jachura, L. J. Wright, and B. J. Smith, "Bandwidth manipulation of quantum light by an electro-optic time lens," *Nat. Photonics*, vol. 11, no. 1, p. 53, 2017.

[57] R. J. Glauber, "The quantum theory of optical coherence," *Phys. Rev.*, vol. 130, no. 6, p. 2529, 1963.

[58] L. Mandel and E. Wolf, *Optical coherence and quantum optics*. Cambridge university press, 1995.

[59] P. Imany, O. D. Odele, J. A. Jaramillo-Villegas, D. E. Leaird, and A. M. Weiner, "Characterization of coherent quantum frequency combs using electro-optic phase modulation," *Phys. Rev. A*, vol. 97, no. 1, p. 013813, 2018.

[60] P. Imany, O. D. Odele, M. S. Alshaykh, H.-H. Lu, D. E. Leaird, and A. M. Weiner, "Frequency-domain Hong-Ou-Mandel interference with linear optics," *Opt. Lett.*, vol. 43, no. 12, pp. 2760–2763, Jun. 2018.

[61] J. M. Lukens, H.-H. Lu, B. Qi, P. Lougovski, A. M. Weiner, and B. P. Williams, "All-optical frequency processor for networking applications," *J. Light. Technol*, vol. 38, no. 7, pp. 1678–1687, 2020.

[62] D. B. Uskov, L. Kaplan, A. M. Smith, S. D. Huver, and J. P. Dowling, "Maximal success probabilities of linear-optical quantum gates," *Phys. Rev. A*, vol. 79, p. 042326, Apr 2009.

[63] S. J. Devitt, W. J. Munro, and K. Nemoto, "Quantum error correction for beginners," *Rep. Prog. Phys.*, vol. 76, no. 7, p. 076001, 2013.

[64] R. H. Byrd, J. C. Gilbert, and J. Nocedal, "A trust region method based on interior point techniques for nonlinear programming," *Mathematical programming*, vol. 89, no. 1, pp. 149–185, 2000.

[65] K. E. Parsopoulos and M. N. Vrahatis, "Particle swarm optimization method for constrained optimization problems," *Intelligent Technologies–Theory and Application: New Trends in Intelligent Technologies*, vol. 76, no. 1, pp. 214–220, 2002.

[66] P. Kumar, "Quantum frequency conversion," *Opt. Lett.*, vol. 15, pp. 1476–1478, Dec. 1990.

[67] J. Huang and P. Kumar, "Observation of quantum frequency conversion," *Phys. Rev. Lett.*, vol. 68, pp. 2153–2156, Apr 1992.

[68] B. Brecht, A. Eckstein, A. Christ, H. Suche, and C. Silberhorn, "From quantum pulse gate to quantum pulse shaper—engineered frequency conversion in nonlinear optical waveguides," *New J. Phys.*, vol. 13, no. 6, p. 065029, 2011.

[69] A. Eckstein, B. Brecht, and C. Silberhorn, "A quantum pulse gate based on spectrally engineered sum frequency generation," *Opt. Express*, vol. 19, no. 15, pp. 13 770–13 778, Jul. 2011.

[70] B. Brecht, D. V. Reddy, C. Silberhorn, and M. G. Raymer, "Photon temporal modes: A complete framework for quantum information science," *Phys. Rev. X*, vol. 5, p. 041017, Oct 2015.

[71] P. Manurkar, N. Jain, M. Silver, Y.-P. Huang, C. Langrock, M. M. Fejer, P. Kumar, and G. S. Kanter, "Multidimensional mode-separable frequency conversion for high-speed quantum communication," *Optica*, vol. 3, no. 12, pp. 1300–1307, Dec 2016.

[72] D. V. Reddy and M. G. Raymer, "High-selectivity quantum pulse gating of photonic temporal modes using all-optical Ramsey interferometry," *Optica*, vol. 5, no. 4, pp. 423–428, Apr 2018.

[73] V. Ansari, J. M. Donohue, B. Brecht, and C. Silberhorn, "Tailoring nonlinear processes for quantum optics with pulsed temporal-mode encodings," *Optica*, vol. 5, no. 5, pp. 534–550, May 2018.

[74] F. Xu, X. M. Zhang, H.-K. Lo, J.-W. Pan *et al.*, "Quantum cryptography with realistic devices," *arXiv preprint arXiv:1903.09051*, 2019.

[75] D. Cozzolino, B. Da Lio, D. Bacco, and L. K. Oxenløwe, "High-dimensional quantum communication: Benefits, progress, and future challenges," *Advanced Quantum Technologies*, 2019.

[76] N. Sangouard, C. Simon, H. De Riedmatten, and N. Gisin, "Quantum repeaters based on atomic ensembles and linear optics," *Rev. Mod. Phys.*, vol. 83, no. 1, p. 33, 2011.

[77] N. Maring, P. Farrera, K. Kutluer, M. Mazzera, G. Heinze, and H. de Riedmatten, "Photonic quantum state transfer between a cold atomic gas and a crystal," *Nature*, vol. 551, no. 7681, p. 485, 2017.

[78] S. Osawa, D. S. Simon, and A. V. Sergienko, "Experimental demonstration of a directionally-unbiased linear-optical multiport," *Opt. Express*, vol. 26, no. 21, pp. 27 201–27 211, 2018.

[79] D. S. Simon, C. A. Fitzpatrick, S. Osawa, and A. V. Sergienko, "Quantum simulation of discrete-time hamiltonians using directionally unbiased linear optical multiports," *Phys. Rev. A*, vol. 95, no. 4, p. 042109, 2017.

[80] S. Osawa, D. S. Simon, and A. V. Sergienko, "Directionally-unbiased unitary optical devices in discrete-time quantum walks," *Entropy*, vol. 21, no. 9, p. 853, 2019.

[81] S. Rahimi-Keshari, M. A. Broome, R. Fickler, A. Fedrizzi, T. C. Ralph, and A. G. White, "Direct characterization of linear-optical networks," *Opt. Express*, vol. 21, no. 11, pp. 13 450–13 458, 2013.

[82] A. Zeilinger, H. Bernstein, D. Greenberger, M. Horne, and M. Zukowski, "Controlling entanglement in quantum optics," in *Quantum Control and Measurement*, H. Ezawa and Y. Murayama, Eds. Elsevier, 1993, pp. 9–22.

[83] A. J. Menssen, A. E. Jones, B. J. Metcalf, M. C. Tichy, S. Barz, W. S. Kolthammer, and I. A. Walmsley, "Distinguishability and many-particle interference," *Phys. Rev. Lett.*, vol. 118, p. 153603, Apr 2017.

[84] J. Wang, H. Shen, L. Fan, R. Wu, B. Niu, L. T. Varghese, Y. Xuan, D. E. Leaird, X. Wang, F. Gan, A. M. Weiner, and M. Qi, "Reconfigurable radio-frequency arbitrary waveforms synthesized in a silicon photonic chip," *Nat. Commun.*, vol. 6, p. 5957, Jan. 2015.

[85] M. Liscidini and J. Sipe, "Scalable and efficient source of entangled frequency bins," *Opt. Lett.*, vol. 44, no. 11, pp. 2625–2628, 2019.

[86] R. Ikuta, R. Tani, M. Ishizaki, S. Miki, M. Yabuno, H. Terai, N. Imoto, and T. Yamamoto, "Frequency-multiplexed photon pairs over 1000 modes from a quadratic nonlinear optical waveguide resonator with a singly resonant configuration," *Phy. Rev. Lett.*, vol. 123, no. 19, p. 193603, 2019.

[87] A. Einstein, B. Podolsky, and N. Rosen, "Can quantum-mechanical description of physical reality be considered complete?" *Phys. Rev.*, vol. 47, pp. 777–780, May 1935.

[88] P. Kok, W. J. Munro, K. Nemoto, T. C. Ralph, J. P. Dowling, and G. J. Milburn, "Linear optical quantum computing with photonic qubits," *Rev. Mod. Phys.*, vol. 79, pp. 135–174, Jan 2007.

[89] J. S. Bell, "On the einstein podolsky rosen paradox," *Physics Physique Fizika*, vol. 1, no. 3, p. 195, 1964.

[90] N. Gisin, G. Ribordy, W. Tittel, and H. Zbinden, "Quantum cryptography," *Rev. Mod. Phys.*, vol. 74, pp. 145–195, Mar. 2002.

[91] M. Raymer, S. van Enk, C. McKinstrie, and H. McGuinness, "Interference of two photons of different color," *Opt. Commun.*, vol. 283, no. 5, pp. 747–752, Mar. 2010.

[92] C. Joshi, A. Farsi, and A. Gaeta, "Hong-Ou-Mandel interference in the frequency domain," in *CLEO: 2017*. Optical Society of America, 2017, p. FF2E.3.

[93] R. Blume-Kohout, "Optimal, reliable estimation of quantum states," *New J. Phys.*, vol. 12, no. 4, p. 043034, 2010.

[94] B. P. Williams and P. Lougovski, "Quantum state estimation when qubits are lost: a no-data-left-behind approach," *New J. Phys.*, vol. 19, no. 4, p. 043003, 2017.

[95] H. Maassen and J. B. M. Uffink, "Generalized entropic uncertainty relations," *Phys. Rev. Lett.*, vol. 60, pp. 1103–1106, Mar 1988.

[96] P. J. Coles, M. Berta, M. Tomamichel, and S. Wehner, "Entropic uncertainty relations and their applications," *Rev. Mod. Phys.*, vol. 89, p. 015002, Feb 2017.

[97] T. B. Pittman, B. C. Jacobs, and J. D. Franson, "Probabilistic quantum logic operations using polarizing beam splitters," *Phys. Rev. A*, vol. 64, p. 062311, Nov 2001.

[98] T. C. Ralph, N. K. Langford, T. B. Bell, and A. G. White, "Linear optical controlled-NOT gate in the coincidence basis," *Phys. Rev. A*, vol. 65, no. 6, p. 062324, 2002.

[99] T. B. Pittman, B. C. Jacobs, and J. D. Franson, "Demonstration of nondeterministic quantum logic operations using linear optical elements," *Phys. Rev. Lett.*, vol. 88, p. 257902, Jun 2002.

[100] H. F. Hofmann and S. Takeuchi, "Quantum phase gate for photonic qubits using only beam splitters and postselection," *Phys. Rev. A*, vol. 66, p. 024308, Aug. 2002.

[101] J. L. O'Brien, G. J. Pryde, A. G. White, T. C. Ralph, and D. Branning, "Demonstration of an all-optical quantum controlled-NOT gate," *Nature*, vol. 426, no. 6964, pp. 264–267, Nov. 2003.

[102] S. Gasparoni, J.-W. Pan, P. Walther, T. Rudolph, and A. Zeilinger, "Realization of a photonic controlled-not gate sufficient for quantum computation," *Phys. Rev. Lett.*, vol. 93, no. 2, p. 020504, 2004.

[103] C. Eckart and F. R. Shonka, "Accidental coincidences in counter circuits," *Phys. Rev.*, vol. 53, pp. 752–756, May 1938.

[104] B. J. Pearson and D. P. Jackson, "A hands-on introduction to single photons and quantum mechanics for undergraduates," *Am. J. Phys.*, vol. 78, no. 5, pp. 471–484, 2010.

[105] D. J. C. MacKay, *Information Theory, Inference, and Learning Algorithms*. Cambridge, UK: Cambridge University Press, 2003.

[106] R. M. Neal, "Slice sampling," *Ann. Stat.*, vol. 31, no. 3, pp. 705–741, 2003.

[107] A. Peruzzo, J. McClean, P. Shadbolt, M.-H. Yung, X.-Q. Zhou, P. J. Love, A. Aspuru-Guzik, and J. L. O'Brien, "A variational eigenvalue solver on a photonic quantum processor," *Nat. Commun.*, vol. 5, p. 4213, 2014.

[108] A. Politi, J. C. Matthews, and J. L. O'Brien, "Shor's quantum factoring algorithm on a photonic chip," *Science*, vol. 325, no. 5945, pp. 1221–1221, 2009.

[109] J. F. Poyatos, J. I. Cirac, and P. Zoller, "Complete characterization of a quantum process: The two-bit quantum gate," *Phys. Rev. Lett.*, vol. 78, pp. 390–393, Jan 1997.

[110] I. L. Chuang and M. A. Nielsen, "Prescription for experimental determination of the dynamics of a quantum black box," *J. Mod. Opt.*, vol. 44, no. 11-12, pp. 2455–2467, 1997.

[111] J. L. O'Brien, G. J. Pryde, A. Gilchrist, D. F. V. James, N. K. Langford, T. C. Ralph, and A. G. White, "Quantum process tomography of a controlled-NOT gate," *Phys. Rev. Lett.*, vol. 93, p. 080502, Aug 2004.

[112] C. M. Dawson and M. A. Nielsen, "The Solovay–Kitaev algorithm," *arXiv:quant-ph/0505030*, 2005.

[113] M. A. Nielsen and I. L. Chuang, *Quantum Computation and Quantum Information*. Cambridge, 2000.

[114] M. Zhang, C. Wang, Y. Hu, A. Shams-Ansari, T. Ren, S. Fan, and M. Lončar, "Electronically programmable photonic molecule," *Nat. Photonics*, vol. 13, no. 1, p. 36, 2019.

[115] C. Joshi, A. Farsi, A. Dutt, B. Y. Kim, X. Ji, Y. Zhao, A. M. Bishop, M. Lipson, and A. L. Gaeta, "Frequency-domain quantum interference with correlated photons from an integrated microresonator," *Phys. Rev. Lett.*, vol. 124, no. 14, p. 143601, 2020.

[116] J. Lukens, K. Law, A. Jasra, and P. Lougovski, "A practical and efficient approach for Bayesian quantum state estimation," *New J. Phys.*, vol. 22, p. 063038, 2020.

[117] H. C. Lim, A. Yoshizawa, H. Tsuchida, and K. Kikuchi, "Broadband source of telecom-band polarization-entangled photon-pairs for wavelength-multiplexed entanglement distribution," *Opt. Express*, vol. 16, no. 20, pp. 16 052–16 057, 2008.

[118] D. Aktas, B. Fedrici, F. Kaiser, T. Lunghi, L. Labonté, and S. Tanzilli, "Entanglement distribution over 150 km in wavelength division multiplexed channels for quantum cryptography," *Laser Photonics Rev.*, vol. 10, no. 3, pp. 451–457, 2016.

[119] S. Wengerowsky, S. K. Joshi, F. Steinlechner, H. Hübel, and R. Ursin, "An entanglement-based wavelength-multiplexed quantum communication network," *Nature*, vol. 564, no. 7735, pp. 225–228, 2018.

[120] N. B. Lingaraju, H.-H. Lu, S. Seshadri, D. E. Leaird, A. M. Weiner, and J. M. Lukens, "Adaptive bandwidth management for entanglement distribution in quantum networks," *arXiv preprint arXiv:2010.10369*, 2020.

[121] J. F. Clauser, M. A. Horne, A. Shimony, and R. A. Holt, "Proposed experiment to test local hidden-variable theories," *Phys. Rev. Lett.*, vol. 23, pp. 880–884, Oct 1969. [Online]. Available: https://link.aps.org/doi/10.1103/PhysRevLett.23.880

[122] M. Erhard, M. Krenn, and A. Zeilinger, "Advances in high-dimensional quantum entanglement," *Nat. Rev. Phys.*, vol. 2, pp. 365–381, 2020.

[123] S. Wehner, D. Elkouss, and R. Hanson, "Quantum internet: A vision for the road ahead," *Science*, vol. 362, no. 6412, p. eaam9288, 2018. [Online]. Available: http://science.sciencemag.org/content/362/6412/eaam9288

[124] L.-M. Duan, M. D. Lukin, J. I. Cirac, and P. Zoller, "Long-distance quantum communication with atomic ensembles and linear optics," *Nature*, vol. 414, no. 6862, pp. 413–418, 2001.

[125] J. Calsamiglia and N. Lütkenhaus, "Maximum efficiency of a linear-optical bell-state analyzer," *Appl. Phys. B*, vol. 72, no. 1, pp. 67–71, 2001.

[126] K. Mattle, H. Weinfurter, P. G. Kwiat, and A. Zeilinger, "Dense coding in experimental quantum communication," *Phys. Rev. Lett.*, vol. 76, no. 25, p. 4656, 1996.

[127] D. E. Browne and T. Rudolph, "Resource-efficient linear optical quantum computation," *Physical Review Letters*, vol. 95, no. 1, p. 010501, 2005.

[128] N. Sangouard, C. Simon, B. Zhao, Y.-A. Chen, H. De Riedmatten, J.-W. Pan, and N. Gisin, "Robust and efficient quantum repeaters with atomic ensembles and linear optics," *Physical Review A*, vol. 77, no. 6, p. 062301, 2008.

[129] A. Dyckovsky and S. Olmschenk, "Analysis of photon-mediated entanglement between distinguishable matter qubits," *Phys. Rev. A*, vol. 85, no. 5, p. 052322, 2012.

[130] T.-M. Zhao, H. Zhang, J. Yang, Z.-R. Sang, X. Jiang, X.-H. Bao, and J.-W. Pan, "Entangling different-color photons via time-resolved measurement and active feed forward," *Phys. Rev. Lett.*, vol. 112, no. 10, p. 103602, 2014.

[131] G. Vittorini, D. Hucul, I. Inlek, C. Crocker, and C. Monroe, "Entanglement of distinguishable quantum memories," *Phys. Rev. A*, vol. 90, no. 4, p. 040302, 2014.

[132] O. E. Sandoval, N. B. Lingaraju, P. Imany, D. E. Leaird, M. Brodsky, and A. M. Weiner, "Polarization diversity phase modulator for measuring frequency-bin entanglement of a biphoton frequency comb in a depolarized channel," *Optics letters*, vol. 44, no. 7, pp. 1674–1677, 2019.

[133] M. Mirhosseini, O. S. Magaña-Loaiza, M. N. O'Sullivan, B. Rodenburg, M. Malik, M. P. Lavery, M. J. Padgett, D. J. Gauthier, and R. W. Boyd, "High-dimensional quantum cryptography with twisted light," *New J. Phys.*, vol. 17, no. 3, p. 033033, 2015.

[134] C. Wang, F.-G. Deng, Y.-S. Li, X.-S. Liu, and G. L. Long, "Quantum secure direct communication with high-dimension quantum superdense coding," *Phys. Rev. A*, vol. 71, no. 4, p. 044305, 2005.

[135] C. Wang, M. Zhang, X. Chen, M. Bertrand, A. Shams-Ansari, S. Chandrasekhar, P. Winzer, and M. Lončar, "Integrated lithium niobate electro-optic modulators operating at CMOS-compatible voltages," *Nature*, vol. 562, no. 7725, pp. 101–104, Oct. 2018.

[136] X. Qiang, X. Zhou, J. Wang, C. M. Wilkes, T. Loke, S. O'Gara, L. Kling, G. D. Marshall, R. Santagati, T. C. Ralph *et al.*, "Large-scale silicon quantum photonics implementing arbitrary two-qubit processing," *Nat. Photonics*, vol. 12, no. 9, pp. 534–539, 2018.

[137] H. J. Lee, S.-K. Choi, and H. S. Park, "Experimental demonstration of four-dimensional photonic spatial entanglement between multi-core optical fibres," *Sci. Rep.*, vol. 7, no. 1, pp. 1–8, 2017.

[138] M. Krenn, M. Huber, R. Fickler, R. Lapkiewicz, S. Ramelow, and A. Zeilinger, "Generation and confirmation of a (100× 100)-dimensional entangled quantum system," *Proc. Natl. Acad. Sci. U.S.A*, vol. 111, no. 17, pp. 6243–6247, 2014.

[139] F. Brandt, M. Hiekkamäki, F. Bouchard, M. Huber, and R. Fickler, "High-dimensional quantum gates using full-field spatial modes of photons," *Optica*, vol. 7, no. 2, pp. 98–107, 2020.

[140] H. Cao, S.-C. Gao, C. Zhang, J. Wang, D.-Y. He, B.-H. Liu, Z.-W. Zhou, Y.-J. Chen, Z.-H. Li, S.-Y. Yu *et al.*, "Distribution of high-dimensional orbital angular momentum entanglement over a 1 km few-mode fiber," *Optica*, vol. 7, no. 3, pp. 232–237, 2020.

[141] P. Imany, J. A. Jaramillo-Villegas, M. S. Alshaykh, J. M. Lukens, O. D. Odele, A. J. Moore, D. E. Leaird, M. Qi, and A. M. Weiner, "High-dimensional optical quantum logic in large operational spaces," *npj Quantum Inf.*, vol. 5, no. 1, pp. 1–10, Jul. 2019.

[142] A. Martin, T. Guerreiro, A. Tiranov, S. Designolle, F. Fröwis, N. Brunner, M. Huber, and N. Gisin, "Quantifying photonic high-dimensional entanglement," *Phys. Rev. Lett.*, vol. 118, no. 11, p. 110501, 2017.

[143] T. Ikuta and H. Takesue, "Implementation of quantum state tomography for time-bin qudits," *New J. Phys.*, vol. 19, no. 1, p. 013039, 2017.

[144] ——, "Four-dimensional entanglement distribution over 100 km," *Sci. Rep.*, vol. 8, no. 1, pp. 1–7, 2018.

[145] J.-P. W. MacLean, J. M. Donohue, and K. J. Resch, "Direct characterization of ultrafast energy-time entangled photon pairs," *Phys. Rev. Lett.*, vol. 120, no. 5, p. 053601, 2018.

[146] P. Imany, N. B. Lingaraju, M. S. Alshaykh, D. E. Leaird, and A. M. Weiner, "Probing quantum walks through coherent control of high-dimensionally entangled photons," *Sci. Adv.*, vol. 6, no. 29, p. eaba8066, 2020.

[147] R. F. Werner, "Quantum states with einstein-podolsky-rosen correlations admitting a hidden-variable model," *Phys. Rev. A*, vol. 40, no. 8, p. 4277, 1989.

[148] M. B. Plenio, "Logarithmic negativity: a full entanglement monotone that is not convex," *Phys. Rev. Lett.*, vol. 95, no. 9, p. 090503, 2005.

[149] J. Huang and P. Kumar, "Observation of quantum frequency conversion," *Phys. Rev. Lett.*, vol. 68, pp. 2153–2156, Apr 1992.

[150] S. Tanzilli, W. Tittel, M. Halder, O. Alibart, P. Baldi, N. Gisin, and H. Zbinden, "A photonic quantum information interface," *Nature*, vol. 437, no. 7055, pp. 116–120, 2005.

[151] C. Joshi, A. Farsi, S. Clemmen, S. Ramelow, and A. L. Gaeta, "Frequency multiplexing for quasi-deterministic heralded single-photon sources," *Nat. Commun.*, vol. 9, no. 1, pp. 1–8, 2018.

[152] Q. Li, M. Davanço, and K. Srinivasan, "Efficient and low-noise single-photon-level frequency conversion interfaces using silicon nanophotonics," *Nat. Photonics*, vol. 10, no. 6, pp. 406–414, 2016.

[153] A. Singh, Q. Li, S. Liu, Y. Yu, X. Lu, C. Schneider, S. Höfling, J. Lawall, V. Verma, R. Mirin *et al.*, "Quantum frequency conversion of a quantum dot single-photon source on a nanophotonic chip," *Optica*, vol. 6, no. 5, pp. 563–569, 2019.

[154] Q. Li, A. Singh, X. Lu, J. Lawall, V. Verma, R. Mirin, S. W. Nam, and K. Srinivasan, "Tunable quantum beat of single photons enabled by nonlinear nanophotonics," *Phys. Rev. Appl.*, vol. 12, no. 5, p. 054054, 2019.

[155] D. Johnson, J. Hogan, S.-W. Chiow, and M. Kasevich, "Broadband optical serrodyne frequency shifting," *Opt. Lett.*, vol. 35, no. 5, pp. 745–747, 2010.

[156] Y. Hu, M. Yu, D. Zhu, N. Sinclair, A. Shams-Ansari, L. Shao, J. Holzgrafe, E. Puma, M. Zhang, and M. Loncar, "Reconfigurable electro-optic frequency shifter," *arXiv preprint arXiv:2005.09621*, 2020.

[157] H. Gevorgyan, A. Khilo, and M. A. Popović, "Active-cavity photonic molecule optical data wavelength converter for silicon photonics platforms," *arXiv preprint arXiv:2005.04989*, 2020.

[158] H.-H. Lu, B. Qi, B. P. Williams, P. Lougovski, A. M. Weiner, and J. M. Lukens, "Agile frequency transformations for dense wavelength-multiplexed communications," *Opt. Express*, vol. 28, no. 14, pp. 20 379–20 390, 2020.

[159] H.-H. Lu, N. Klco, J. M. Lukens, T. D. Morris, A. Bansal, A. Ekström, G. Hagen, T. Papenbrock, A. M. Weiner, M. J. Savage *et al.*, "Simulations of subatomic many-body physics on a quantum frequency processor," *Phys. Rev. A*, vol. 100, no. 1, p. 012320, 2019.

APPENDICES

A. GATE SIMULATION RESULTS

- **Procedures:**

  1. Particle swarm optimization to minimize the following cost function (C): When $\mathcal{F} < 0.9999$, $C = \mathcal{P} log_{10}(1-\mathcal{F})$; otherwise, $C = -4\mathcal{P}$
  2. Followed by interior-point method (*fmincon*) with the previous best particle as the initial guess. Minimize $1-\mathcal{P}$ with $\mathcal{F}$ constrained over 0.9999.
  3. See Ch 1.3 for more details.

- **Parameters:** A total of $\boldsymbol{Q}$ **elements** (EOMs+PSs).

  Sum of sinewaves in the EO modulation (a total number of $\boldsymbol{p}$ **harmonics**).

  – **Goal:** d-dimensional discrete Fourier transform (DFT) gate,

$$[F_d]_{mn} = \frac{1}{\sqrt{d}} e^{2\pi i \frac{mn}{d}}; \quad m, n \in \{0, 1, ..., d-1\} \tag{A.1}$$

Q	d	p	$log_{10}(1-\mathcal{F})$	$\mathcal{P}$	**Filename**	**Implemented?**
3	2	1	-4.0	0.9760	20200826-2-48	Y [21]
	2	1	-6.0	0.9748	20200827-2-48	Y [159]
	3	2	-4.0	0.9733	20200826-3-48	Y [21]
	4	3	-3.9	0.9703	20200826-4-48	N
	5	4	-3.8	0.9679	20200826-5-48	
	6	5	-3.8	0.9665	20200826-6-48	
	7	6	-3.7	0.9685	20200826-7-48	
	8	7	-3.6	0.9688	20200826-8-48	
	9	8	-3.6	0.9668	20200826-9-48	
	10	9	-3.6	0.9681	20200826-10-48	

– **Discussions:**

  * In our demonstration of frequency beamsplitter (2-d DFT) and tritter (3-d DFT) in [21], we notice a favorable scaling between the dimension of the DFT and the number of RF harmonics (p) introduced to the EO modulation, without increasing the total number of components (Q).

  * A more balanced beamsplitter is implemented in [159], where we utilize parallel Hadamard gates for the purpose of quantum simulation of sub-atomic many-body physics. The fidelity is increased to $1 - 10^{-6}$, with only a minor reduction in the success probability.

– **Example: 7-dimensional DFT Gate**

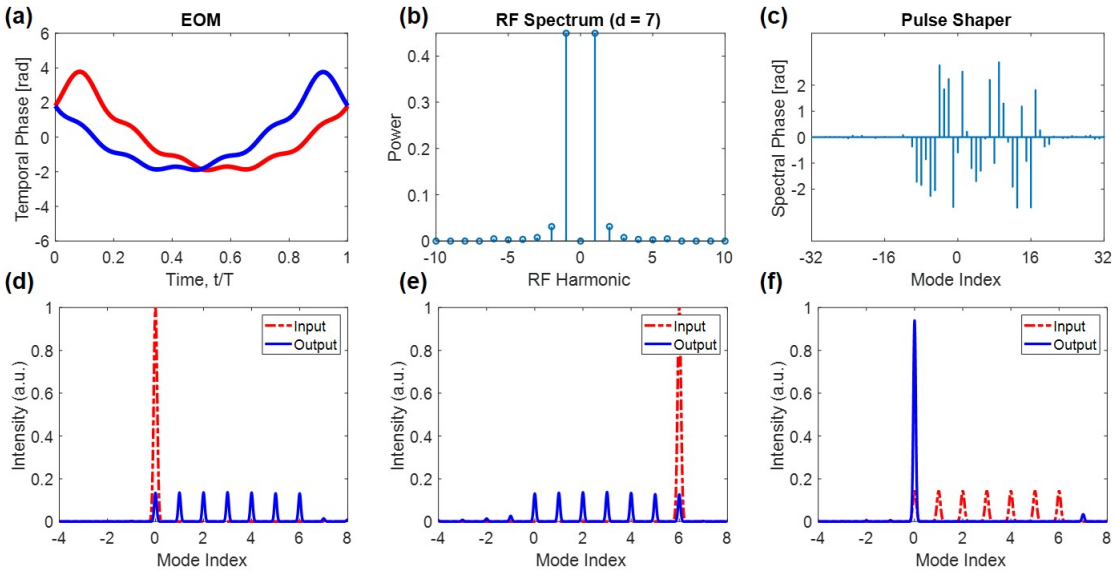

Fig. A.1. **7-dimensional DFT gate design.** (a) temporal phase modulation applied to the first EOM [red] and second EOM [blue], plotted over one period T. (b) Corresponding microwave power spectra for the first EOM. (c) phases applied to each frequency mode by the PS, where modes 0 to 6 denote the computational space. (d-f) Simulated optical transformation for single-line inputs and superposition of seven comb lines input.

– **Goal:** d-dimensional Pauli-X gate,

$$[S_d]_{mn} = \delta[(m-n-1) \bmod d]; \quad m,n \in \{0,1,...,d-1\}, \\ \text{and consider } S_d, S_d^2, ..., S_d^{d-1} \text{ for all possible frequency hops.} \tag{A.2}$$

– **Discussion:** A traditional Pauli-X gate ($d = 2$) realizes a frequency hop operation between the two computational states (i.e., $\omega_0 \rightarrow \omega_1, \omega_1 \rightarrow \omega_0$), while high-dimensional Pauli-X performs frequency cyclic hops for all frequency modes. We only focus on $d = 2$ at this point, while our recent paper [61] provides more results (with slightly different constraints, $\mathcal{F}, \mathcal{P} \geq 0.99$) for larger d. From the limited data sets we possess, the realization of Pauli-X is relatively difficult, and will require more resources than the DFT gates.

Q	d	p	$log_{10}(1-\mathcal{F})$	$\mathcal{P}$	**Filename**	**Implemented?**
3	2	1	-4	0.7590	328-001	Y
3	2	2	-4	0.9458	328-002	Y
5	2	1	-7	0.9955	5-328-002	N
3	3	2	-4	0.4590	0621-3	N
		3		0.5887	20200927-3	N
		4		0.7184	20200927-4	N
		5		0.7660	20200927-5	N
		10		0.8356	20200927-10	N
	$4(S_4)$	4		0.4876	20200926-4	N
		5		0.6240	20200927-5	N
		6		0.6507	20200927-6	N
		10		0.7471	20200927-10	N
	$4(S_4^2)$	4		0.5601	20200926-4	N
		5		0.6279	20200927-5	N
		6		0.7174	20200927-6	N
		10		0.8515	20200927-10	N
	$5(S_5)$	7		0.4586	20200928-7	N
		8		0.6782	20200929-8	N
		9		0.7151	20200929-9	N
		10		0.7355	20200929-10	N
	$5(S_5^2)$	8		0.6625	20200930-8	N
		9		0.6937	20200930-9	N
		10		0.7071	20200930-10	N
	$6(S_6)$	8		0.3569	20200930-8	N
		9		0.6533	20200930-9	N
		10		0.6766	20200930-10	N

– **Goal:** Coincidence-basis CNOT gate.

$$U = \begin{pmatrix} 1 & 0 & 0 & 0 \\ 0 & 1 & 0 & 0 \\ 0 & 0 & 0 & 1 \\ 0 & 0 & 1 & 0 \end{pmatrix} \tag{A.3}$$

Q	p	$1-\mathcal{F}$	$\mathcal{P}$	**Filename**	**Implemented?**
3	1	10^{-4}	0.0445	1104-001	Y [25]
5	1	10^{-4}	1/9	1105-002	N

– **Method:** Assume the computational-basis states for the two-qubit Hilbert space are: $|C_0T_0\rangle$, $|C_0T_1\rangle$, $|C_1T_0\rangle$, and $|C_1T_1\rangle$[1], where C_0, C_1, T_0, and T_1 represents a specific frequency bin for encoding [cf. Fig. 4.3]. In the numerical optimization procedures, we firstly construct the *mode* transformation V using Eq. 1.9, and then calculate the *state* transformation W as

$$W_{C_pT_q \leftarrow C_mT_n} = V_{C_pC_m}V_{T_qT_n} + V_{C_pT_n}V_{T_qC_m};\ \{m,n,p,q\} \in \{0,1\}, \tag{A.4}$$

– **Discussion:** For a 3EOM/2PS QFP ($Q = 5$), we can realize a frequency-bin CNOT at the theoretical optimal success probability of $\mathcal{P} = 1/9$, while a smaller circuit ($Q = 3$) can do so with reduced success.

– **Numerical Solution ($Q = 3$):** $V = [r_{nn'} \angle \phi_{nn'}] =$

$$\begin{bmatrix} 0.4407\angle -2.5976 & 0.0022\angle 0.2103 & 0.0026\angle 1.2938 & 0.0010\angle -2.0353 \\ 0.0022\angle 0.2104 & 0.4343\angle -2.6045 & 0.4596\angle -1.5754 & 0.4549\angle 1.5710 \\ 0.0026\angle 1.2939 & 0.4596\angle -1.5754 & 0.4830\angle 2.5973 & 0.0030\angle -2.8778 \\ 0.0010\angle -2.0352 & 0.4549\angle 1.5710 & 0.0030\angle -2.8779 & 0.4783\angle 2.5979 \end{bmatrix}. \tag{A.5}$$

[1]Usually expressed as $|00\rangle$, $|01\rangle$, $|10\rangle$, and $|11\rangle$ for shorthand notation.

using the phasor shorthand $r_{nn'}\angle\phi_{nn'} \equiv r_{nn'}e^{i\phi_{nn'}}$. We can use Eq. A.4 to compute the corresponding state transformation matrix

$W = [r_{nn'}\angle\phi_{nn'}] =$

$$\begin{bmatrix} 0.2128\angle{-1.0882} & 0.0013\angle{-0.2822} & 0.0001\angle{-0/9929} & 0.0005\angle 1.5953 \\ 0.0013\angle{-0.2823} & 0.2108\angle{-1.0877} & 0.0012\angle 1.7805 & 0.0006\angle 1.8263 \\ 0.0001\angle{-0.9930} & 0.0012\angle 1.7805 & 0.0015\angle 1.7557 & 0.2100\angle{-1.0880} \\ 0.0005\angle 1.5954 & 0.0006\angle 1.8264 & 0.2100\angle{-1.0880} & 0.0016\angle{-2.1786} \end{bmatrix}, \tag{A.6}$$

where the four large elements (highlighted in red) share almost identical amplitude and phase, aligned well with respect to those in the Eq. A.3.

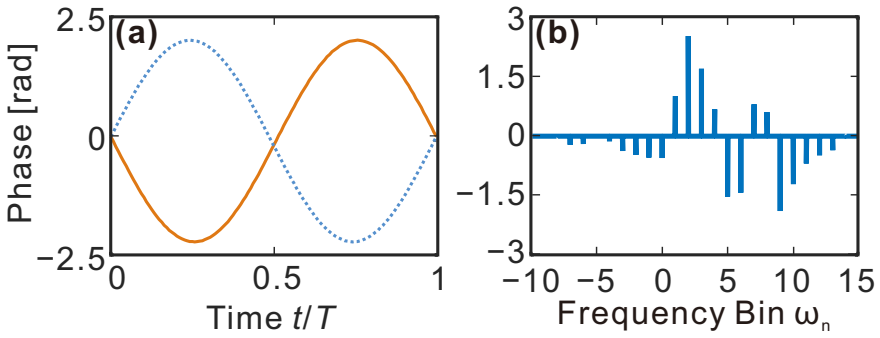

Fig. A.2. **CNOT gate design.** Numerical solutions found for the time-frequency phases required to implement the coincidence-basis CNOT gate on a 2EOM/1PS QFP circuit, with a theoretical performance of $\mathcal{F} = 0.9999$ and $\mathcal{P} = 0.0445$. (a) Temporal phase modulation applied to the first [solid red] and second [dotted blue] EOM, plotted over on period T. (b) Spectral phase applied to each frequency mode by the pulse shaper, where modes 0 and 6 denote the control bins $\{C_0, C_1\}$, and modes 7 and 8 represent the target bins $\{T_0, T_1\}$.

B. PROCEDURE FOR MEASURING TRANSFORMATION MATRIX

Our calculations of $\mathcal{F}$ and $\mathcal{P}$ rely on complete characterization of the $d \times d$ multiport $V_{d\times d}$. We utilize an analogue of the spatial technique shown in Ref. [81], and here we provide additional details on precisely how to determine each of the matrix elements. This technique relies on high-power coherent state probing, which is justified because the operation of interest is, at its basic level, a linear multiport; thus its distinguishing behavior holds for high-flux coherent states as well as single photons.

The definition of success probability $\mathcal{P}$ is

$$\mathcal{P} = \frac{\mathrm{Tr}(V_{d\times d}^{\dagger} V_{d\times d})}{\mathrm{Tr}(U^{\dagger} U)} = \frac{\mathrm{Tr}(V_{d\times d}^{\dagger} V_{d\times d})}{d}, \tag{B.1}$$

where U is the desired state transformation and $V_{d\times d}$ denotes the infinite-dimensional transformation V truncated to the dimension of U[1]. This can be written equivalently as

$$\mathcal{P} = \frac{1}{d} \sum_{m=0}^{d-1} \sum_{n=0}^{d-1} |V_{mn}|^2, \tag{B.2}$$

from which we see that $\mathcal{P}$ depends on only the moduli of the d^2 matrix elements. To find these values, we probe our frequency multiport with a single optical frequency from index $n = 0$ to $d - 1$. The information we need to calculate $\mathcal{P}$, namely $|V_{mn}|^2$, is then given by the output optical power in mode m when the input is set to n. And by measuring the total throughput of the system in all modes (even those beyond d), we can normalize each matrix element by overall transmissivity, distinguishing the insertion loss (photon is missing) from scatter loss (photon remains, but has left d-dimensional subspace), so that $\mathcal{P}$ can quantify the latter. Thus, a value $\mathcal{P} = 1$ means

[1]For single-qudit operation, the *state* transformation W is equivalent to the *mode* transformation V operating on the $d \times d$ computational space, thus we have $W = V_{d\times d}$ for calculation of $\mathcal{P}$ and $\mathcal{F}$.

that, given that the input photon exits the system, it is guaranteed to have undergone the desired operation and has remained in the d-mode computational subspace.

On the other hand, the fidelity $\mathcal{F}$ involves the full Hilbert-Schmidt inner product:

$$\mathcal{F} = \frac{\mathrm{Tr}(V_{d\times d}^{\dagger} U)\,\mathrm{Tr}(U^{\dagger} V_{d\times d})}{\mathrm{Tr}(V_{d\times d}^{\dagger} V_{d\times d})\,\mathrm{Tr}(U^{\dagger} U)}, \tag{B.3}$$

or alternatively

$$\mathcal{F} = \frac{1}{d^2\mathcal{P}} \left| \sum_{m=0}^{d-1} \sum_{n=0}^{d-1} V_{mn}^{*} U_{mn} \right|^2, \tag{B.4}$$

which indeed depends on the phase and amplitude information of $V_{d\times d}$. To determine these phases, we next probe the setup with superpositions of two frequency modes, scanning the relative phase ϕ from 0 to 2π. Extracting the power in specific modes from a series of optical spectra yields interference patterns over ϕ, and the unknown phase terms in $V_{d\times d}$ can be obtained by performing sinusoidal fitting on each curve.

In our experiments, we apply the above technique to $d = 2$ and $d = 3$. The corresponding frequency multiport matrices are $V_{2\times 2}$ and $V_{3\times 3}$, and the input optical field $E(t) = \sum_{m=0}^{d-1} \sqrt{p_m} e^{i\phi_m} e^{-i\omega_n t}$ can be expressed in mode matrix form as $[\sqrt{p_0} e^{i\phi_0}\ \sqrt{p_1} e^{i\phi_1} \cdots \sqrt{p_{d-1}} e^{i\phi_{d-1}}]^T$. We write a general matrix element of $V_{d\times d}$ in polar form as $V_{mn} = r_{mn} e^{i\phi_{mn}}$. Since phase is only physically meaningful up to a unitary rotation, we follow the procedure of Ref. [81] and define the phases of the first row and column as zero: this effectively provides a reference for zero phase on our input state preparation. Finally, though the matrices in the following equations are expressed in d dimensions for brevity, experimentally the optical power can be scattered out of the d-mode computational space into adjacent sidebands. Therefore, the sensitivity of the OSA should be high enough so that we can collect the optical power in as many modes as possible for accurate normalization. Experimentally, we found that only 6-8 modes were needed to encompass all the optical power (to within 10^{-4} accuracy).

The tests cases for a single-frequency-mode probe are (note that the OSA functions as a frequency-resolved square-law detector):

$\boxed{2\times 2}$

$$\begin{bmatrix} r_{00} & r_{01} \\ r_{10} & r_{11}e^{i\phi_{11}} \end{bmatrix} \begin{bmatrix} \sqrt{p} \\ 0 \end{bmatrix} = \sqrt{p} \begin{bmatrix} r_{00} \\ r_{10} \end{bmatrix} \xrightarrow{\text{OSA}} p \begin{bmatrix} r_{00}^2 \\ r_{10}^2 \end{bmatrix}$$

$$\begin{bmatrix} r_{00} & r_{01} \\ r_{10} & r_{11}e^{i\phi_{11}} \end{bmatrix} \begin{bmatrix} 0 \\ \sqrt{p} \end{bmatrix} = \sqrt{p} \begin{bmatrix} r_{01} \\ r_{11}e^{i\phi_{11}} \end{bmatrix} \xrightarrow{\text{OSA}} p \begin{bmatrix} r_{01}^2 \\ r_{11}^2 \end{bmatrix}$$

$\boxed{3\times 3}$

$$\begin{bmatrix} r_{00} & r_{01} & r_{02} \\ r_{10} & r_{11}e^{i\phi_{11}} & r_{12}e^{i\phi_{12}} \\ r_{20} & r_{21}e^{i\phi_{21}} & r_{22}e^{i\phi_{22}} \end{bmatrix} \begin{bmatrix} \sqrt{p} \\ 0 \\ 0 \end{bmatrix} = \sqrt{p} \begin{bmatrix} r_{00} \\ r_{10} \\ r_{20} \end{bmatrix} \xrightarrow{\text{OSA}} p \begin{bmatrix} r_{00}^2 \\ r_{10}^2 \\ r_{20}^2 \end{bmatrix}$$

$$\begin{bmatrix} r_{00} & r_{01} & r_{02} \\ r_{10} & r_{11}e^{i\phi_{11}} & r_{12}e^{i\phi_{12}} \\ r_{20} & r_{21}e^{i\phi_{21}} & r_{22}e^{i\phi_{22}} \end{bmatrix} \begin{bmatrix} 0 \\ \sqrt{p} \\ 0 \end{bmatrix} = \sqrt{p} \begin{bmatrix} r_{01} \\ r_{11}e^{i\phi_{11}} \\ r_{21}e^{i\phi_{21}} \end{bmatrix} \xrightarrow{\text{OSA}} p \begin{bmatrix} r_{01}^2 \\ r_{11}^2 \\ r_{21}^2 \end{bmatrix}$$

$$\begin{bmatrix} r_{00} & r_{01} & r_{02} \\ r_{10} & r_{11}e^{i\phi_{11}} & r_{12}e^{i\phi_{12}} \\ r_{20} & r_{21}e^{i\phi_{21}} & r_{22}e^{i\phi_{22}} \end{bmatrix} \begin{bmatrix} 0 \\ 0 \\ \sqrt{p} \end{bmatrix} = \sqrt{p} \begin{bmatrix} r_{02} \\ r_{12}e^{i\phi_{12}} \\ r_{22}e^{i\phi_{22}} \end{bmatrix} \xrightarrow{\text{OSA}} p \begin{bmatrix} r_{02}^2 \\ r_{12}^2 \\ r_{22}^2 \end{bmatrix} \tag{B.5}$$

We thus see that by these measurements we can obtain all d^2 amplitudes of $V_{d\times d}$. Subsequently, we probe the system with superpositions of two frequency modes, and scan the relative phase $\phi \in [0, 2\pi]$ between them. The different configurations are:

$\boxed{2\times 2}$

$$\begin{bmatrix} r_{00} & r_{01} \\ r_{10} & r_{11}e^{i\phi_{11}} \end{bmatrix} \begin{bmatrix} \sqrt{p} \\ \sqrt{p}e^{i\phi} \end{bmatrix} = \sqrt{p} \begin{bmatrix} r_{00} + r_{01}e^{i\phi} \\ r_{10} + r_{11}e^{i(\phi+\phi_{11})} \end{bmatrix} \xrightarrow{\text{OSA}} p \begin{bmatrix} r_{00}^2 + r_{01}^2 + 2r_{00}r_{01}\cos\phi \\ r_{10}^2 + r_{11}^2 + 2r_{10}r_{11}\cos(\phi+\phi_{11}) \end{bmatrix}$$

$\boxed{3\times 3}$

$$\begin{bmatrix} r_{00} & r_{01} & r_{02} \\ r_{10} & r_{11}e^{i\phi_{11}} & r_{12}e^{i\phi_{12}} \\ r_{20} & r_{21}e^{i\phi_{21}} & r_{22}e^{i\phi_{22}} \end{bmatrix} \begin{bmatrix} \sqrt{p} \\ \sqrt{p}e^{i\phi} \\ 0 \end{bmatrix} \xrightarrow{\text{OSA}} p \begin{bmatrix} r_{00}^2 + r_{01}^2 + 2r_{00}r_{01}\cos\phi \\ r_{10}^2 + r_{11}^2 + 2r_{10}r_{11}\cos(\phi+\phi_{11}) \\ r_{20}^2 + r_{21}^2 + 2r_{20}r_{21}\cos(\phi+\phi_{21}) \end{bmatrix}$$

$$\begin{bmatrix} r_{00} & r_{01} & r_{02} \\ r_{10} & r_{11}e^{i\phi_{11}} & r_{12}e^{i\phi_{12}} \\ r_{20} & r_{21}e^{i\phi_{21}} & r_{22}e^{i\phi_{22}} \end{bmatrix} \begin{bmatrix} \sqrt{p} \\ 0 \\ \sqrt{p}e^{i\phi} \end{bmatrix} \xrightarrow{\text{OSA}} p \begin{bmatrix} r_{00}^2 + r_{02}^2 + 2r_{00}r_{02}\cos\phi \\ r_{10}^2 + r_{12}^2 + 2r_{10}r_{12}\cos(\phi+\phi_{12}) \\ r_{20}^2 + r_{22}^2 + 2r_{20}r_{22}\cos(\phi+\phi_{22}) \end{bmatrix} \tag{B.6}$$

For each curve, we then perform sinusoidal fitting with respect to the input phase ϕ and obtain all the phase values in $V_{d\times d}$. And from this, we can calculate fidelity $\mathcal{F}$.

To give an idea of what our measurements produce, we provide two examples of matrices obtained using the previous characterization method. An example mode transformation for the beamsplitter is

$$V_{2\times 2} = \begin{bmatrix} \sqrt{0.4871} & \sqrt{0.4869} \\ \sqrt{0.4866} & \sqrt{0.4871}e^{i3.1400} \end{bmatrix}. \tag{B.7}$$

These values correspond to $\mathcal{P} = 0.9739$ and $\mathcal{F} = 0.9999$ when compared to the ideal Hadamard gate. Error bars from repeating the full characterization four more times then gave $\mathcal{P} = 0.9739 \pm 0.0003$ and $\mathcal{F} = 0.99998 \pm 0.00003$.

For the three-mode DFT, an example transformation measured is

$$V_{3\times 3} = \begin{bmatrix} \sqrt{0.3261} & \sqrt{0.3126} & \sqrt{0.3062} \\ \sqrt{0.3183} & \sqrt{0.3290}e^{i2.0925} & \sqrt{0.3339}e^{i4.1775} \\ \sqrt{0.3202} & \sqrt{0.3476}e^{i4.1365} & \sqrt{0.3256}e^{i2.0425} \end{bmatrix}, \tag{B.8}$$

with associated success $\mathcal{P} = 0.9731$ and fidelity $\mathcal{F} = 0.9992$ with respect to the perfect (i.e., not numerically simulated) DFT matrix. Averaging over five repeated measurements then yielded $\mathcal{P} = 0.9730 \pm 0.0002$ and $\mathcal{F} = 0.9989 \pm 0.0004$, as in the main text [cf. Chapter 2.2].

C. BAYESIAN MEAN ESTIMATION MODEL

C.1 Entanglement Witness

To calculate the conditional entropies corresponding to the measurements shown in Fig. 3.5, we employ Bayesian mean estimation (BME) on the raw count data [93,94]. To produce as conservative an estimate as possible, we make no specifying assumptions about the underlying state. For each situation in Fig. 3.5, we posit a three-parameter multinomial likelihood function (four probabilities minus normalization), with counts taken directly from the raw data; we take the prior as uniform. The estimated means and standard deviations of the conditional entropies are then calculated, as shown in Eq. 3.9.

C.2 Two-Qubit Density Matrix Reconstruction

To estimate the complete two-qubit density matrix, we assume a single quantum state underlying all four measurements in Fig. 3.5. As discussed in Chapter 3.5, these four combinations are equivalent to joint measurements of the two-qubit observables $\{Z_A \otimes Z_B, X_A \otimes Z_B, Z_A \otimes X_B, X_A \otimes X_B\}$, where $\mathbb{1}$ and H permits measurement of Z and X, respectively. Despite the fact that our measurements is tomographically incomplete, we are nevertheless able to infer a complete state estimate, with appropriately higher uncertainties in the unmeasured bases (e.g., Pauli Y). Finally, we emphasize that experimentally we only have access to the detector click (or no-click) events that are more naturally described in terms of positive-operator valued measures (POVMs) rather than von Neumann type projectors on the eigenvectors of Pauli X and Z operators.

For a specific two-qubit observable and chosen pair of frequency bins, we have the POVMs $\Lambda^{(A,B)} = \{\hat{\Pi}^{(A,B)}, \mathbb{1} - \hat{\Pi}^{(A,B)}\}$ for subsystem A and B, where $\hat{\Pi}^{(A,B)}$ correspond to photon clicks, $\mathbb{1} - \hat{\Pi}^{(A,B)}$ to the absence of a click. Absence of a click can be due to detection inefficiency or the photon being in an unmonitored mode. An outcome of a two-qubit POVM $\Lambda^{(A)} \otimes \Lambda^{(B)}$ will fall into one of the three experimentally recorded numbers: coincidence counts (C_{AB}), singles counts on detector A (S_A), and singles counts on detector B (S_B). These form our specific data set $\mathcal{D} = \{C_{AB}, S_A, S_B\}$. In our model, we assume fixed channel efficiencies for A and B propagation and detection (η_A and η_B), and the following normalized probabilities under no loss and perfect detection: p_{AB} (coincidence, one photon in mode A and one photon in mode B), p_{A0} (one photon in mode A and no photon in mode B), p_{0B} (one photon in mode B and no photon in mode A), p_{00} (no photon in mode A or B).

Letting N denote the number of photon pairs generated in the measured time interval, we can enumerate the following four experimental possibilities, formed by the products of all operators from this POVM pair (✓: click, ✗: no click).

POVMs	A	B	**Occurrence Probability**	**Counts**
$\hat{\Pi}^{(A)} \otimes \hat{\Pi}^{(B)}$	✓	✓	$\eta_A \eta_B p_{AB}$	C_{AB}
$\hat{\Pi}^{(A)} \otimes [\mathbb{1} - \hat{\Pi}^{(B)}]$	✓	✗	$\eta_A[p_{AB}(1-\eta_B) + p_{A0}]$	$S_A - C_{AB}$
$[\mathbb{1} - \hat{\Pi}^{(A)}] \otimes [\hat{\Pi}^{(B)}]$	✗	✓	$\eta_B[p_{AB}(1-\eta_A) + p_{0B}]$	$S_B - C_{AB}$
$[\mathbb{1} - \hat{\Pi}^{(A)}] \otimes [\mathbb{1} - \hat{\Pi}^{(B)}]$	✗	✗	$p_{00} + p_{AB}(1-\eta_A)(1-\eta_B)$ $+ \mathrm{p}_{A0}(1-\eta_A) + p_{0B}(1-\eta_B)$	$N - S_A - S_B + C_{AB}$

Our likelihood function, $P(\mathcal{D}|\beta)$, is then a multinomial distribution over the aforementioned probabilities and outcomes, where $\beta = \{\hat{\rho}, \eta_A, \eta_B, N\}$ is the underlying parameter set of interest. The idealized probabilities $\{p_{AB}, p_{A0}, p_{0B}, p_{00}\}$ are all functions of the density matrix $\hat{\rho}$, which we limit to physically allowable states [94].

Up to this point, we have focused on a *specific* choice of POVMs, $\Lambda^{(A)} \otimes \Lambda^{(B)}$. To account for all 16 POVM combinations (basis pairs and frequency-bin pairs) in

the two-qubit space of Fig. 3.5, we form the product over all settings, leaving the complete posterior distribution

$$P(\beta|\boldsymbol{\mathcal{D}}) = \frac{\left[\prod_j P(\mathcal{D}_j|\beta)\right] P(\beta)}{P(\boldsymbol{\mathcal{D}})}, \tag{C.1}$$

where the bolded $\boldsymbol{\mathcal{D}}$ represents the union of the respective results $\mathcal{D}_j$ from each particular setting ($j = 1, 2, ..., 16$). Our prior $P(\beta)$ is taken to be uniform in a Haar-invariant sense, and the marginal $P(\boldsymbol{\mathcal{D}})$ is found by integrating the numerator in Eq. (C.1). With this posterior distribution, we can estimate any parameter of interest via integration, such as the mean density matrix

$$\hat{\rho}_{\mathrm{BME}} = \int d\beta \; P(\beta|\boldsymbol{\mathcal{D}})\hat{\rho}. \tag{C.2}$$

Due to the complexity of integrals of this form, we employ numerical slice sampling for their evaluation [106]. The resulting estimates are discussed in the main text and plotted in Fig. 3.6.

C.3 CNOT Gate Characterization

In order to make use of the observed data to estimate the key parameters of our quantum gate, we first derive a realistic model connecting the underlying gate operation to photon counts, encapsulated in a likelihood function $P(\boldsymbol{\mathcal{D}}|\beta)$, for the model parameters β given data $\boldsymbol{\mathcal{D}}$. In our case, the set β contains mode transformation matrix V, pair generation probability μ and the system efficiencies η_A and η_B.

For a particular counting experiment, we take the prepared input state as

$$|\Psi\rangle = |1_u 1_v\rangle = \hat{a}_u^\dagger \hat{a}_v^\dagger |\mathrm{vac}\rangle, \tag{C.3}$$

where $u \neq v$. Specifying such a state relies on several assumptions. First of all, it discards any contribution from other frequency-bin pairs, justified experimentally by the >40 dB extinction ratio on the BFC shaper. Moreover, this state expression—and the multiport model in general—treats each frequency bin as a pure single mode.

Experimentally, as a consequence of the pump laser's ∼kHz linewidth (much narrower than our 1.8 GHz-thick bins determined by the etalon), a given photon pair is highly frequency-entangled, containing substructure absent in the separable state of Eq. (C.3). While such hidden entanglement would markedly reduce, e.g., the purity of *heralded* frequency-bin photons, it does not degrade the correlations in the two-photon experiments we conduct here. The counts registered for a particular pair of bins do result from a continuum of photon pairs with slightly different frequency offsets, implying that the net result is the incoherent sum of partially distinguishable probability amplitudes. However, as all such frequency pair combinations under the same bin lineshapes undergo matching frequency operations, the net measurement result is identical to the case in which all bins are purely single mode, apart from an overall scaling constant (see discussion of frequency filtering below). Finally, Eq. (C.3) does not include higher-order pair generation explicitly. Incidentally, the ansatz we incorporate for accidental coincidences [see Eq. (C.9) below] ends up capturing the main effects of multiple photon pairs on our data in a simpler fashion.

We define $p_\mu(1_m 1_n)$ as the probability for one photon to be found in mode m and the other in mode n at the output (again assuming no loss). This is given by

$$p_\mu(1_m 1_n) = \left| \frac{\langle \mathrm{vac} | \hat{b}_m^\dagger \hat{b}_n^\dagger \hat{a}_u \hat{a}_v | \mathrm{vac} \rangle}{\sqrt{1+\delta_{mn}}} \right|^2 = \frac{|V_{mu}V_{nv} + V_{mv}V_{nu}|^2}{1+\delta_{mn}}. \tag{C.4}$$

When $n = m$ (two photons in the same mode), the probability is

$$p_\mu(2_m) = 2\,|V_{mu}V_{mv}|^2\,, \tag{C.5}$$

with the factor of two a consequence of boson statistics. From these results, we can also compute the marginal probability for one-photon occupancy in a particular mode,

$$\begin{aligned} p_\mu(1_m) &= \sum_{\substack{n=-\infty \\ n\neq m}}^{\infty} |V_{mu}V_{nv} + V_{mv}V_{nu}|^2 \\ &= \sum_{n=-\infty}^{\infty} \Big(|V_{mu}V_{nv} + V_{mv}V_{nu}|^2 \Big) - 4|V_{mu}V_{mv}|^2 \\ &= |V_{mu}|^2 + |V_{mv}|^2 - 4|V_{mu}V_{mv}|^2, \end{aligned} \tag{C.6}$$

where all the cross terms are neglected, following from the unitarity of V and the fact that $u \neq v$ in our input state.

We then map these fundamental "per-pair" probabilities to expected detection rates. For accounting purposes, we define all detection probabilities within a specific temporal frame τ, the time within which clicks on detector A (t_A) and B (t_B) are deemed coincident: $|t_A - t_B| < \tau$. Our stationary (continuous-wave pumped) source ensures that all such probabilities are equal in every length-τ time bin. With μ defined as the pair generation probability within such a frame, the marginal probabilities for single-detector clicks are

$$\begin{aligned} p_A &= \mu\left[\eta_A + (1-\eta_A)\eta_A\right] p_\mu(2_m) + \mu\eta_A p_\mu(1_m) + d_A \\ p_B &= \mu\left[\eta_B + (1-\eta_B)\eta_B\right] p_\mu(2_n) + \mu\eta_B p_\mu(1_n) + d_B \end{aligned} \tag{C.7}$$

for detector A monitoring frequency bin m and B frequency bin n. These marginal probabilities include three terms: (i) both photons arrive, but detector misses one, (ii) one photon arrives, and detector registers one click, and (iii) no photon arrives, but detector fires due to dark counts. The probabilities d_A and d_B represent the dark count probabilities; we measure these independently and take them as fixed at $d_A = 9.60 \times 10^{-7}$ and $d_B = 7.77 \times 10^{-7}$, corresponding to dark count rates of 640 Hz and 518 Hz, respectively. The efficiencies η_A and η_B include all loss effects through the system, from generation in the crystal to photon detection; we assume them to be mode-independent—validated by the relatively small bandwidth comprising all modes of interest ($\sim$500 GHz)—yet they can vary by the different relative efficiencies of our superconducting nanowire detectors. And while spectral filtering *per se* does not modify these general considerations, the multimode frequency substructure (mentioned above), coupled with the Lorentzian linewidth profile of the etalon, introduces an effective transmission given by the average over all frequency offsets—we believe this contributes to lower overall η_A and η_B retrieved in BME. Next we make use of

the fact that the system efficiencies $\eta_A, \eta_B \ll 1$. Plugging in Eqs. (C.5) and (C.6), we obtain

$$\begin{aligned} p_A &= \mu\eta_A\Big(|V_{mu}|^2 + |V_{mv}|^2\Big) + d_A \\ p_B &= \mu\eta_B\Big(|V_{nu}|^2 + |V_{nv}|^2\Big) + d_B. \end{aligned} \tag{C.8}$$

The simple addition of pair and dark-count contributions is justified in our case by their small values ($\sim 10^{-6}$), so that there is no concern for p_A or p_B approaching or exceeding 1 in the numerical analysis below.

To establish the probability for a coincidence between detectors A and B in our model, we make a sharp distinction between two types of events: (i) correlated coincidences, deriving from two photons of the same pair; and (ii) accidental coincidences, in which two random clicks (from at least one dark count, or photons from two different pairs) overlap within the resolving time τ. For event (i), the click probability follows from multiplying the per-pair probability $p_\mu(1_m 1_n)$ by $\mu\eta_A\eta_B$, so that $p_{AB}^{(\mathrm{i})} = \mu\eta_A\eta_B\,|V_{mu}V_{nv} + V_{mv}V_{nu}|^2$, which assumes that τ is sufficiently large to integrate over the full two-photon correlation time. Regarding event (ii), in general the rate of accidental coincidences between two independent detectors is given by a product of the rates of the two detectors individually: $R_{AB}^{(\mathrm{ii})} = 2\tau R_A R_B$ [103, 104], where the factor of two follows from the fact that—under our definition of τ—all events such that $(t_A - t_B) \in (-\tau, \tau)$ register as coincidences. Making the connection $p_j = \tau R_j$ then allows us to write $p_{AB}^{(\mathrm{ii})} = 2p_A p_B$, so that the total coincidence probability becomes

$$\begin{aligned} p_{AB} &= p_{AB}^{(\mathrm{i})} + p_{AB}^{(\mathrm{ii})} \\ &= \mu\eta_A\eta_B\Big|V_{mu}V_{nv} + V_{mv}V_{nu}\Big|^2 + 2p_A p_B, \end{aligned} \tag{C.9}$$

with p_A and p_B defined as in Eq. (C.8). Expanding $2p_A p_B$, the expected noise sources appear naturally: a μ^2 term reflects clicks from two different pairs, while μd_A and μd_B terms give coincidences from a photon and dark count. In this way, we can recover noise effects otherwise absent in the physical model, via what can be called

an "accidentals correction" term $2p_Ap_B$. Finally, we emphasize that the accuracy of Eq. (C.9) relies again on the relative order of magnitudes of the probabilities involved: $p_{AB}^{(\mathrm{i})} \sim 10^{-10}$, so that the differences between alternative forms one could conceivably argue for—such as $p_B \to p_B - p_{AB}^{(\mathrm{i})}$, to help ensure that singles counts from correlated coincidences do not also count toward accidental probabilities—become numerically inconsequential.

Finally, with these probabilities established, we can write the likelihood using a multinomial distribution for all event types. Over the course of a single measurement of duration T, we experience $M = T/\tau$ total frames, in which we can register one of the four mutually exclusive outcomes: click on A only, click on B only, coincidence, or no clicks. The likelihood for the specific input/output mode configuration (defined by the mode numbers $uv \to mn$) is

$$\begin{aligned} P\left(\mathcal{D}_{uv}^{mn}|\beta\right) &= \left(p_A - p_{AB}\right)^{N_A - N_{AB}} \left(p_B - p_{AB}\right)^{N_B - N_{AB}} \\ &\quad \times p_{AB}^{N_{AB}} \left(1 - p_A - p_B + p_{AB}\right)^{M - N_A - N_B + N_{AB}}, \end{aligned} \tag{C.10}$$

where we emphasize that both the dataset $\mathcal{D}_{uv}^{mn} = \{N_A, N_B, N_{AB}\}$ and probabilities $\{p_A, p_B, p_{AB}\}$ themselves depend on the mode configuration $uvmn$. The total likelihood follows by multiplying out all 16 individual combinations

$$P\left(\boldsymbol{\mathcal{D}}|\beta\right) = \prod_{\substack{u,m \in \{C_0, C_1\} \\ v,n \in \{T_0, T_1\}}} P\left(\mathcal{D}_{uv}^{mn}|\beta\right). \tag{C.11}$$

This likelihood forms the basis for estimating the parameters $\beta = \{V, \mu, \eta_A, \eta_B\}$ from the dataset $\boldsymbol{\mathcal{D}} = \bigcup \mathcal{D}_{uv}^{mn}$. To estimate these values along with their uncertainties, we make use of Bayes' rule for the posterior probability distribution

$$P(\beta|\boldsymbol{\mathcal{D}}) \propto P\left(\boldsymbol{\mathcal{D}}|\beta\right) P(\beta), \tag{C.12}$$

$P(\beta)$ represents the prior probability distribution for the parameters. We take $P(\beta)$ as uniform over $(0, 1)$ for each of μ, η_A, and η_B; uniform over $(0, 2\pi)$ for all phases $\phi_{nn'} = \arg V_{nn'}$ which are not taken as fixed $\{\phi_{C_0C_0}, \phi_{C_1C_1}, \phi_{C_1T_0}, \phi_{C_1T_1}, \phi_{T_0C_1}, \phi_{T_1C_1}\}$; and uniform for all squared moduli $r_{nn'}^2$ subject to the constraint $\sum_{nn'} r_{nn'}^2 = 1.6558$

from Eq. (A.5). This uninformative prior allows the estimates to be fully determined by the counting data itself.

Due to the complexity of integrating Eq. (C.12) over our parameter space, we employ slice sampling [106] and retrieve 4096 samples of all 28 parameters from the unnormalized $P(\boldsymbol{\mathcal{D}}|\beta)\,P(\beta)$. We use best guesses of all parameters as the starting point to enable convergence, invoking a burn-in period and thinning until stationarity is achieved. At each sample of β, we can compute any quantity of interest, and use the statistics over all samples to produce the mean and standard deviation. Specifically, we find

$$\mu = 0.024 \pm 0.002 \tag{C.13}$$

$$\eta_A = (3.5 \pm 0.3) \times 10^{-4} \tag{C.14}$$

$$\eta_B = (4.7 \pm 0.3) \times 10^{-4} \tag{C.15}$$

$$\mathcal{F}_{\mathrm{BME}} = 0.91 \pm 0.01. \tag{C.16}$$

The retrieved pathway efficiencies are smaller by ∼9 dB compared to our insertion loss alone, which we estimate to be ∼25 dB from generation to detection. While we have fully characterized the insertion loss of the gate components themselves (12.9 dB in total: each EOM contributes ∼2.8 dB; the pulse shaper, ∼4.7 dB; and the remainder comes from polarization controllers and fiber patch cords), uncertainties remain in the state preparation and measurement components, such as the breakdown of loss inside the fiber-pigtailed photon source, as well as questions of how strongly the spectrally varying transmission of the etalon reduces its effective transmission from its peak value. Otherwise, the retrieved μ and fidelity match predictions. Even though $\mathcal{F}_{\mathrm{BME}}$ is smaller and has higher uncertainty than the classically inferred $\mathcal{F}_{\mathrm{inf}}$, the fact it still exceeds 90% with fairly sparse measurements is strong confirmation of excellent performance, particularly in light of the uninformative prior, which permits high fidelity only based on the strength of the observed data.

We also compute the mean and standard deviation for all elements of the retrieved transformation V, for both the magnitude and phase:

$$[r_{nn'}] = \begin{bmatrix} 0.452 \pm 0.005 & 0.124 \pm 0.009 & 0.06 \pm 0.01 & 0.02 \pm 0.02 \\ 0.06 \pm 0.03 & 0.465 \pm 0.008 & 0.475 \pm 0.006 & 0.411 \pm 0.006 \\ 0.04 \pm 0.01 & 0.463 \pm 0.005 & 0.470 \pm 0.005 & 0.03 \pm 0.01 \\ 0.028 \pm 0.009 & 0.455 \pm 0.005 & 0.02 \pm 0.01 & 0.413 \pm 0.005 \end{bmatrix} \tag{C.17}$$

$$[\phi_{nn'}] = \begin{bmatrix} -2.5976 \pm 0 & -2.8 \pm 0.2 & 1.3 \pm 0.1 & -2.01 \pm 0.09 \\ 0.30 \pm 0.09 & -2.6045 \pm 0 & -1.5754 \pm 0 & 1.5710 \pm 0 \\ 1.35 \pm 0.09 & -1.5754 \pm 0 & 2.6 \pm 0.1 & 0.7 \pm 0.2 \\ -2.0 \pm 0.1 & 1.5710 \pm 0 & 0.3 \pm 0.1 & 2.5 \pm 0.1 \end{bmatrix}. \tag{C.18}$$

As before, the phases with uncertainties ± 0 are those fixed prior to parameter retrieval. Comparing this result to the design [Eq. (A.5)], the most significant mismatch occurs for the element in row 1, column 2 (the coupling from mode C_1 to C_0). At 0.124, this value is significantly larger than designed, and contributes to the higher error for the cases $|C_1 T_0\rangle \rightarrow |C_0 T_0\rangle$ and $|C_1 T_1\rangle \rightarrow |C_0 T_1\rangle$ in Fig. 4.7. While the source of this error is still uncertain, experimentally we did observe extraneous counts on detector A during these integration times, beyond the theoretical prediction. Bayesian retrieval succeeds in finding matrix elements to account for this observation, as intended.

D. SINGLE-QUBIT QFP TRANSFORMATION SYMMETRIES

Consider a QFP composed of $N+1$ EOMs and N pulse shapers in an alternating series, and configured to realize single-qubit transformation $W = gU(\theta, 0, 0)$ [see Eq. (1) in the main text for the definition], where $|g|^2 \leq 1$ represents the gate success. Assume the first and last EOMs are driven by $A(t)$ and $B(t)$ (each $\frac{2\pi}{\Delta\omega}$-periodic waveforms), and the first and last pulse shapers are programmed with spectral phases p_k and q_k on the k-th frequency mode. The corresponding transformation by frequency multiport V, with projection of W onto the single-qubit space ($m, n \in \{0, 1\}$) is then

$$W_{mn} = \sum_{k=-\infty}^{\infty} \sum_{l=-\infty}^{\infty} d_{m-k} e^{iq_k} T_{kl} e^{ip_l} c_{l-n} \tag{D.1}$$

where T_{kl} is the mode transformation from all elements in the QFP apart from the first and last EOM/shaper pair. In the case of $N = 1$ (EOM/shaper/EOM QFP), T is an identity matrix and the center pulse shaper is programmed with $p_k + q_k$. The factors c_{l-n} and d_{m-k} are the mode coupling coefficients between modes n and l and modes k and m, for the first and last EOM, respectively. They represent the Fourier series coefficients of the periodic modulation, and can be expressed as

$$\begin{aligned} c_{l-n} &= \frac{1}{T} \int_T dt\, e^{iA(t)} e^{i(l-n)\Delta\omega t} \\ d_{m-k} &= \frac{1}{T} \int_T dt\, e^{iB(t)} e^{i(m-k)\Delta\omega t}, \end{aligned} \tag{D.2}$$

where the integration is over any full period $T = \frac{2\pi}{\Delta\omega}$.

To actualize $U(\theta, \varphi, \lambda)$, our goal is to reconfigure the QFP such that the new mode transformation $\tilde{W}_{mn}$ equals $e^{i(m\varphi+n\lambda)} W_{mn}$, or $gU(\theta, \varphi, \lambda)$ by specification. Suppose that we delay the RF signals applied to the first and last EOM by τ_a and τ_b, re-

spectively, and introduce additional phase shifts δ_k and ϵ_k to the first and last pulse shaper, respectively. We obtain the modified mode transformation

$$\begin{aligned}\tilde{W}_{mn} = e^{i\Delta\omega(m\tau_b - n\tau_a)} \sum_{k=-\infty}^{\infty} \sum_{l=-\infty}^{\infty} e^{i(\epsilon_k - k\Delta\omega\tau_b)} \\ \times \left[d_{m-k} e^{iq_k} T_{kl} e^{ip_l} c_{l-n} \right] e^{i(\delta_l + l\Delta\omega\tau_a)}\end{aligned} \tag{D.3}$$

In order to fulfill $\tilde{W}_{mn} = e^{i(m\varphi + n\lambda)} W_{mn}$, we can set the delays such that $\Delta\omega\tau_b = \varphi$, $\Delta\omega\tau_a = -\lambda$, and make the double summation in Eq. (D.3) identical to W_{mn} by choosing $\epsilon_k = k\Delta\omega\tau_b$ and $\delta_l = -l\Delta\omega\tau_a$. Thus, we arrive at a simple method for reconfiguring the QFP for $U(\theta, \varphi, \lambda)$ given $U(\theta, 0, 0)$: delay the RF signals applied to the first and last EOM by $\tau_a = -\frac{\lambda}{\Delta\omega}$ and $\tau_b = \frac{\varphi}{\Delta\omega}$, respectively, and add linear phases $\delta_k = k\lambda$ and $\epsilon_k = k\varphi$ to the first and last pulse shaper, respectively. The remaining settings of the QFP are unchanged. This procedure readily extends to higher-dimensional unitaries. For example, if the QFP is originally programmed to implement U, we could follow the same method to reconfigure QFP and realize $D_1 U D_2$, as long as D_1 (D_2) is a diagonal unitary with a constant phase increment φ (λ) across the diagonal elements. Intuitively, this process works because a linear phase is equivalent to a delay (while for a two-dimensional system, *any* arbitrary phase shift between two modes can be seen as a delay); tuning the bookend EOMs redefines the input/output phase references, while the pulse shaper corrections ensure that, inside the QFP, the frequency-bin mixing operation proceeds unaffected.

VITA

VITA

Hsuan-Hao (Peach) Lu graduated from the Undergraduate program of Electrical Engineering and Computer Science from National Tsing Hua University, Taiwan in 2014, and a M.S. in Institute of Photonics Technologies from National Tsing Hua University, Taiwan in 2016. He is currently pursuing a Ph.D. in electrical engineering at Purdue University. His research interests include photonic quantum information processing and ultrafast optics. His work has resulted in thirteen journal publications and numerous conference presentations, including a post-deadline talk at CLEO 2018, an invited talk at CLEO 2019, and the 3rd place winner at IPC 2020 on Best Student Papers. For his contributions to research, Hsuan-Hao was selected as a recipient of Optics And Photonics Education Scholarship by SPIE in 2019, and the College of Engineering Outstanding Graduate Student Research Award in 2020. Hsuan-Hao is a student member of The Optical Society (OSA), former vice-president of the Purdue student chapter of OSA, and an active reviewer for OSA and the American Physical Society (APS).